UNIVERSITÀ DEGLI STUDI DI PADOVA

Dipartimento di Fisica e Astronomia "Galileo Galilei"

Master Degree in Physics

Final Dissertation

DTT NBI fast particle modelling with Monte Carlo ASCOT code

Thesis supervisor

Dr. Tommaso Bolzonella

Thesis co-supervisor

Dr. Pietro Vincenzi

Candidate

Chiara De Piccoli

Academic Year 2021/2022

To my granparents
Carlo, Elsa, Gigi e Rosa.
You will always have
a special place in my heart.

Acknowledgements

I want to dedicate this page to thank who helped me and supported me during my thesis and my master degree.

First of all, I would like to thank my supervisor Tommaso Bolzonella, who always supported me, providing me with valuable advice and introducing me to the Consorzio RFX. A special thank to Pietro Vincenzi, my co-supervisor, who guided me and encouraged me during this work, being always present, teaching me innumerable things and giving an invaluable support. I am really grateful that I had the opportunity to work together, I hope this is just the beginning. I also would like to thank all researchers who helped me and discussed with me about this work. The kindness and support I encountered at the Consorzio pleasantly surprised me and I am grateful for having had the opportunity to work here. My interest on plasma physics has found here an environment to evolve and grow. Of course I cannot forget to thank also all the friends that I met here at the Consorzio for all the lunches and laughs together. I had a lot of fun!

A huge thank to my family, my father Mauro, my mother Fabiola, my brother Andrea and my sister Claudia, who always support me and encourage me to value my skills. After the remote bachelor degree declaration due to Covid-19, the thought of finally being able to have you by my side on the day of the discussion touches me. A thank also to all my friends, particularly Mattia and Sofia, who always understand the difficult moments but, above all, the immense satisfactions of this path.

A final and special thank to Luca, who has always been by my side. You always encourage me and give me the strength to face the challenges I encountered. I am grateful to have you in my life.

Chiara

Contents

Abstract

The present thesis deals with the analysis and modelling of the behavior of Energetic Particles (EPs) injected by a neutral beam in a tokamak plasma. By Neutral Beam Injection (NBI), it is possible to achieve the high temperatures needed for fusion reactions in plasmas, but also to drive current and provide torque. In order to study EPs, the orbit-following ASCOT Monte Carlo code is used. A good confinement of EPs is essential both for plasma performances and to avoid potentially harmful EP losses from confined plasma to the machine first wall. For this reason, EP modelling is used to predict their interaction with the plasma and to eventually set limitations for NBI use depending on plasma parameters. In particular, fast ion losses can be caused by particle orbits that cross the plasma boundary (orbit losses) or from injected neutral particles not ionized in the plasma (shine-through losses).

After a brief introduction presenting the foreseen advantages of employing fusion energy and the relevant concepts of plasma physics for this thesis, the theory of fast ion confinement and orbits is reviewed. The case of the Divertor Tokamak Test, an experimental device in construction in Frascati (IT), is then analyzed, with a classification of possible EP orbits through a topological map in the phase space defined by EP constants of motion and adiabatic invariant of the system. EP orbit topologies are shown for different DTT plasmas and for different EP injection energies, giving already a grasp of expected EP confinement and losses in the approximation of collisionless orbits. ASCOT modelling is then used to verify the different situations analyzed and to understand the role of EP collisions. ASCOT numerical results give also estimations of EP loss channels different from orbit losses, as for instance shine-through losses, showing their dependence on the plasma density as foreseen by theory. The theoretical study of EP orbits and numerical modelling of NBI-plasma interaction contribute to the understanding of predicted EP confinement and losses for the forthcoming DTT device, in order to allow for the most effective application of NBI in future DTT operations.

List of acronyms and abbreviations

CoM	Constant of Motion
DN	Double Null
DTT	Divertor Tokamak Test
ECRH	Electron Cyclotron Resonance Heating
EPs	Energetic Particles
FP	Fokker-Planck
FW	First Wall
GC	Guiding Center
GO	Gyro-Orbit
HFS	High Field Side
ICRH	Ion Cyclotron Resonance Heating
I/O	Input/Output
JET	Joint European Torus
LCFS	Last Closed Flux Surface
LFS	Low Field Side
MA	Magnetic Axis
NBI	Neutral Beam Injection
N-NBI	Negative ion source based - Neutral Beam Injection
P-NBI	Positive ion source based - Neutral Beam Injection
RF	Radio Frequency
RFP	Reverse Field Pinch
SN	Single Null
SOL	Scrape Off Layer

Structure of this work

Chapter 1 The nuclear fusion energy represents a promising source of energy for the future. In section 1.1, a brief discussion about the possible role of the nuclear fusion energy in the world energy panorama is illustrated. After that, an overview about fusion reactions is given in section 1.2, describing in particular how to obtain fusion reactions whose energy can be used for electrical energy production. In section 1.3, the relevant concepts of plasma physics for this thesis are explained, before discussing one of the possible approach which can be used to confine charged particles into a vessel, i.e. magnetic confinement. Section 1.4 is dedicated to the explanation of this approach. In section 1.5 the most promising magnetic confinement is presented. This is the tokamak configuration, adopted also by the Divertor Tokamak Test (DTT) facility, the experimental device analyzed in this work.

Chapter 2 Neutral Beam Injection is one of the DTT heating system. After a brief introduction on the Divertor Tokamak Test facility and its goals, illustrated in section 2.1, the descriptions of the NBI system and beam-plasma interaction physics are presented in section 2.2, where also the possible source of particle losses are described. An overview about the particle motion inside the plasma is given in section 2.3, focusing on the Energetic Particles (EPs) characteristics, which are the main interest of this work. The EPs behavior inside the plasma is complex and EPs modelling is useful to develop and efficient use of the NBI system. For this thesis, numerical studies about EPs are performed by the orbit-following Monte Carlo ASCOT code, illustrated in details in section 2.4.

Chapter 3 The numerical studies performed by ASCOT code about beam-plasma interaction for DTT are presented in chapter 3. To investigate how plasma parameters and NBI energy affect the EPs behavior inside the plasma, several simulations are performed by modifying the plasma temperatures and densities and the NBI energy. In sections 3.1 and 3.2, results of the plasma temperature and density scans are discussed, focusing on changes of several quantities estimated by ASCOT, as the absorbed power and the NBI driven current. The same analysis is performed changing the NBI energy and results are illustrated in 3.3.

Chapter 4 First topological analyses of EP orbits in DTT with ASCOT code are discussed in chapter 4. The first part of the chapter is dedicated to the presentation of the topological map in the phase space defined by constants of motion and adiabatic invariant of the system. This map is used to classify particle orbits and estimate EP losses. The description of the adopted convention and the magnetic field equilibrium characterizing DTT is given in section 4.1. The construction of the EP topological map is explained in sections 4.2. The guideline to interpret the map is reported on section 4.3, where the EP orbit "zoology" expected in DTT is also illustrated. The second part of the chapter shows the EP topological map populated by particle orbits using ASCOT simulations already presented in chapter 3. The differences in orbit classification and EP losses observed considering different plasma parameters and NBI energy are discussed in details.

Chapter 5 This chapter reports results obtained through the EP modelling performed with ASCOT code for DTT NBI. Possible future work are also discussed.

Chapter 1

Fusion energy and magnetic plasma confinement

In this chapter, an overview of nuclear fusion reactions and plasma physics is presented, starting from the mechanism that allows to obtain fusion processes and ending with the description of future fusion power plants and challenges to be faced for their realization. The DEMO project will be the last step of development for the production of energy through nuclear fusion, but there are still many challenges, both engineering and physical, that are making this path still long [1]. The promising fuel for future fusion power plant is a mixture of deuterium and tritium, two hydrogen isotopes. This mixture will form an ionized gas, called plasma, which must be confined at high temperatures, on the order of 100 million degrees, and sufficient density to produce fusion reactions in toroidal reactors. High temperatures can be reached with additional heating sources, as the Radio-Frequency (RF) or Neutral Beam Injection (NBI) heating, which will be a crucial additional heating system in today's and future tokamak configurations.

1.1 The energetic problem

At the time being, humankind is facing environmental problems as never before, as evidenced by evident climatic changes. At the same time, the energy request increases due to the development of countries and population growth. The energy produced in the last century has been obtained mainly from fossil fuels, such as coal, oil and natural gas. However, the emissions of greenhouse gases, as carbon dioxide, deriving from the exploitation of these resources have led to the climate changes that we are all witnessing today. To reduce these emissions, different energy scenarios capable of respecting the environment and producing the necessary energy at moderate and intrinsically safe costs are studied and assessed to be adopted by the countries. As reported in IEA "World Energy Outlook" [2], today's countries pledges towards a transition to sustainable energy reduce the gap for the Net Zero by 2050 scenario less than 20%, as shown in figure 1.1. In the context of zero net emissions, the fusion represents a good opportunity to produce energy, being an environmental-friendly, inherently safe and long lasting source. Fusion and other renewable energy sources, such as solar and wind energy, are fundamental ingredients for a sustainable energy mix, capable of meeting the world's energy needs, progressively replacing the use of fossil fuels.

1.2 Fusion reactions

Fusion energy is a form of nuclear energy. Differently from fission, that consist of the splitting of heavy atoms, fusion reactions take place when two light nuclei, as of hydrogen (H) and its isotopes, have enough energy to overcome the mutual Coulomb repulsion and merge together. The energy released from fusion reactions derives from the difference in mass between the mass of the product nuclei of the reaction and the sum of those of the two reagents. Reactions advantageous for the production of

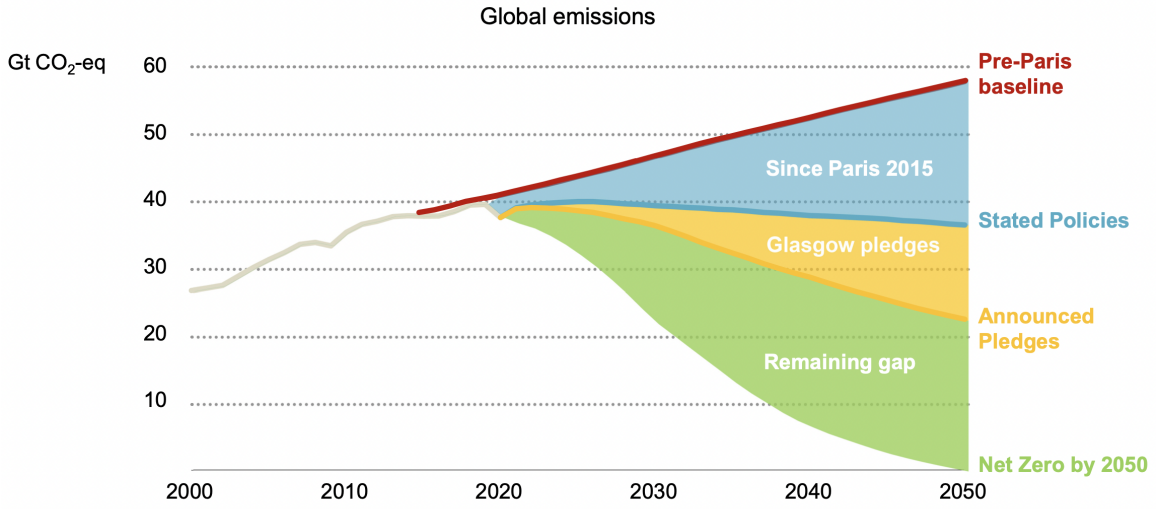

Figure 1.1: Carbon dioxide equivalent trend perspective until 2050. With today's pledges, the Net Zero scenario will not yet be reached in 2050. [2]

fusion energy are those between deuterium-deuterium (D-D) in (1.1),(1.2), deuterium-helium3 (D-^{3}He) in (1.3) and deuterium-tritium (D-T) in (1.4).

$$D + D \rightarrow {}^3He + n + 3.27 \text{ MeV} \tag{1.1}$$

$$D + D \rightarrow T + n + 4.03 \text{ MeV} \tag{1.2}$$

$$D + {}^3He \rightarrow {}^4He + H + 18.3 \text{ MeV} \tag{1.3}$$

$$D + T \rightarrow {}^4He + n + 17.6 \text{ MeV} \tag{1.4}$$

Deuterium and tritium are two hydrogen isotopes. The former is stable and can be easily extracted from the ocean. Deuterium reserve is almost unlimited, being able to sustain the production of energy for about 2 billion years at the present rate of total energy consumption [3]. Tritium instead is an unstable hydrogen isotope, with a short half-lifetime, of approximately 12 years. It must be produced directly inside the reactor by breeding with Lithium (equation(1.5)), which reserves are large enough to last thousands of years.

$$^6Li + n \rightarrow T + {}^4He + 4.8 \text{ MeV} \tag{1.5}$$

The D-T reaction is the central focus of the world fusion research. Indeed, reaction (1.4) is the easiest to initiate because of the large cross section of tritium, which means an higher probability to collide with incidental particles, as deuterium. This characteristic is quite evident in the figure 1.2 where the D-T cross section is visibly higher than those of others reactions at the same temperature. The D-T curve has a maximum at 100 keV of particle energy. However, already at 10 keV the number of fusion reactions that occurs between deuterium and tritium element is enough for future fusion reactors. The released energy E = 17.6 MeV of D-T reactions is equivalent to 388×10^6 MJ/kg, larger than that released by fission and chemical process (respectively about 84×10^6 MJ/kg and ~ 40 MJ/kg) [3]. Compared to fossil and fission fuels, D-T fuel appears advantageous in terms of energy equivalence as reported in table 1.1.

Fossil	Fission	Fusion
10^6 tonne oil	0.8 tonne uranium	0.14 tonne deuterium

Table 1.1: Energy equivalence among different resources. [3]

An efficient way to produce fusion reactions consists on creating a plasma of H isotopes in a reactor under condition which can guarantee the self-sustenance of the process, defined by the so-called Lawson

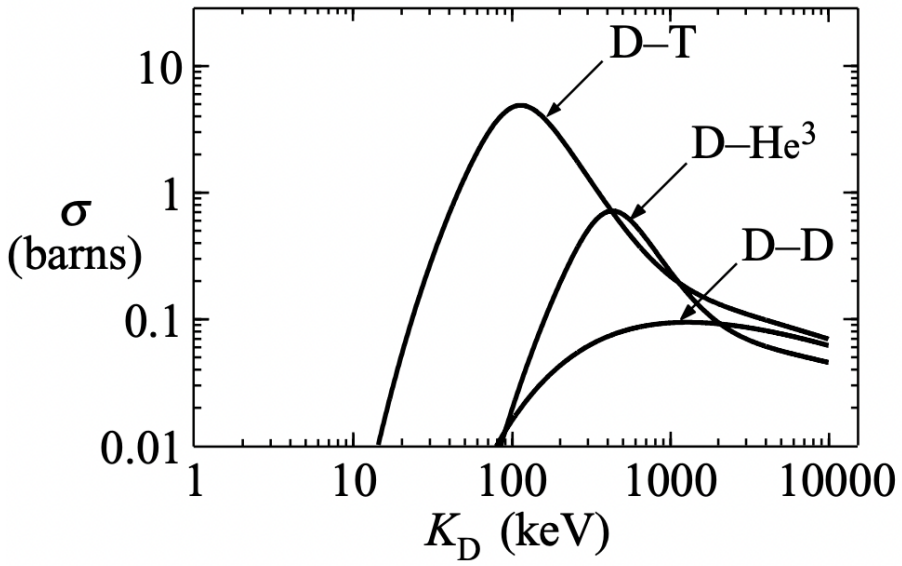

Figure 1.2: Experimental measured cross sections σ for different fusion reactions (D-T, D-^{3}He, D-D) as a function of the kinetic energy of a deuterium K_D. [3]

criterion. This condition is fulfilled when the product between temperature T, density n and energy confinement time τ_E of the plasma fulfill the relation in (1.6). The Lawson criterion can be satisfied e.g. with $n = 10^{20}\ m^{-3}$, T = 10 keV, $\tau_E = 3$ s.

$$nT\tau_E > 3 \times 10^{21}\ \frac{keVs}{m^2} \tag{1.6}$$

At temperatures of the order of 10 keV, the mixture of deuterium and tritium atoms is on the state of plasma. It is the state of matter in which stars, the natural example of the great potential of fusion energy, are found too.

1.3 Plasma physics

Inside a fusion reactors, temperatures must be of the order of 10 keV to obtain enough fusion reactions between deuterium and tritium atoms. At this temperature, the mixture gas becomes ionized, i.e. a plasma. A fusion plasma is a fully ionized gas where charged particles interact through long-range electromagnetic interactions. Fusion plasmas are good conductors of electricity, mostly at high temperatures and low densities when, due to rare Coulomb collisions, resistance is low. The main characteristics of plasma concern its quasi-neutrality property and the presence of collective effects, typical of fluids. Even if plasma is a collection of charged particles, it can be considered as a quasi-neutral gas. The number density of ions and electrons (positive and negative charges) is almost the same $n_i \sim n_e$ (densities are not equivalent because of the presence of Z > 1 impurities) and any charged imbalance is restored by the electric field that arises due to long-range interactions between particles. Charge imbalances only exist within the so called Debye length λ_D, defined as

$$\lambda_D = \left(\frac{\epsilon_0 T_e}{e^2 n_e}\right)^{1/2} \tag{1.7}$$

where T_e and n_e are temperature and number density of electrons and ϵ_0 the vacuum permittivity. The role of collective effects are instead measured by the plasma parameter Λ_D. This quantity gives a measure about the number of particles which interact simultaneously and is related to the plasma density n_e as defined in the following relation

$$\Lambda_D = \frac{4\pi}{3} n_e \lambda_D^3 = \frac{4\pi}{3}\left(\frac{\epsilon_0 T_e}{e^2}\right)^{3/2} \frac{1}{\sqrt{n_e}} \tag{1.8}$$

When Λ_D is much larger than 1, collective interactions dominate the plasma behavior, meaning that more particles interact collectively [4]. From (1.8) is easy to see that $\Lambda_D > 1$ is satisfied at low densities. Since this thesis analyzes the plasma of the Divertor Tokamak Test (DTT) device (see section 2.1), quantities defined in (1.7) and (1.8) for this facility are reported in table 1.2. The reference plasma parameters used are $n_e = 1.8 \times 10^{20}$ m$^-3$ and $T_e = 6.1$ keV, reported in section 2.1.1.

Debye length λ_D	Plasma parameter Λ_D
4.33×10^{-7} m	6.12×10^{7}

Table 1.2: Debye length and plasma parameter for DTT.

1.4 Magnetic confinement

Not only high temperatures and low densities must be achieved to obtain fusion reactors starting from a D-T fuel. Charged particles must be also confined since the hot gas that they form cannot be contained in a conventional vessel [5]. Two different approaches can be used to this: inertial confinement and magnetic confinement. With the former approach, fusion reactions happen by compressing and heating deuterium-tritium targets, by means of high power laser beams. This process force nuclei within short distances that allow fusion reactions. The magnetic confinement instead is based on the use of external magnetic fields to confine plasmas. This is the method on which the European Fusion Program [1] is based and set the framework of this thesis. Charged particles in plasmas feel the Lorentz force due to the presence of magnetic fields which imposes them to move circularly around the magnetic field lines. This motion, known as gyro-motion, will be presented in more details in section 2.3.1, together with the "average" particle motion known as guiding center motion. Charged particles can move freely along magnetic field lines remaining confined inside the plasma since the radius of the circular motion, called Larmor radius r_L, is small compared to typical macroscopic dimension of plasmas.

The first magnetic confinement setups were based on linear magnetic field configurations, as the case of the magnetic mirror. Particles are confined inside a plasma column by the presence of an intense magnetic field at the ends of the column. To preserve energy, some particles experience the mirror effect, i.e. approaching the ends, they turn back and remain confined inside the column. A significant amount of particle losses at the ends of the plasma makes this kind of particle confinement not feasible. A more effective approach consists of closing magnetic field lines on themselves, generating a toroidal configuration. In this case end losses are avoided but some losses in radial direction are still present and must be reduced. These losses are determined by drifts of the guiding center motion of particles and to avoid them the magnetic field lines must be helical twisted. This magnetic configuration can be obtained using coil systems which provide toroidal magnetic field and plasma current to form the main poloidal magnetic field component or using complex shaping coils that generate directly an helical field. The former case is exploited by tokamak and Reverse Field Pinch (RFP) devices, while the latter by stellarator concepts.

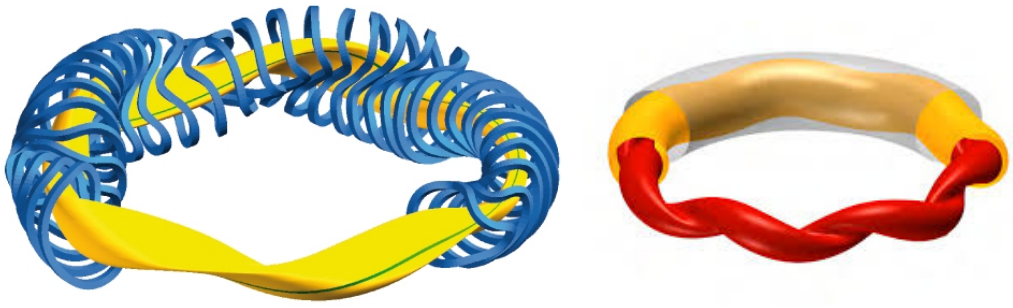

Figure 1.3: **Left.** Schematic design of Wendelstein 7-X experiment in Germany [6]. **Right.** Reversed Field Pinch configuration used in RFX-mod2 device [7] in Padua, Italy.

The Wendelstein7-X (W7-X) [6] in Germany and the Large Helical Device (LHD) [8] in Japan are two experiments built to test the stellarators concept [6]. These devices exploits a complex series of magnetic coils, that are able to provide a helical configuration to the magnetic field lines of the device. The largest Reversed Field Pinch device is RFX-mod (Reversed-Field eXperiment), located in Padua (Italy) [7]. The RFP configuration is characterized by different directions of the toroidal magnetic field at the core and at the edge of the plasma. It uses magnetic field with lower intensity than those used in tokamaks configuration, which instead represent the most promising and advanced fusion concept. Magnetic confinement in tokamaks is provided by different magnetic coil systems, necessary to provide the toroidal components of the magnetic field and the plasma current, which produces the main poloidal component of the magnetic field and maintains shape and position of the plasma volume. In the following section a more detailed description of tokamaks and modern devices using this configuration is provided.

1.5 Tokamak configuration

The most promising configuration to confine plasma is that of tokamak. Invented in the Soviet Union in late 1950s, it consists on a axisymmetric toroidal vacuum chamber in which plasma can be formed and confined by different systems of magnetic coils. Among them, the toroidal field coils and the central solenoid are the main systems which provide magnetic confinement. The first system is composed by a set of coils radially distributed around the torus which produces the toroidal component of the magnetic field. The central solenoid instead corresponds to the primary circuit for the generation of plasma current. This current determines the presence of a poloidal component of the magnetic field, that is necessary to confine plasma in a stable equilibrium. Combination of toroidal and poloidal components gives rise to an equilibrium configuration where magnetic field lines follow helical trajectories. Other sets of coils are used to maintain shape and position of the plasma volume, as the poloidal magnetic field coils. In figure 1.4 coil systems necessary for the proper tokamak operation are designed.

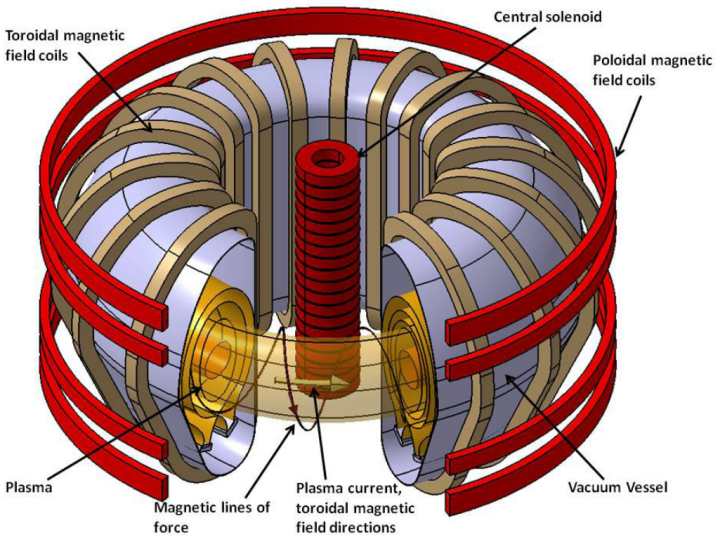

Figure 1.4: Scheme of tokamak magnetic coil systems. [9]

Tokamak configuration is the most successful concept for a fusion reactor, thanks to its efficient plasma confinement. The achieved value of triple product $nT\tau_E$ of the Lawson criterion in (1.6) exceeds those of any other concepts [3]. The intensity of the toroidal field is limited by technological factors, as heat dissipation by Joule effect and magnetic stress on coils and structure itself. However, with the use of superconductive coils, heat dissipation problem could be partly solved. At present, the highest achievable magnetic field near the coils is about 12 T, with a value of about 6 T in the plasma core.

Fusion reactor as tokamaks can operate as a steady state or long pulses device. This requires use

of externally driven currents, implying costs without any guarantee that the power balance will be favorable, due to the not so high efficiency of current-drive systems. A way to satisfy the steady state or long pulses condition without economical problems is to rely on bootstrap-current, that is a natural current inside the plasma generated by transport processes. High bootstrap current requires an high β parameter, a quantity that evaluates the effectiveness of plasma magnetic confinement defined as the ratio of plasma and magnetic pressure, $\beta = \frac{p}{B^2/2\mu_0}$. However it is difficult to achieve high β parameters due to plasma instabilities. Therefore external systems to provide current are necessary. These systems provide also heat, heating the plasma to the temperatures necessary for fusion reactions. Indeed, even if an initial warm-up is given by ohmic heating that already occurs inside plasma, the ohmic heating is sufficient to reach just a few keV of thermal energy since plasma resistivity decrease with its temperature. The necessary energy for fusion reactions can be reached using different external systems to heating and current drive, as the Radio-Frequency (RF) heating and the Neutral Beam Injection (NBI). The first one consists on launching electromagnetic waves into magnetized plasma and exploiting resonances with plasma natural frequencies. It is possible to distinguish two different RF heating modes, called Ion and Electron Cyclotron Resonance Heating (ICRH and ECRH). The first one requires frequencies of the order of ω_{ci}, the ion cyclotron frequency, to transfer energy to ions inside plasma. ω_{ci} covers a range of 30-120 MHz. The second method heats the plasma electrons at higher frequencies, in an interval between 100-200 GHz, of the order of the electron cyclotron frequency ω_{ce}.

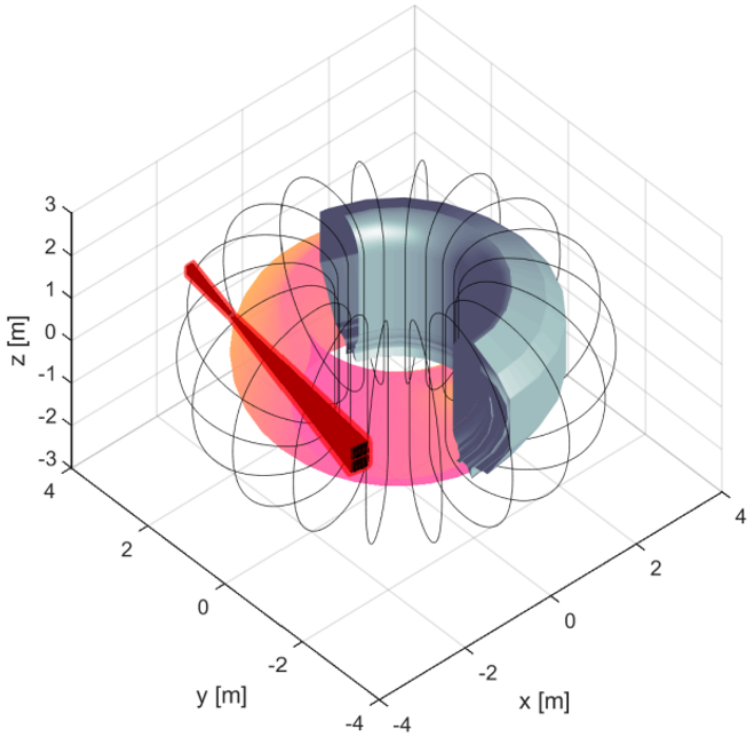

Figure 1.5: Sketch of the DTT neutral beam (red cones) entering the plasma. [10]

The NBI instead is based on injection of neutral particles at energy E_{NBI} greater than that of thermal particles of plasma. These neutrals can be generated by an initial source of positive (P-NBI) or negative (N-NBI) ions. Using positive ions, the efficiency of the neutralization, that occurs before the injection of beam particles into the plasma, decreases with increasing beam energy. Negative ions instead are more difficult to produce but have a high neutralization efficiency also at high energy [3]. The N-NBI option is the most suited to the need of the modern experiments since the neutralization efficiency of the P-NBI starts to decrease at about 100 keV of injected energy [3]. The injected neutrals are ionized inside the plasma, creating a population of confined Energetic Particles (EPs) which heat the plasma during the thermalization process, by means of Coulomb collisions with plasma particles.

When fusion reactions occur, energetic particles are already present inside the plasma. These are the alpha particles and their contribution to fusion power becomes dominant at temperatures larger than 5-7 keV, which can be reached using external heating systems. The behavior of EPs generated by the NBI in the DTT scenario is the central topic of this work. The analysis of their behavior is crucial in order to investigate their confinement and losses. The NBI is one of the auxiliary external heating system which will be used in DTT to reach the reactor power. The Neutral Beam system and the basic physics of NBI-plasma interaction will be described in more details in chapter 2. In figure 1.5 the sketch of the DTT neutral beam entering the plasma is shown.

DTT, together with JET and ITER, are fusion experiments that adopted a tokamak configuration. JET [11] (Joint European Torus) is one of the most successful fusion experiment in the world, located in Oxford (UK). ITER [12] is still under construction in Cadarache (France) and will be the largest tokamaks ever built. ITER primary goals are to prove the possibility to obtain the power-gain requested for a fusion reactor ($Q = \frac{P_{output}}{P_{input}} > 1$) and to maintain fusion reactions for long periods. DTT (Divertor Tokamak Test) is the test-bed facility for ITER and DEMO (DEMOnstation fusion power plant), which is the ambitious project for the construction of the first nuclear fusion power plant that will prove the industrial feasibility of electricity production from fusion reactions. DTT was proposed on the European Roadmap for Fusion Energy [1] to study possible solutions able to mitigate the power exhaust problem in ITER and DEMO, one of the major challenges in the design and development of future fusion power plants. In the following chapter, an overview of DTT properties and scientific goals is illustrated, focusing later on the NBI system with which DTT will be equipped and the behavior of EPs born from neutral beam injection.

Chapter 2

Energetic particles from Neutral Beam Injection in DTT

This chapter is dedicated to the introduction of the DTT (Divertor Tokamak Test) facility and its goals, with a detailed description of the design and the physical parameters requested for the DTT operation in relevant condition for ITER and DEMO. Then an overview of the neutral beam system and the beam-plasma interaction processes is given, to finally focus on the behavior of NBI Energetic Particles (EPs). Studying EPs is of primary importance since they behave similarly to the alpha particles obtained in fusion reactions. DTT will have a significant EP population, mainly thanks to high-energy NBI. The modelling of EP dynamics will be performed in this thesis by ASCOT, an orbit-following Monte Carlo code able to simulate ionization and slowing-down processes of EPs inside the plasma. The chapter is structured as follow. First of all, a description of the DTT facility and plasma target scenario will be given, together with a general characterization of NBI system and beam-plasma processes. Then a physical description of particle motion and orbits will be discussed, focusing on EPs characteristics. Finally, the ASCOT modelling code, used to simulated EPs behavior after the injection in the plasma, is illustrated.

2.1 DTT: Divertor Tokamak Test facility

The Divertor Tokamak Test (DTT) facility was proposed in the European Roadmap [1] for the realization of fusion energy. DTT primary goal is to evaluate alternative divertor configurations for the power exhaust problem, one of the major challenges for future fusion power plants. Some plasma particles, due to collisions with other particles or drift effects, can be lost outside the plasma edge, defined by the Last Closed Flux Surface (LCFS), also called separatrix.

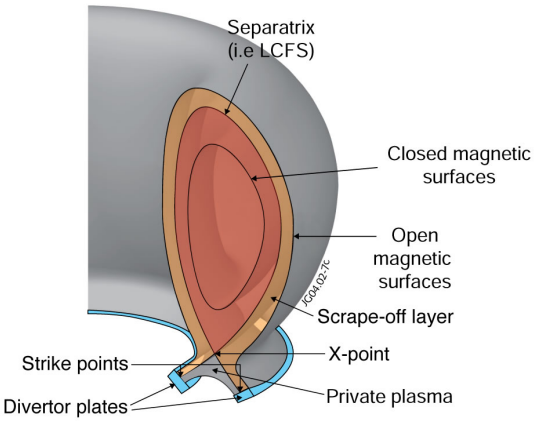

Figure 2.1: Sketch of magnetic confinement with a divertor plasma-wall interface. [13]

These escaping particles find open magnetic field lines in the so-called Scrape-Off Layer (SOL), a narrow layer outside the separatrix. Open magnetic field lines are deviated into specific target plates. In the SOL-region, neutral gas is injected to reduce the heat flux to target plates. The region of target plates is called divertor, i.e. the region of plasma-wall interface[1] that collects the energy flowing out from plasma. In figure 2.1, a sketch representing plasma edge and divertor region is shown. The geometry of the divertor in the figure is a conventional one, known as Single Null (SN). Even if the conventional divertor configuration will be used in ITER, the larger heat load expected in DEMO requires further investigations. DTT was proposed in this sense, to assess the performance of a conventional ITER divertor but also to investigate alternative divertor geometries and materials that could withstand the thermal load of DEMO. Flexibility is therefore one of the primary characteristics of DTT for the study of different divertor configurations, i.e. the plasma shape in the divertor region, as illustrated in figure 2.2. The reference divertor configuration is the Single Null (SN). Following the order of the figure, the alternatives are the Double Null (DN), snowflake, X-divertor, negative triangularity and double super-X configurations. All of them are characterized by different plasma shapes and currents, resulting in different plasma characteristics.

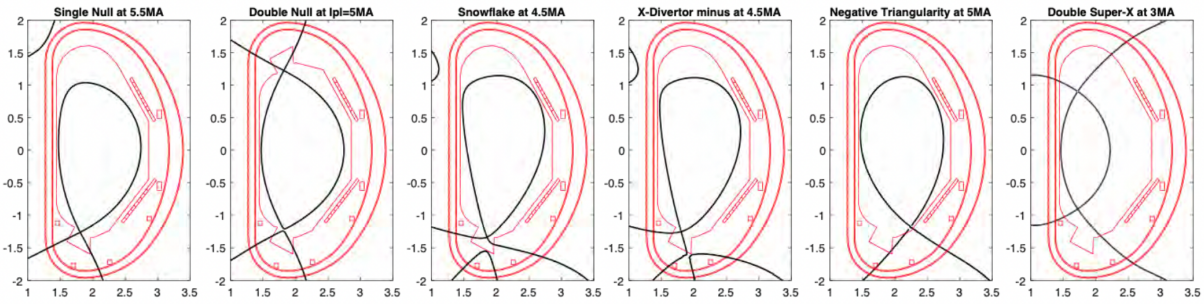

Figure 2.2: DTT possible divertor configurations, as planned in [5].

DTT is a mainly-italian collaboration, managed by ENEA, ENI and CREATE with the participation of important Italian research centers and universities, included Consorzio RFX [14]. The conceptual design of DTT project is terminated and DTT should start its operation in 2026. The DTT schedule, shown in figure 2.3, includes five phases where a gradual increase of power (from 8 MW to 45 MW) is foreseen.

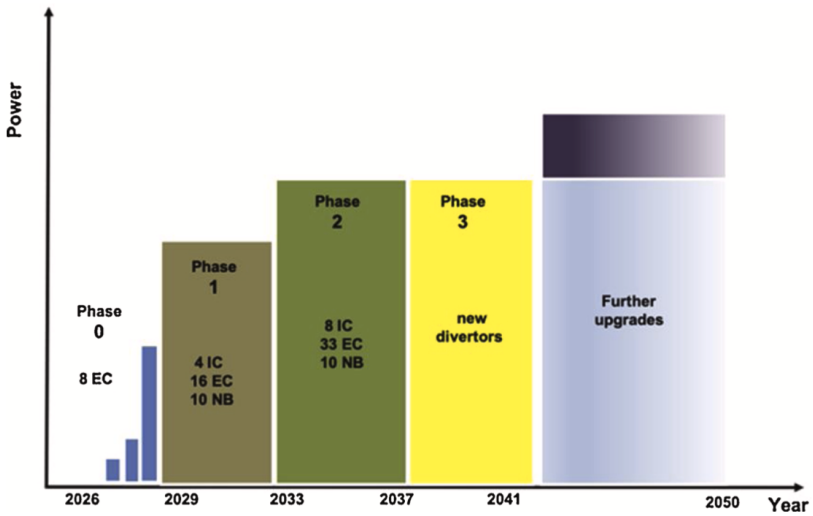

Figure 2.3: DTT planning [15]

[1] Another plasma-wall interface is the limiter. As the divertor, the limiter collects particles that diffuse across the LCFS but, being it is in direct contact with the plasma and, as a drawback, increases the number of impurities in the plasma.

2.1.1 Design and physic requirements

In order to be relevant for ITER and DEMO, the design of DTT has been guided to specific plasma parameters. The target plasma scenario for DTT is the single null and Full Power (FP) configuration, i.e. the maximum available auxiliary power. This scenario is characterized by parameters reported on table 2.1, as the volume averaged electron temperature and density, respectively of $< T_e >= 6.1$ keV and $< n_e >= 1.8 \times 10^{20}\ m^{-3}$, or the effective charge number Z_{eff}, defined in [9] as $Z_{eff} = \sum_i \frac{n_i Z_i^2}{n_e}$. Some of these parameters are in the range of those of DEMO, as the electron temperature $< T_e >$ and the beta parameter β. The DTT kinetic profiles, predicted by 1.5D transport simulations [16], are shown in figure 2.4. Actually, the total ion density, asides from the deuterium contribution n_D, includes impurity densities. After the injection, indeed, other ion species, henceforth called impurities, can be found inside the plasma, as tungsten (W) and argon (Ar). Argon is injected specifically to cool the plasma edge and safe the divertor heating. Tungsten instead derives from the interaction between plasma particles and the divertor, covered by tungsten. The target plasma scenario presented here will be used as reference in the numerical studies presented in chapter 3 and 4. Table 2.2 reports DTT design parameters [15]. The dimension of DTT are smaller than those of ITER ($R_0 = 6.2$ m, a = 2 m) and DEMO ($R_0 = 9.1$ m, a = 2.93 m), but with an equal aspect ratio R_0/a = 3.1.

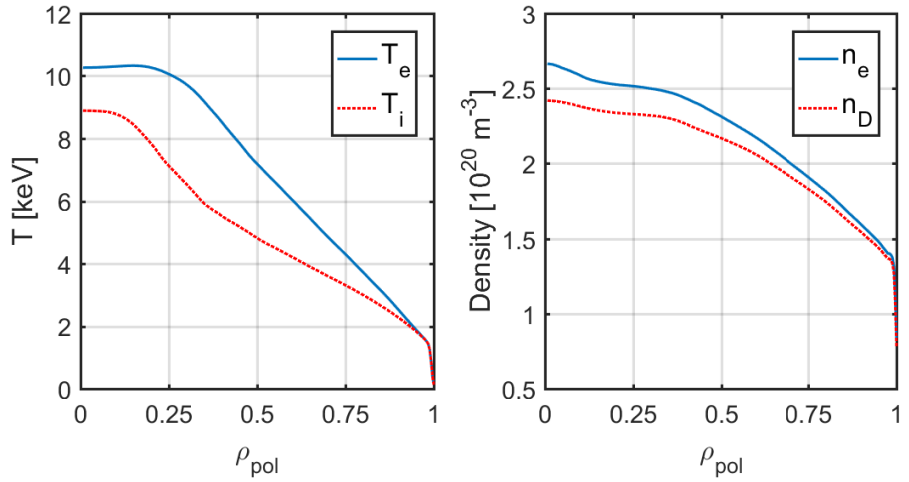

Figure 2.4: Kinetic profiles for the target plasma scenario [10].

Electron density $< n_e > 10^{20}$ [m^{-3}]	1.8
Electron temperature $< T_e >$ [keV]	6.1
Energy confinement time τ_e [s]	0.43
Plasma parameter β [%]	2.2
Normalized ion Larmor radius ρ^* [10^{-3}]	2.9
Ion Larmor radius r_L [10^{-6} m]	2.0
Effective charge number Z_{eff}	~ 1.7

Table 2.1: Reference DTT physical parameters estimated with a 0D approach [15].

Major radius R_0 [m]	2.19
Minor radius a [m]	0.70
Aspect ratio R_0/a	3.1
Plasma current I_p [MA]	≤ 5.5
Toroidal magnetic field B_T [T]	≤ 6
Heating power P_{tot} [MW]	≤ 45
P_{sep}/R_0 [MW/m]	~ 15
Pulse length [s]	~ 100
SOL thickness λ_q [mm]	0.7

Table 2.2: DTT design main parameters [15].

Additional heating systems are employed to reach the total power P_{tot} required for the optimal operation of DTT. Those are ECHR, with an installed power up to 32 MW, ICHR, with an installed power up to 8 MW and the N-NBI. The injector will provide 10 MW with an injection energy of 510 keV.

2.2 Neutral Beam Injection

Without the use of auxiliary heating and current drive systems, fusion reactions in plasma cannot be obtained and sustained with a favorable power balance. The Neutral Beam Injection is a way to heat the plasma but also to drive current, provide torque and fuel to the plasma. Its role in DTT is extremely important because it will provide a significant fraction of axuliary power (10 MW of 45 MW required). As already explained in the chapter 1, the NBI consists on the injection of neutral particles inside the plasma. Colliding with the plasma particles, neutrals are ionized becoming fast ions and after that, by means of Coulomb collisions with the background plasma, fast ions slow down transferring energy to plasma electrons and ions. In the following, a brief description concerning how a neutral beam is created and beam-plasma interaction processes are discussed, providing also the characteristics of the NBI system in DTT.

2.2.1 Neutral Beam Injection system

The NBI system is composed by four parts, represented in figure 2.5: the ion source, the accelerator, the neutralizer and the residual ion dump. An energetic beam is created starting from an ion source, that can be positive or negative. Positive ion beams have low efficiency in the neutralization process and therefore they are not suitable for energy injection above $\sim$ 100 keV. Negative beams instead are more difficult to create but electrons can be easily stripped away from the negative ion during the neutralization phase, also at high energy. For this reason, the negative ion source is preferred for high-energy NBI. The second step consists on the acceleration phase, in which ions, positive or negative, are accelerated to high energies by means of an high voltage. This phase is where most of the input electrical power is consumed [3]. The third step foresees the neutralization of high energy ions. Without the neutralization, ions would be lost as soon as they feel the magnetic fields that confine the plasma because of the Lorentz force. Ions that are not neutralized are deviated into a beam dump exploiting a magnetic or electrostatic field. This allows to avoid unwanted fast ion losses on the DTT duct. The residual ion dump therefore acts as a filter after the neutralizer. The remaining neutral particles are then injected inside the plasma.

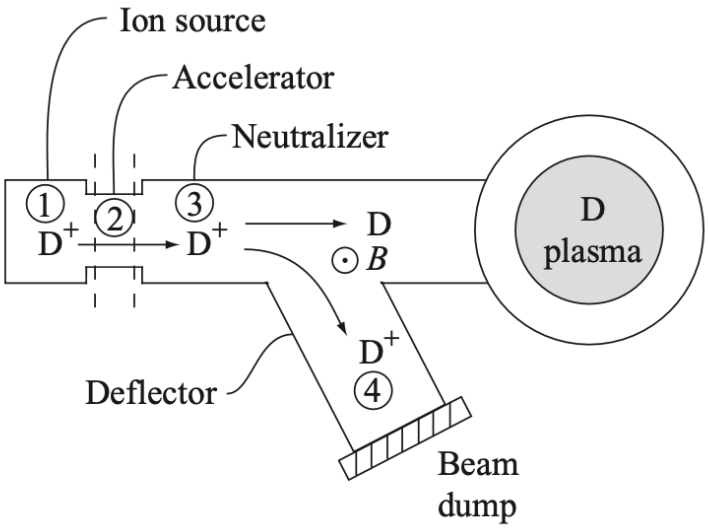

Figure 2.5: Schematic design of the neutral beam injection system [3].

The NBI system design has some implications in the beam-plasma interactions. The beam dimensions, as well as the beam divergence, are fixed by the acceleration grid design. Also the beam trajectory is fixed. It is possible to distinguish two extreme injection directions, tangential and perpendicular to the torus (figure 2.6). The first one provides torque and drives plasma current. Tangential injection can happen both in co- and counter-current directions. Moreover, it is also possible to inject particles at the magnetic axis (on-axis) or at different vertical and horizontal positions than those at which the

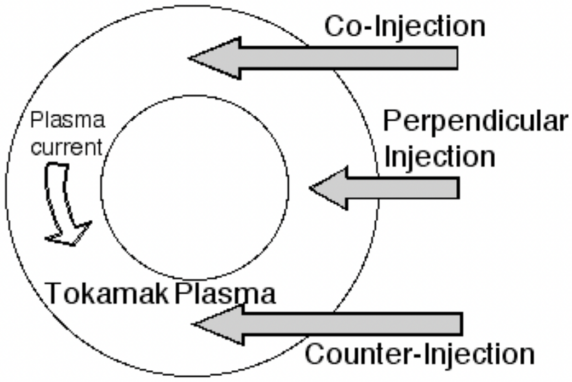

Figure 2.6: Possible injection directions for the NBI system [9].

magnetic axis is located (off-axis). The perpendicular injection instead is used to strongly heat the plasma core. This injection direction is affected by consistent particle losses, as first orbit losses, i.e. particles lost in time scale shorter than collision time scale, or shine-though losses, i.e. particles that hit the inner wall of the device after passing through the plasma without being ionized.

2.2.2 NBI system in DTT

The use of NBI system dates back to the 70s [17]. In today's experiments, the NBI is one of the necessary solutions to create fusion reaction in future power plants. ITER will be the first experiment with the highest beam heating system ever design, of about 1 MeV of injected energy. In the middle, the DTT NBI system is design to heat the plasma with an energy of 510 keV and an installed power of 10 MW [18], similarly to to neutral beam that will be used in JT60-SA, the toroidal device in Japan [19]. The conceptual design and research on the development of the DTT NBI system will last until 2025, with the goal of the installation on DTT in 2033. The NBI system in DTT will provide deuterium or hydrogen neutrals. It is located on the equatorial plane of the tokamak, to be suitable also in diagnostic terms. It is composed by a single-beam starting from a negative ion source. The injection happens in the tangential direction, in the same direction of the plasma current (co-current injection). The energy of the beam can be modulated, with a linear decrease of power, with energy in the range 250-510 keV [10]. In figure 2.7, the top view of the NBI system in DTT and the scheme of the injector are shown.

2.2.3 Beam-plasma interactions

What happens after the injection of the neutral beam in the plasma can be summarized in two processes: ionization and thermalization (or slowing-down). In the first process, fast neutrals are ionized by means of three different reactions and become Energetic Particles (EPs), also referred to as fast ions. In particular, ionization happens by charge exchange (2.1) or ionization by plasma ions (2.2) and electrons (2.3).

$$H^0 + H^+ \rightarrow H^+ + H^0 \tag{2.1}$$

$$H^0 + H^+ \rightarrow H^+ + H^+ + e^- \tag{2.2}$$

$$H^0 + e^- \rightarrow H^+ + 2e^- \tag{2.3}$$

The same processes happen for H, D and T atoms. Also the interaction with impurities in the plasma could determine ionization process. The cross sections of ionization reactions are reported in figure 2.8. They depend on the beam energy: at high energy, the ionization by ions and electrons are the more efficient, while at lower beam energy the charge-exchange interaction dominates. After the ionization, fast ions are thermalized by Coulomb collisions with the background plasma. During this process, EPs release energy to plasma ions and electrons in different fractions. In this way, the energy of the beam is transferred to the plasma. The critical energy E_c represents the beam energy at which the fraction

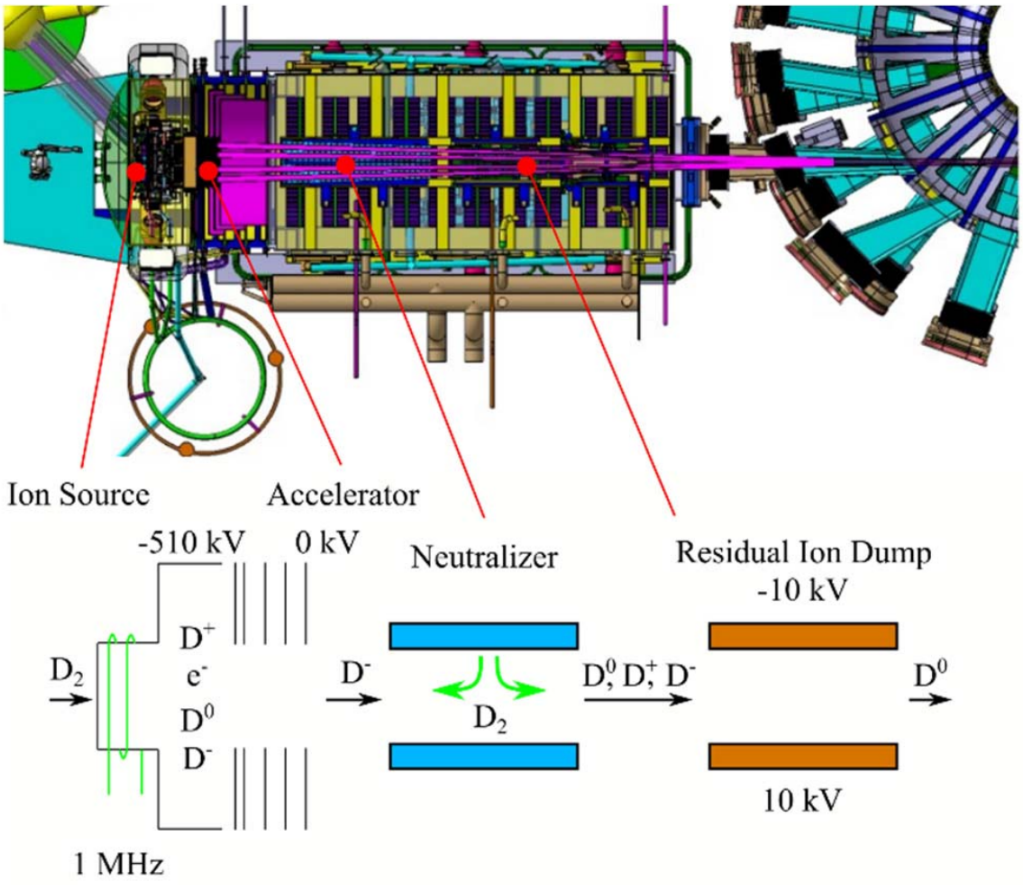

Figure 2.7: Top view of the DTT NBI system and scheme of the injector [18].

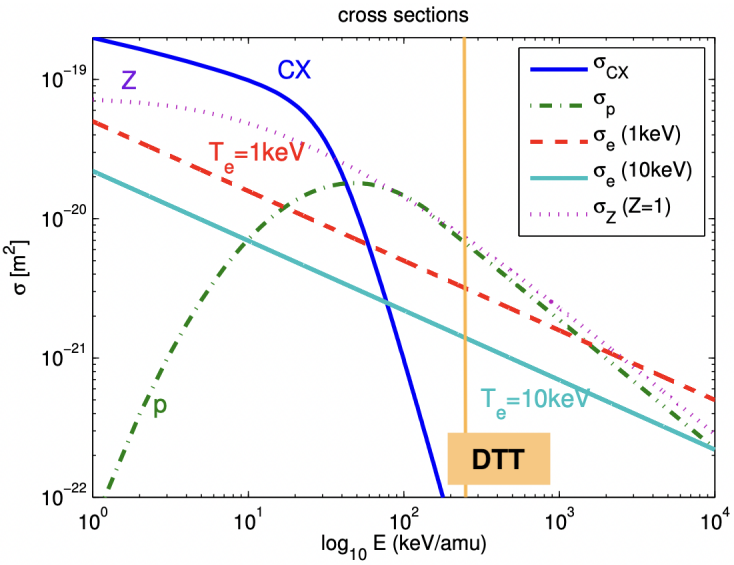

Figure 2.8: Cross sections for neutrals ionization by charge-exchange σ_{cx}, ion collisions σ_p, electron collisions σ_e and ionization by impurities with atomic number Z σ_Z [20]. The orange line identifies the DTT NBI energy (510 keV).

of energy transferred by collision to ions is equal to the one transferred to electrons. Assuming that velocities $v_i \ll v_b \ll v_e$, where i, b, e subscripts stay for ions, beam and electrons, the critical energy is defined as

$$E_c = \left(\frac{9\pi m_p}{16 m_e}\right)^{1/3} T_e \left(\frac{A^{3/2}}{n_e}\sum_i \frac{n_i Z_i^2}{A_i}\right)^{2/3} = 14.8 T_e \left(\frac{A^{3/2}}{n_e}\sum_i \frac{n_i Z_i^2}{A_i}\right)^{2/3} \tag{2.4}$$

where m_p, m_e are the proton and electron mass, T_e represents the electron temperature, n_e, n_i the electrons and ions densities, A the fast ions mass number and n_i, Z_i, A_i the charge and mass numbers of plasma particles [21]. Considering the injection of deuterium neutrals[2], the average critical energy for DTT is defined as $< E_c > = 114$ keV, using Z_{eff} and the average volume values for T_e and n_e reported in table 2.1. When the beam energy E_{NBI} is higher than E_c, the energy is preferentially transferred to electrons; while the energy transferred to ions dominates at $E_{\mathrm{NBI}} < E_c$. In particular, from equation (2.4), the higher is the electron temperature, the higher is the critical energy, therefore the lower is the fraction of energy transferred to plasma electrons. Integrating over the slowing-down process, the fraction of power delivered to ions and electrons can be represented in figure 2.9 in terms of the ratio between the injection energy and the critical one. Curves describe also the dependence on n_0/n_e, with n_0 the neutral atom density. Considering $n_0/n_e \sim 10^{-6}$, it worth noting that the delivered power to ions and electrons is equal at $E_{\mathrm{NBI}} \sim 2.5 E_c$.

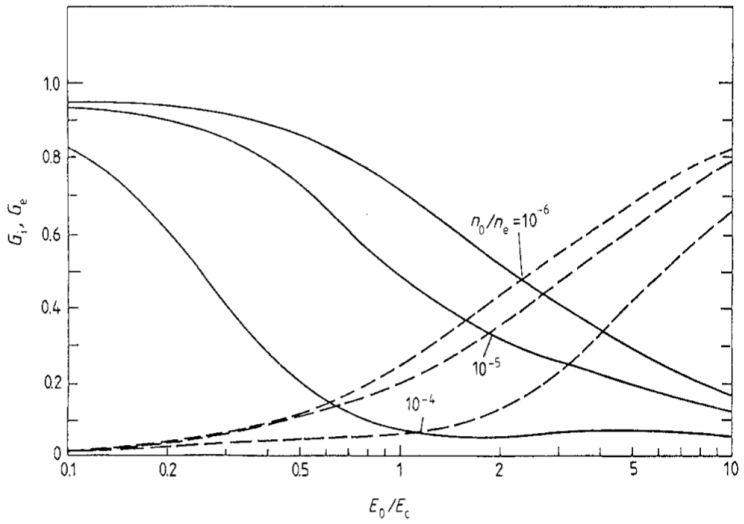

Figure 2.9: Fraction of power delivered to ions G_i (solid curve) and electrons G_e (dashed curve) versus E_{NBI}/E_c for different n_0/n_e ratios, with n_0 the neutral atom density [21].

The fraction of power deposited from fast ions to plasma particles turns out to be useful also in determining the efficiency of the Current Drive (CD) effect obtained injecting the neutrals beam in tangential direction. A tangential NBI produces a fast ions current I_{CD}. As reported in [22], the efficiency of the fast ion current drive, in the absence of trapped electrons, can be computed as the ratio between the fast ion current density on a specific flux surface j_f and the deposited power per unit volume P_d

$$\eta_{\mathrm{CD}} = \frac{j_f}{P_d} = \frac{2\tau_s e Z_f}{m_f v_0 (1+u_c^2)} \int_0^1 f_1(u) u^3 du \tag{2.5}$$

with fast ions charge $Z_f e$, the slowing-down time τ_s , i.e the characteristic time required to fast ions to become thermalized particles, the fast ion mass and charge number m_f, Z_f, the injection velocity v_0 and its normalized value $u = \frac{v}{v_0}$. The distribution function $f_1(u)$ is given by

$$f_1(u) = u^{2\beta}\left[\frac{1+u_c^3}{u^3+u_c^3}\right]^{1+2\beta/3}$$

[2]The critical energy for deuterium is characterized by a factor 18.6 instead of 14.8

where

$$\beta = \frac{m_i Z_{eff}}{2 m_f \bar{Z}} \qquad u_c^3 = \frac{3\sqrt{\pi}}{4} \frac{m_e \bar{Z} v_{Te}^3}{m_i v_0^3} \qquad \bar{Z} = \sum_i \frac{m_f n_i Z_i^2}{m_i n_e}$$

with subscript i related to ions and v_{Te} the thermal particle velocity. Solving (2.5) indicates that to achieve high value of CD efficiency, T_e and n_e must be such that the slowing down time τ_s is maximized and the injection energy E_{NBI} must be close to the critical value E_c. The slowing down time is computed as

$$\tau_s = \frac{t_s}{3} ln \left(1 + \left(\frac{E_0}{E_c} \right)^{3/2} \right) \tag{2.6}$$

where t_s is the Spitzer slowing down time defined as

$$t_s = 6.28 \cdot 10^8 \left(\frac{A T_e^{3/2}}{Z^2 n_e ln\Lambda} \right) \tag{2.7}$$

with the Coulomb logarithm $ln\Lambda \simeq 20$. It is necessary to find the highest value of T_e and the lowest value of n_e that maximize τ_s to obtain the highest value of the efficiency in (2.5). The slowing down time computed for the DTT reference plasma scenario (see section 2.1.1) is $\tau_s \sim 0.13$ s. All these theoretical considerations are applied in chapter 3, where several numerical studies for different DTT plasmas and NBI energies will be presented.

2.2.4 Particle losses

During the ionization and slowing down processes, injected particles could be lost in different ways. Among them it is possible to distinguish SOL losses, which affect fast ions born outside the confined plasma region, the Scrape-Off Layer (SOL). Here, fast ions find open magnetic field lines that bring them to collide with divertor plates, unless favorable drifts or collisions bring EPs back to confined orbits. Particles are lost also if they born in non-confined orbits. This kind of losses are known as first orbit losses. Banana orbits, i.e. the trapped particle orbits, are the main type of orbits affected by these losses, since one part of the banana could cross the separatrix. The amount of these losses results from the direction of the neutral beam injection into the plasma. A co-current injection involves a significant reduction of this type of loss since the bananas close inwards. This will be better explained in the following section. If fast ions collide with neutral particles in the plasma, it is possible to observe particle losses known as charge-exchange losses. Indeed, in the charge-exchange process fast ions become fast neutrals, which have a lower probability of being ionized, as can be seen in figure 2.8. Orbit losses describe instead losses of confined particle which, after collisions with plasma particles or by drift effects, move to non-confined orbits. Analyses in this thesis are performed on a collisionless plasma, since in EPs slowing down time is greater than the time required by a fast ion to complete a toroidal turn, defined as $\tau_{tor} \sim 2 \times 10^{-6}$ s. Shine-through losses are the last kind of particle losses treated here. Shine through losses affect not ionized beam particles which cross the plasma arriving to the device opposite wall. This kind of losses is related on the plasma density. Indeed, the lower the plasma density, the higher the probability that injected neutrals pass through the plasma without being ionized. Possible damage to the device can occurs if the fraction of shine-through losses produce an harmful heat load on the wall. This thesis mainly deals with first orbit and shine-through losses. Numerical studies of EPs behavior after the neutral beam injection will be discussed in chapters 3 and 4, to investigate the particles losses affecting the NBI-plasma interaction. To a better comprehension of the results, in the next section an overview of the motion of EPs in a fusion plasma is discussed, deepening drift effects suffered by EPs and orbit typologies that fast ions can follow.

2.3 Confined EPs motion and orbits

The injection of neutral particles into a plasma gives rise to a superthermal population of energetic particles. As the plasma particles, fast ions are charged particles that feel the presence of magnetic fields. Therefore they behave similarly to plasma ions and electrons, making helical trajectories

around the magnetic field lines but with an higher radial excursion due to their higher energy[3]. The importance on the study of EPs concerns their similarity to the alphas, the energetic particles that born from fusion reactions (He^4 in (1.4)). The alphas heat the plasma representing one fifth of the total fusion power. The velocity distribution functions of alphas and EPs are different: alphas are born isotropically, while EPs velocity distribution is peaked in the injection direction. The high energy of EPs determines different behavior than that of thermal particles when they move inside the plasma. EP orbits are mostly affected by the presence of drift effects, derived from the characteristics of magnetic fields that confine the plasma or from the presence of an electric field. This determine the definition of new particle orbits, such as potato or stagnation orbits [23]. In the next subsections, a general description of drifts that influence the motion of particles and EP orbits is given.

2.3.1 Particle motion

Consider a fast ion with mass m and charge q moving inside a plasma magnetically confined by an uniform magnetic field. The particle trajectory is studied starting from the Newton's motion equation in which the Lorentz force is involved

$$m\frac{d\vec{v}}{dt} = q\vec{v} \times \vec{B} \tag{2.8}$$

The particle initial velocity is $\vec{v} = (v_\perp, v_\parallel)$ with $\perp$, $\parallel$ components defined with respect to the magnetic field $\vec{B}$. The single-particle motion of fast ion is a superposition of two motions, called Gyro-Orbit (GO) and Guiding Center (GC) motion. Charged particles feel a perpendicular force that determines a circular motion around magnetic field lines. This is called gyro-orbit motion. Quantities that characterize the GO motion are the Larmor radius r_L and the gyro-frequency, or cyclotron frequency, ω_c, respectively defined as the radius of circular motion and its characteristic angular frequency

$$r_L = \frac{mv_\perp}{|q|\mathrm{B}} \qquad\qquad \omega_c = \frac{|q|\mathrm{B}}{m}$$

The Larmor radius must be small compared to the typical macroscopic dimension of the plasma in order to have a good confinement of particles. In DTT device, the Larmor radius, reported in table 1.2, is of the order of 10^{-6} m [15]. Particles follow a circular motion around a centre called guiding centre. This point moves in the parallel direction with respect to the magnetic field in case of the presence of an initial parallel velocity $v_\parallel$. The uniform constant motion of particle is known as guiding center motion. The velocity of the guiding center can be modified by the presence of spatial and time variations of B. The resulting effect is the presence of a drift velocity component v_d which modifies the guiding center trajectory, determining in the worst case particle losses.

2.3.2 Particle drifts

The presence of an external force acting on particles moving inside the plasma determines the drift of the guiding centre. In general indeed, considering a uniform external force $\vec{F}$ perpendicular to the magnetic field, the equation of motion for a particle becomes

$$m\frac{d\vec{v}}{dt} = q\vec{v} \times \vec{B} + \vec{F} \tag{2.9}$$

Solving this equation turns out that the perpendicular motion of particles is affected by a drift equal to

$$\vec{v}_F = \pm\frac{\vec{F} \times \vec{B}}{B^2} \tag{2.10}$$

where $\pm$ defines the dependence on the charge sign (+ for positive particles, - for negative particles). External forces can act on particles when some spatial or time variations[4] of the magnetic fields occur. These external forces, as the gradient or centrifugal forces, are responsible for the guiding center shift.

[3] The Larmor radius of the gyro-motion is proportional to the particle energy, $r_L \propto E$

[4] Spatial variations of the magnetic field occur on a long length scale compared to the Larmor radius while time variations on a shorter time that the inverse of the gyro frequency

Also the presence of an electric field can determine a drift, due to the electric force that acts on particles. Therefore, it is possible to distinguish four different drifts, described in details below, that, combined, result in a total contribution v_d to the guiding center motion given by

$$\vec{v}_d = \vec{v}_{\nabla B} + \vec{v}_k + \vec{v}_E + \vec{v}_p$$

Gradient drift The presence of a gradient in the magnetic field leads to a drift of the particle guiding center in the perpendicular direction of B and the gradient itself. In particular, the velocity contribution given to the guiding center velocity is defined as

$$\vec{v}_{\nabla B} = \mp \frac{v_\perp^2}{2\omega_c} \frac{\vec{B} \times \nabla B}{B^2} \tag{2.11}$$

where ω_c is the gyro-frequency, associated to the gyro-motion of particle. The sign $\pm$ defines that positive and negative particles move in opposite directions.

Curvature drift When the magnetic field is characterized by a constant radius of curvature $\vec{R}_c$, as in toroidal geometry, the GC drifts perpendicularly to the plane in which the curvature lies [22]. The presence of a centrifugal force acting on particles, given by $\vec{F}_c = -m v_\parallel^2 \frac{\vec{R}_c}{R_c}$, determines a drift velocity equal to the following relation

$$\vec{v}_k = \mp \frac{v_\parallel^2}{\omega_c} \frac{\vec{R}_c \times \vec{B}}{R_c^2 B} \tag{2.12}$$

Also this contribution depends on the charge sign sgn(q) and on ω_c.

ExB drift The presence of an electric field $\vec{E}$, perpendicular to $\vec{B}$, determines a drift perpendicular to both fields [22]. In this case, the shift is defined by the following velocity contribution

$$\vec{v}_E = \frac{\vec{E} \times \vec{B}}{B^2} \tag{2.13}$$

which is charge and mass independent, meaning that both positive and negative charges drift in the same direction. Inside a toroidal solenoid, ions and electrons feel opposite curvature and gradient drifts. This charge separation creates a vertical electric field $E \neq 0$. Therefore, particles are affected by the E×B drift. This can cause poor confinement without the presence of a poloidal magnetic field, introduced to solve E×B drift problem twisting the magnetic field lines in an helical shape. This effect on the field is also called as rotational transform. In this way, particles will have a zero net vertical drift after a poloidal turn.

Polarization drift If electric and magnetic field are time dependent and vary slowly in time, the polarization drift arises from the particle inertia and modifies the guiding center motion according to the following expression

$$\vec{v}_p = \mp \frac{1}{\omega_c} \frac{d}{dt} \left(\frac{E_\perp}{B} \right) \tag{2.14}$$

where $E_\perp$ is the perpendicular component of the electric field. The contribution is charge dependent.

In figures 2.10 and 2.11, the drift effects on the particle motion just described are represented.

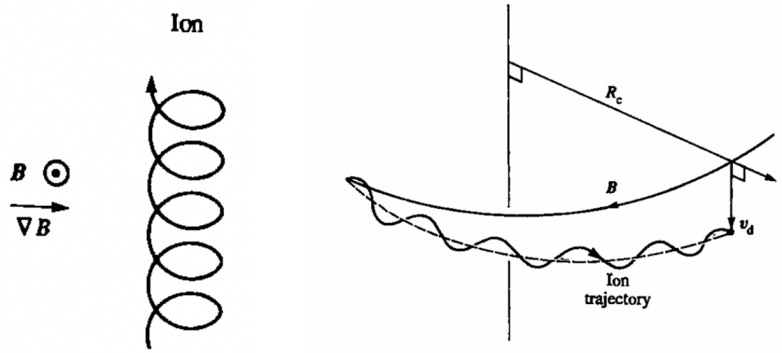

Figure 2.10: Sketch of gradient (left) and curvature (right) drift effects felt by ions [22].

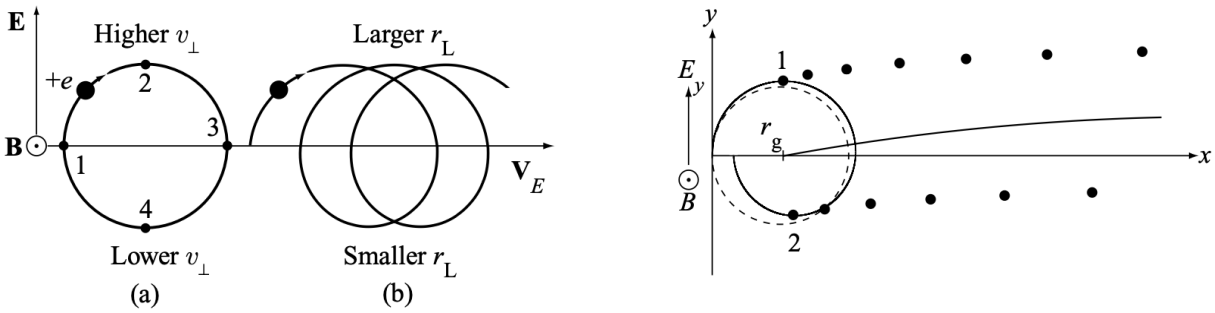

Figure 2.11: Sketch of E×B (left) and polarization (right) drift effects felt by ions [3].

Drift relations (2.11)-(2.12) are defined in terms of $v_\perp$, $v_\parallel$. The definitions of the perpendicular and parallel kinetic energy as $E_\perp = \frac{1}{2}mv_\perp^2$ and $E_\parallel = \frac{1}{2}mv_\parallel^2$ show a direct proportionality with the particle energy for both gradient and curvature drifts. For this reasons, EP drifts are greater than those of thermal particles and, as consequences, the deviation from their initial position is one order of magnitude larger [23]. In particular, this affects types of orbits that fast ions can follow, treated in the following subsection.

2.3.3 Orbit typologies

Plasma particles can be classified as passing or trapped particles. The former are particles that complete a toroidal orbit; the latter are trapped between two toroidal positions and bounce from one to the other without complete a lap in the toroidal plane. This is due to a magnetic mirror effect similar to that of linear magnetic field devices. The projection of the particular orbit of a trapped particle in the (R,z) plane gives a banana shaped orbit, as can be seen in figure 2.12. If a particle is trapped or passing depends on its initial velocity and position. Inside the tokamak plasma, the magnetic field is not uniform along the radial coordinate R. Indeed it follows a 1/R dependence and, in the inner part of the torus, the intensity is higher. Trapped particles invert their trajectory to preserve their energy and magnetic moment, defined as $\mu = \frac{1}{2}\frac{mv_\perp^2}{B}$, when they feel an high magnetic field intensity. The magnetic moment in particular can be considered as an adiabatic invariant since in DTT its value remains approximately invariant during slow time variation of magnetic field in the system (see section 4.4.1). Another constant of motion for an axisymmetric geometries, as the toroidal geometry, is the canonical toroidal angular momentum $P_\phi = mRv_\phi + q\Psi$, where v_ϕ is the toroidal velocity that is assumed equal to $v_\parallel$ in the guiding center approximation [25]. Both the magnetic moment and the canonical angular momentum will be used in the chapter 4 to describe the topological map of EP orbits in a collisionless approximation, which is particularly useful to characterize first orbit losses, a fraction of losses unavoidable and fully determined by EP orbit topology.

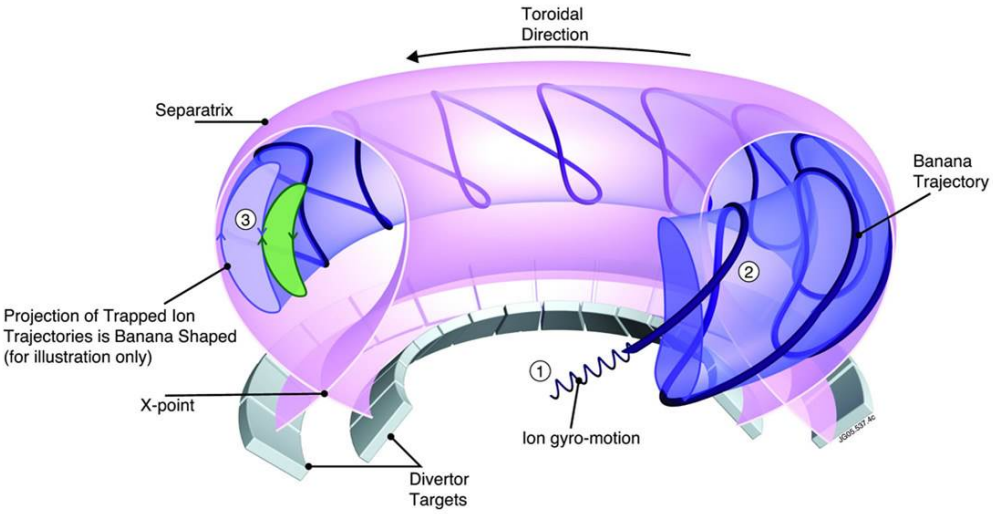

Figure 2.12: Representations of banana trajectory along the toroidal direction and its poloidal projection [24].

Differently from thermal particles, EPs move inside the plasma following several types of orbits. Indeed, due to large drifts related to EPs, it is possible to distinguish not only banana or passing orbits but also stagnation and potato orbits. Additionally, some particles could be lost due to the drift effects that push them towards the wall defining lost orbits. One important quantity that allows to determine the nature of orbits is known as pitch, defined as $\lambda = \frac{v_\parallel}{v}$, with velocity $v = \sqrt{v_\parallel^2 + v_\perp^2}$. As convention, it is assumed that positive pitch ($\lambda > 0$) characterizes particles moving with $v_\parallel$ in the same direction of the magnetic field. $\lambda > 0$ particles are called from now on *co-moving particles*. Negative pitch ($\lambda < 0$) defines particles moving in the opposite direction of B, called instead *counter-moving particles*. A brief description of EP orbit typologies is provided, considering the projection on the (R,z) plane of the trajectories traced by particles in the plasma in the GC reference. In figure 2.13 it is possible to observe all the possible orbits described below [26].

Passing and Banana Orbits When a particle completes a toroidal orbit maintaining the sign of its parallel velocity $v_\parallel$ constant, it is called passing particle. A particle that doesn't complete a toroidal orbit is characterized by a change on the sign in the parallel velocity. At some point of its trajectory, called bounce point, particle turns back to preserve energy and magnetic moment, which conservation relations are respectively

$$\left(v_\parallel^2 + v_\perp^2\right) = v_b^2 \tag{2.15}$$

$$\frac{v_\perp^2}{B} = \frac{v_{\perp,b}^2}{B_b} \tag{2.16}$$

where b subscript stays for bounce-point quantities, with $v_b^2 = v_{\parallel,b}^2 + v_{\perp,b}^2$. The condition for the switchback is $v_{\parallel,b} \ll v_{\perp,b}$ and therefore $\lambda \sim 0$. When a particle satisfies it during its trajectory around the torus, it becomes a trapped particle, characterized by an orbit with a banana shape in the poloidal plane. The condition to determine if a particle is trapped or passing depend on the magnetic field at the bounce point B_b. Indeed if $B_b < B_{max}$, where B_{max} is the maximum value of the magnetic field for a given flux surface, then the particle is trapped. This condition can be translated using the equations (2.15) and (2.16) such as

$$\frac{v_\parallel^2}{v^2} < 1 - \frac{B_{min}}{B_{max}} \tag{2.17}$$

where B_{min} is the minimum B for a given flux surface and $v_\parallel$ the initial parallel velocity. From the definition of the pitch, it is also possible to write equation (2.17) in terms of λ such as

$$-\sqrt{1 - \frac{B_{min}}{B_{max}}} < \lambda < \sqrt{1 - \frac{B_{min}}{B_{max}}}$$

B_{max} and B_{min} are defined for a given flux surface. They can be parameterized with respect to the normalized flux coordinate ρ_{pol}, defined as

$$\rho_{pol} = \sqrt{\frac{\Psi - \Psi_{ax}}{\Psi_a - \Psi_{ax}}} \tag{2.18}$$

where Ψ represents the poloidal flux contained within a contour outlined by constant pressure value. Ψ_{ax} and Ψ_a describe the poloidal flux surfaces respectively at the magnetic axis and the last closed flux surface (see chapter 4 for a detailed description of these quantities). The parametrization [27] is given by

$$\frac{B_{max}}{B_{min}} = \frac{1 + \frac{a}{R_0}\rho_{pol}}{1 - \frac{a}{R_0}\rho_{pol}}$$

where a and R_0 are respectively the minor and major radii of the machine. The banana width is of particular importance to distinguish between different kind of trapped particles (banana or potato orbits). Defining r as the mean radius of a given flux surface, the banana width is defined by $\delta_b \sim \frac{q(r) r_L}{\sqrt{\epsilon}}$ where $\epsilon = \frac{r}{R_0}$ is the inverse aspect ratio and $q(r)$ the safety factor. This definition allows to distinguish when a trapped particle follows a banana or potato orbits, as can be seen later. Examples of passing and banana orbits are reported in figure 2.13: *a, b, h, k, l* are confined passing particles while trajectory *e* represents a banana orbit.

Stagnation Orbits If a particle completes a toroidal orbit scarcely moving poloidally, and without encircling the magnetic axis, as usually happens for passing particles, its trajectory is called stagnation orbit. The $\mathrm{sgn}(v_\parallel)$ remains constant but the vertical shift due to gradient and curvature drifts nearly cancels the poloidal component of the parallel motion along the field lines outside of the magnetic axis [23]. Letter *f* in figure 2.13 represents a stagnation orbit.

Potato Orbits A trapped particle characterized by the change of $\mathrm{sgn}(v_\parallel)$ but whose trajectory encircles the magnetic axis follows a potato orbit. These kind of orbits are characterized by a larger width than those of banana trapped particles, determining the inclusion of the magnetic axis during their motion around the torus. This happens when $\delta_b \geq r$. Under this condition indeed, the banana approximation fails In this case the width is defined as

$$\delta_p = \left(\frac{2q(0)v_{\perp,0}}{\Omega_0 R_0}\right)^{2/3} R_0$$

where $v_{\perp,0} = \sqrt{\frac{2\mu B_{ax}}{m}}$, $\Omega_0 = \frac{ZeB_{ax}}{mc}$ is the ion cyclotron frequency and B_{ax} the magnetic field at the magnetic axis [28]. An example of potato orbit is shown in figure 2.13 by the trajectory *g*.

Lost Particles When a particle collide with the wall, it is considered lost. This happens because of the drifts which force particles to shift from their initial flux surface. Co-moving and counter-moving particles are characterized by a different loss boundary depending on their drift direction. Also the direction of the neutral beam injection plays an important role in the amount of lost particles. Indeed, counter-current injection is affected by a large number of first orbit losses, i.e. fast ions that born in a non-confined particles. To avoid these harmful losses, co-current neutral beam injection is required. Through a co-current injection indeed trapped particles close their banana trajectories inwards, regardless of their motion with respect to the magnetic field. Considering a collisionless plasma, when particles are lost outside the LCFS are considered lost particles. In the presence of collisions instead particles can leave the border but re-enter due to collisions with other particles in the SOL. Some example of lost particle orbits are depicted in figure 2.13. Lost orbits are defined by letters *c, d, j, i, m*. Letter *c* in particular identifies one lost trapped orbit while all the others represent lost passing orbits.

The EPs behavior inside plasma is complex. Numerical studies about the motion of fast ions injected in the plasma by means of the NBI system are extremely important for the development of an efficient use of the NBI system. The modelling of EPs can be done through the orbit-following Monte Carlo code ASCOT, introduced in the next section.

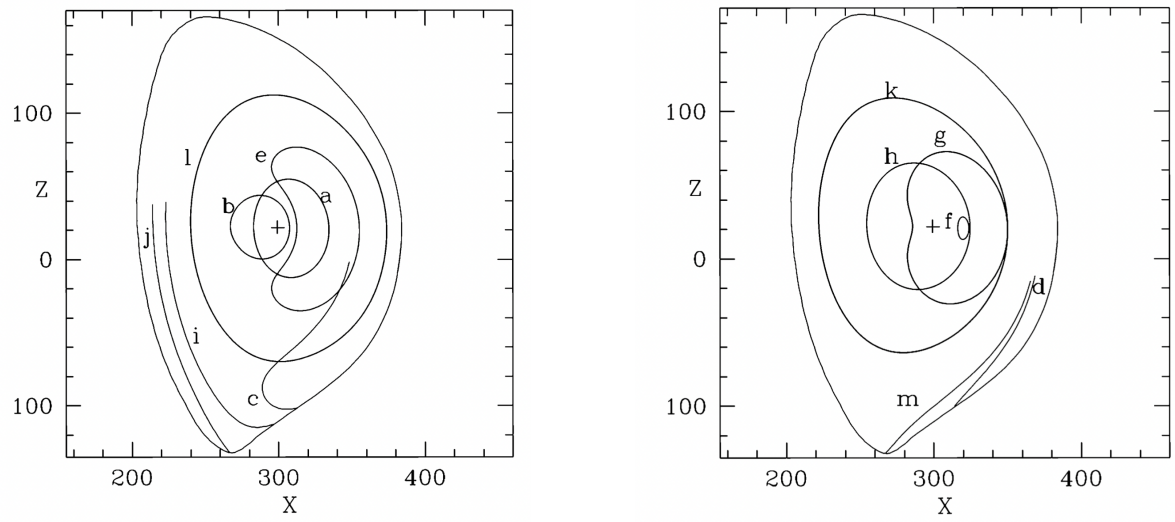

Figure 2.13: In both graphs projections on the the (X,Z) plane of the trajectories traced by EPs in plasma are presented. **Left.** *a, b, l* are confined passing particles; *j, i* are lost passing particles; *e* is a confined trapped particle; *c* is a lost confined particle. **Right.** *h, k* are confined passing particles; *d, m* are lost passing particles; *g* follows a potato orbit; *f* is a stagnation orbit. [26]

2.4 EPs modelling: ASCOT Monte Carlo code

Numerical applications on DTT device performed in this thesis are done using the orbit-following Monte Carlo ASCOT code [29]. ASCOT was developed in Aalto University, Finland, and it is used to study the behavior of energetic particles, as the ones obtained by the NBI, the alphas or fast ions derived from the ICRH system. ASCOT solves the time evolution of the particle distribution function $f(\vec{\mathbf{z}}, t)$, where $\vec{\mathbf{z}} = (\vec{\mathbf{r}}, \vec{\mathbf{v}})$ is the particle phase space and t the time. The code follows Monte Carlo test particles integrating numerically the equation of motion, both in the gyro-orbit (GO) reference and in the guiding center (GC) reference, as it will be described below. ASCOT works with real 3D geometry of the machine, injector systems and magnetic field [10]. This code was used to simulate NBI fast ions in the most relevant fusion devices, including ITER and JET. ASCOT is applied here to DTT as a stand-alone code for the study of the NBI EP population using a "frozen" background plasma and the work in this thesis represents the first applications of this code to DTT device. In the following, a detailed description of the kinetic equation solutions, the inputs required to the ASCOT code and the consequent outputs is given. Finally a brief discussion about similar codes is presented.

2.4.1 Kinetic equation solver

ASCOT code solves the kinetic equation of charged particles in the GO and GC references. The kinetic equation describes the time evolution of the distribution function of minority particle species, represented by an ensemble of Monte Carlo test particles. In this thesis, the minority particle species considered are the fast ions obtained from NBI. Their kinetic equation is given by

$$\frac{\partial f}{\partial t} + \dot{\mathbf{z}} \cdot \frac{\partial f}{\partial \mathbf{z}} = \left(\frac{\partial f}{\partial t}\right)_{coll} \tag{2.19}$$

where $\dot{\mathbf{z}}$ stands for the equation of motion and $\left(\frac{\partial f}{\partial t}\right)_{coll}$ describes the Coulomb collision effects[5] on the distribution function [30]. The phase space volume is conserved by the equation of motion, according to the Liouville theorem, and therefore it is possible to rewrite equation (2.19) as the Fokker-Planck equation, which describes the probability evolution related to finding a test particles in a certain

[5]Charge-eXchange (CX) losses are not treated on the ASCOT version used for the analysis in thesis. However, due to the high plasma electron density in DTT, the CX losses are negligible.

location $\mathbf{z}$ when the motion is described by a stochastic process. The Fokker-Planck equation is

$$\frac{\partial f}{\partial t}(\mathbf{z},t) = -\frac{\partial}{\partial \mathbf{z}}\left[\mathbf{a}(\mathbf{z},t)f(\mathbf{z},t)\right] + \frac{\partial}{\partial \mathbf{z}}\frac{\partial}{\partial \mathbf{z}}\left[\mathbf{c}(\mathbf{z},t)f(\mathbf{z},t)\right] \tag{2.20}$$

where $\mathbf{a}$ contains also the equations of motion $\dot{\mathbf{z}}$. The solutions of (2.19) and (2.20) are obtained considering many random test particle paths and making an average over them [30]. ASCOT solve the equation of motion for the full GO motion and GC motion. The main difference between these two motions concerns the time computation demand. The GO case indeed requires a huge computational effort since particles are followed for millions of oscillation periods. In the GC approach, the computational demand is reduced since only the particle guiding center is followed by ASCOT and oscillations of this point have a larger time scale than that of the full gyro orbit case. Both approaches can be used together in the so called hybrid mode. To study for example the wall power load due to EP losses there may be some uncertainties with the GC motion due to the presence of particles whose guiding center is closer than a Larmor radius r_L to the wall boundary. This means that, according to the guiding center approximation, particles remain confined even if in the GO motion they are lost on the wall. In this particular case, the hybrid approach is applied: when the particle guiding center is closer than r_L from the wall, then the code starts to follow the GO approximation [30]. This approach is time saving and so allows a better estimation of the power load to the wall. Hydrid mode is the usual setting of ASCOT code in this thesis.

2.4.2 BBNBI code for beam ionization

The initial test particle ensemble for ASCOT is obtained with BBNBI, a neutral beam ionization model. BBNBI [31] is an independent tool capable of following the injected neutrals until ionized. BBNBI uses the same plasma input as ASCOT. BBNBI follows neutrals starting from the NBI accelerator grid until their ionization, taking into account also the ionization outside the LCFS and providing information about shine-through losses. The beam representation is beamlet-based, meaning that it is modelled by a set beamlets for which source location and direction are defined individually. The beamlet divergence and the injection probability can be specified too. The DTT NBI in particular is composed by 1360 beamlets with a single-beamlet divergence of 6 mrad. Others neutral beam models can be used as test particles generators for ASCOT, as PENCIL [32] or FAFNER [33]. However, the magnetic field and plasma background structures are not the same of those used by ASCOT and, in this sense, the BBNBI test particle ensemble is more suitable for ASCOT studies.

2.4.3 Input and output structures

The Input/Output (I/O) structure for ASCOT is now presented. Main inputs required for ASCOT code are defined in table 2.3. These are the same inputs used also by BBNBI, apart for the test particle ensamble input that is the BBNBI output used by ASCOT. The magnetic field is computed starting from the information contained into the EQDSK format file written by the CREATE-NL free boundary code [34]. The EQDSK stores also first wall and last close flux surface coordinates. The plasma kinetic profiles are instead obtained by 1.5D transport simulations [16].

The outputs given by ASCOT are different N-dimensional histograms called distributions. Most of them are produced as radial profile in 1D with respect to the normalized poloidal flux ρ_{pol} or 2D coordinates (R,z). The larger dimension of distribution is a 6-D histograms, where time and test particle species are the two dimensions common to all distributions and the other 1-4 dimensions are used to specify the coordinates of the phase space of interest. In table 2.4, outputs of interest for this thesis are reported. For further information about ASCOT outputs, see [30]. In chapters 3 and 4, numerical applications of ASCOT code to DTT NBI system to study EP population will be presented and described in details.

Input	**Description**
Magnetic field	Toroidal and poloidal magnetic field (2D or 3D)
Plasma kinetic profiles	Plasma scenario that contains information about the electron and ion temperatures and densities
First wall coordinates	Geometry of the tokamak first wall used to check collisions between test particles and the wall (2D or 3D)
Test particle ensemble	Contains information about markers to be simulated by ASCOT
Option parameters	Simulation parameters
Injector geometry	Beamlet geometry in 3D

Table 2.3: Main inputs used by the orbit-following Monte Carlo ASCOT code.

Output	**Description**
Power deposition	Power distribution of injected particles on the background plasma particles. ASCOT provides information on the power deposited to the different species of particles present in the plasma (ions, electrons, impurities).
Injected toroidal current	Total toroidal current by NBI Current Drive (CD).
Injected torque	Total torque provided by the NBI.
Orbit losses	Information of particles that are lost during the thermalization process.
Test particle information at different timestep	Contains all the information about markers (GO and GC positions, velocities, energy, pitch, etc...) written at specified timestep of the simulation. Without any specified timestep, ASCOT saves information at the initial state (inistate) and final state (endstate) of the simulation.

Table 2.4: Some of the outputs provided by the orbit-following Monte Carlo ASCOT code.

2.4.4 Other orbit-following and analytical codes for beam-plasma interaction studies

The Fokker-Planck (FP) equation of EPs distribution function can be computed using different approaches and different levels of approximations. It is possible to distinguish between codes that use a orbit-following Monte Carlo approach or those that use an analytic solution of the FP equation. The main differences between these two approaches concern the computational time demand and the accuracy of the result. The high accuracy of orbit-following codes requires a huge computational effort; on the contrary, analytic codes solve an orbit averaged Fokker-Planck equation with less accuracy and lower computational time. Some examples of code that use a orbit-following Monte Carlo approach other than ASCOT are NUBEAM [35] and SPOT [36]. RISK [37], RABBIT [38] and METIS [39] are instead examples of code that use an analytic approach. NUBEAM, as ASCOT, follows test particles up to a certain temperature, below which they are considered thermalized, in the GC approximation. RISK is based on the approximation related to finite orbit width effect. RISK computational time is longer than RABBIT, that use more approximations than RISK to make real time simulations ($\sim$25 ms per time step). The main approximations adopted by RABBIT concern a simple beam geometry, a reduced number of orbit ($\sim$ 20 orbits are computed per beam energy component) for the orbit average of the beam deposition as well as the analytic solution of the FP equation. These codes are in good agreement with most of the analysis conducted with the higher accurate orbit-following codes, at least for 0D volume integrated quantities and 1D deposition profiles. To study EP losses, and in particular orbit losses, orbit-following codes are necessary. In the present work, ASCOT is chosen to perform the numerical analysis that will be presented in the following chapters.

Chapter 3

Numerical studies of energetic particles confinement and losses in DTT

After the overview given in chapter 2 about the NBI system and the EP behavior inside plasma, this chapter reports the numerical analysis performed for this thesis with ASCOT code to investigate the beam-plasma interactions. Several simulations were performed by modifying plasma temperatures and densities of the reference plasma scenario of DTT, illustrated in the previous chapter, or changing the injection energy of the beam. The plasma magnetic equilibrium is calculated by CREATE-NL free-boundary code [34] which saves the equilibrium information in the so-called EQDSK format. In this file the necessary information to build the magnetic field background are contained as well as the first wall and LCFS geometries, some of the inputs required for ASCOT simulations. The simulations were carried considering 50.000 test particles, which is the usual number of test particles for this kind of EP studies, in order to have a good statistics and an optimal computational time effort.

3.1 Plasma temperature scan

The first analysis consists on three different simulations performed keeping fixed the injection energy at $E_{\mathrm{NBI}} = 510$ keV and the particle densities profiles n_e, n_i as the reference scenario. Instead, the plasma temperatures T_e, T_i are changed as follow:

- **$\mathbf{T_e}$, $\mathbf{T_i}$ profiles of the reference plasma scenario** (see section 2.1.1);
- T_e, T_i multiplied by a factor 0.5;
- T_e, T_i multiplied by a factor 1.5.

In figure 3.1 the electrons temperature profiles for the three cases described above are shown as functions of the normalized poloidal flux coordinate ρ_{pol}. For simplicity of writing, from now on, only the electrons temperature will be reported in the following tables and figures. In table 3.1, the absorbed power, the NBI Current Drive (CD) and the injected torque are reported. These are 0D quantities obtained by ASCOT simulations.

Temperature	Absorbed Power [%]	NBI CD [A]	Injected torque [Nm]
0.50 T_e	99.93	1.17e+05	5.07
$\mathbf{T_e}$	**99.93**	**2.33e+05**	**5.14**
1.50 T_e	99.92	3.21e+05	5.15

Table 3.1: 0D quantities regarding beam-plasma interaction from ASCOT simulations at different temperatures. In bold, the reference plasma scenario data.

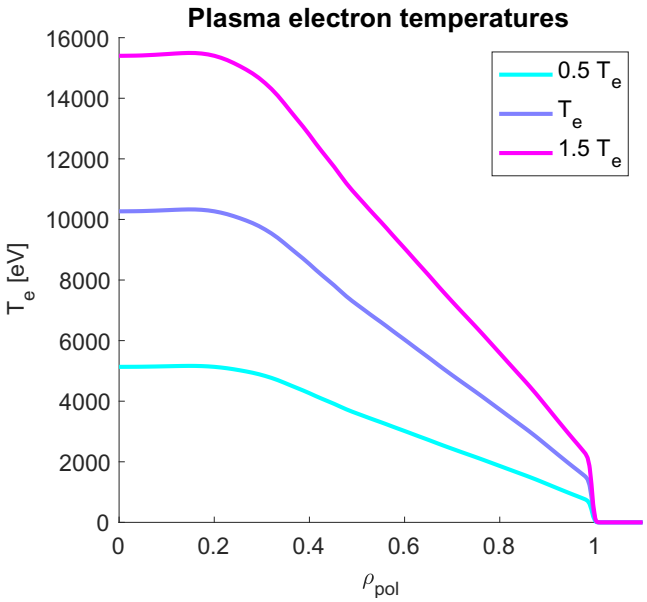

Figure 3.1: Electron temperature profiles used for the simulations at fixed n_e, n_i and E_{NBI}.

The absorbed power is the amount of power absorbed by plasma particles, as ions and electrons, from EPs during their slowing down process. The total power injected by NBI is equal to 10 MW. Almost 100% of it is transferred to plasma particles, as reported in table 3.1. The profile of the total deposited power density is shown in figure 3.2 as a function of the normalized poloidal flux coordinate ρ_{pol}.

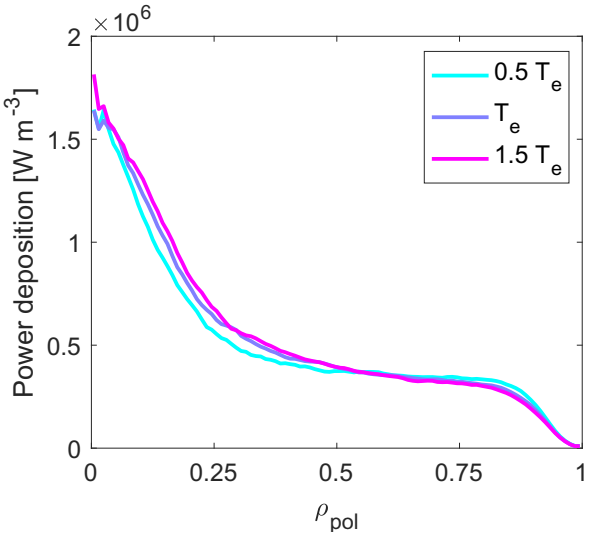

Figure 3.2: Radial profile of the total distributed power density for different plasma temperature scenarios.

To read this and the following density profile plots, it has to be noticed that the plasma volume (or area) considered at the edge ($\rho_{pol} \sim 1$) and at the core ($\rho_{pol} \sim 0$) are very different (at the core region is smaller than the edge). Therefore, considering 0D quantities (table 3.1), a small variation at the edge of the radial profiles has a stronger impact than larger variations in the plasma core. The same reason makes the curves more peaked in core region. More in details, table 3.2 shows the fraction of power transferred to plasma electrons and ions and figure 3.3 depicts the radial profiles of their relative power distributions. Observing the mentioned table and figure, the amount of power transferred to ions increases with the temperature T_e, while the power transferred to electrons decreases. To explain this, it is worth remembering that the critical energy E_c, defined in the previous chapter in equation (2.4), is proportional to T_e. As consequence, the ratio E_{NBI}/E_c decreases with the electron temperature keeping fixed E_{NBI}. Looking at the figure 2.9, this means that the fraction of injected power transferred

Temperature	Deposited power to electrons [%]	Deposited power to ions [%]
0.50 T_e	76.90	23.10
T_e	**61.67**	**38.33**
1.50 T_e	50.99	49.01

Table 3.2: Deposited powers to plasma electrons and ions during the slowing down process estimated with ASCOT for different plasma temperatures. In bold, the reference plasma scenario data.

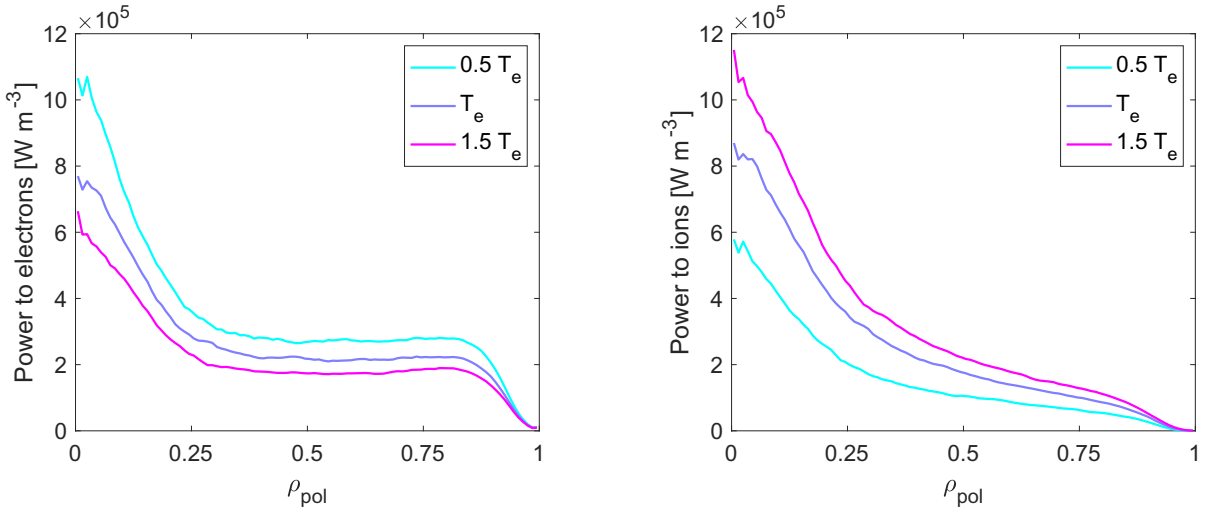

Figure 3.3: Radial profiles of power deposition to electrons and ions at different plasma temperatures.

to ions increases with T_e. Physically, this derives from the electron temperature dependence of the electron-beam collision frequency ν_{eb}. In particular, as reported in [3], in the approximation for the velocities $v_b \ll v_e$, where b, e subscripts refer respectively to beam and electron, the collision frequency is $\nu_{eb} \propto T^{-3/2}$. Therefore increasing the temperature of plasma electrons, the collision frequency between electrons and EPs decreases implying a decrease of electron power deposition.

For what concern the NBI current drive, whose values for the different cases are reported in table 3.1, it is possible to see an increase with T_e. In particular, from the lower value of the electron temperature 0.5 T_e to 1.5 T_e, the current is more than doubled, showing an increase of $\sim$ 170%. This effect derives from the characteristic of plasma to be a good conductor. The resistivity η of plasma, defined by [40], shows a $T_e^{-3/2}$ dependence. This implies that the higher the plasma temperatures, the higher the injected current, since the conductivity of the plasma increases if η is decreased. The same dependence is observed in the electron-beam collision frequency ν_{eb}, since the resistivity is obtained in [40] with a model based upon electron-ion collisions. Less collisions between plasma electrons and EPs means less resistivity for the current flowing into the plasma. In figure 3.4 the profile of total toroidal current density injected by the neutral beam is shown for the performed simulations as a function of ρ_{pol}. The last comment on quantities reported on table 3.1 concerns the injected torque. In particular, for the injection torque no significant changes are observed when the plasma temperature changes.

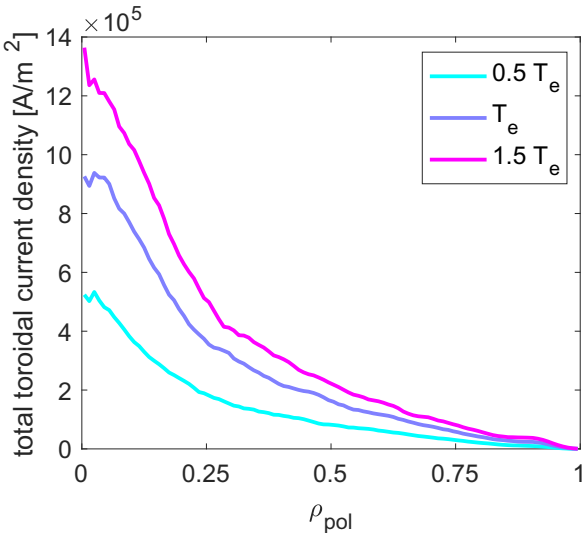

Figure 3.4: Radial profiles of the total toroidal current density at different plasma temperatures.

As last analysis for the plasma temperature scans performed, the critical energy is computed. Using the definition[1] reported on equation (2.4), curves in figure 3.5 are obtained. Due to the electron temperature dependence, the critical energy increases radially towards plasma center. As it can be easily seen in figure 3.5, the EP energy at 510 keV is larger everywhere than the critical energy, whose average value for the plasma reference scenario is $< E_c > \simeq 114$ keV, considering a volume average electron temperature at $< T_e > = 6.1$ keV. Integrating over the slowing down time to obtain the power deposition P_{NBI}, it can be noticed from figure 2.9 that $P_{\mathrm{NBI,e}} = P_{\mathrm{NBI,i}}$ at $E_{\mathrm{NBI}} \sim 2.5E_c$.In particular, when $E_{\mathrm{NBI}} > 2.5E_c$, the power is deposited mainly on electrons. In figure 3.6 curves for the critical energy multiplied by 2.5 are reported in order to provide a qualitative explanation. For 1.5 T_e and T_e cases, the E_{NBI} is larger than $2.5E_c$ only in a central portion of the plasma. At the core, the fast ion power is preferentially deposited on ions. This can be seen also in figure 3.3 where at some point along the radial position the power deposition to ions becomes larger than that deposited to electrons. This behavior is not observed in the lower plasma temperature scenario (0.5 T_e), where the power deposition to electrons is always larger and $E_{\mathrm{NBI}} > 2.5E_c$ along the radius.

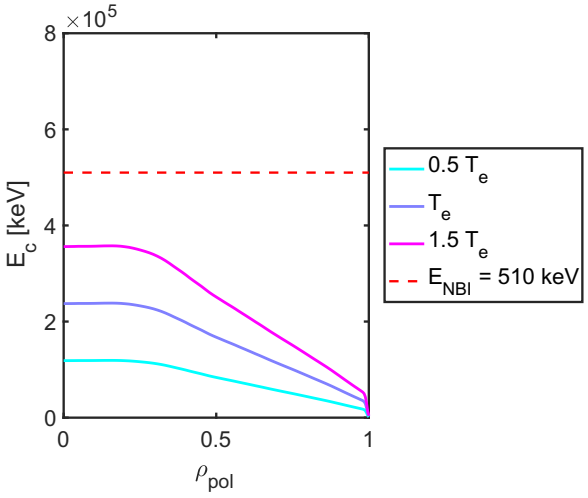

Figure 3.5: Radial profiles of the critical energy E_c at different plasma temperatures.

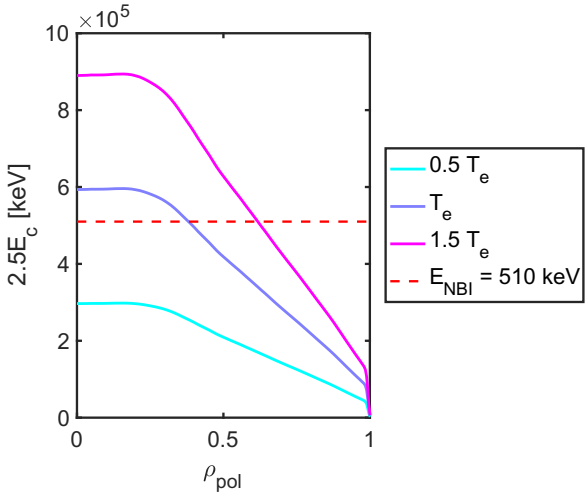

Figure 3.6: Radial profiles at 2.5 times E_c at different plasma temperatures.

[1]For deuterium plasma the constant factor 14.8 becomes 18.6 (see equation (2.4))

3.2 Plasma density scan

The scan over plasma densities was performed as second analysis. In this case, the injection energy is still $E_{\mathrm{NBI}} = 510$ keV and plasma temperatures are those of the reference scenario. The electron density is changed by multiplicative factors while a different computation has to be made for the ion density, due to the presence of impurities inside the plasma, as argon (Ar) and tungsten (W). Their contribution to the total ion density n_i is defined by the following relation

$$n_i = Z_D n_D + Z_{Ar} n_{Ar} + Z_W n_W \tag{3.1}$$

where $Z_D = 1$, $Z_{Ar} = 18$, $Z_W = 74$ are the relative charge numbers in the hypothesis of fully ionized impurities. Since a plasma is considered quasi-neutral, meaning that $n_e \sim n_i$, it is possible to compute the deuterium density n_D as follow

$$n_D = \frac{1}{Z_D}\left(n_e - Z_{Ar} n_{Ar} - Z_W n_W\right) \tag{3.2}$$

The impurity density ratios n_{Ar}/n_D, n_W/n_D are kept fixed. In figure 3.7, the ion densities of the reference plasma scenario are compared using a logarithmic scale.

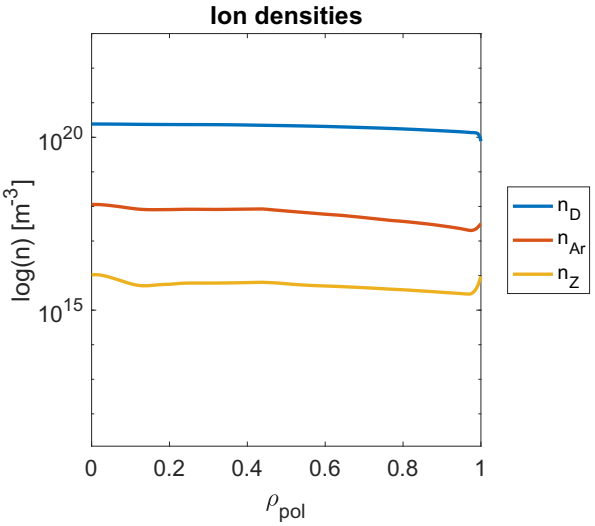

Figure 3.7: Density profiles of plasma ions (deuterium, argon and tungsten) in the reference plasma scenario.

Simulations were performed with the following conditions on n_e, used then to obtain n_i through equation (3.2):

- **$\mathbf{n_e}$ profiles of the reference plasma scenario** (see section 2.1.1);
- n_e multiplied by a factor 0.5;
- n_e multiplied by a factor 0.25.

The electron density profiles for the three cases described above are shown in figure 3.8, reported as a function of ρ_{pol}, while in table 3.3 the same quantities analyzed in the previous scan are reported: the absorbed power, the driven current obtained by NBI and the injected torque.

Density	Absorbed Power [%]	NBI CD [A]	Injected torque [Nm]
0.25 n_e	93.17	1.38e+06	4.96
0.50 n_e	99.64	6.72e+05	5.22
$\mathbf{n_e}$	**99.93**	**2.33e+05**	**5.14**

Table 3.3: 0D quantities regarding beam-plasma interaction from ASCOT simulations at different plasma densities. In bold, the reference plasma scenario data.

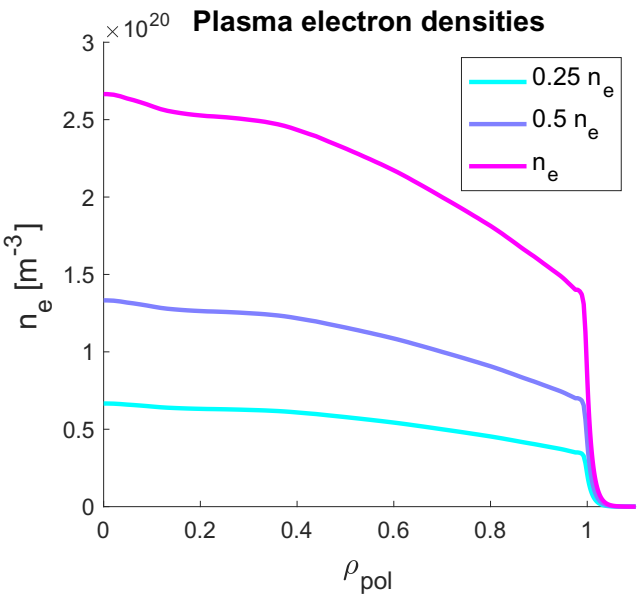

Figure 3.8: Electron density profiles used for ASCOT simulations at fixed plasma temperatures and E_{NBI}.

As in the previous scan on T_e, the injected power is equal to 10 MW. However, the absorbed power values in this analysis strongly depends on density, as can be seen in figure 3.9, where the total deposited power density profile is reported. As before, this radial profile is obtained dividing by a volume that, at the plasma core, is lower making curves peaked at the core.

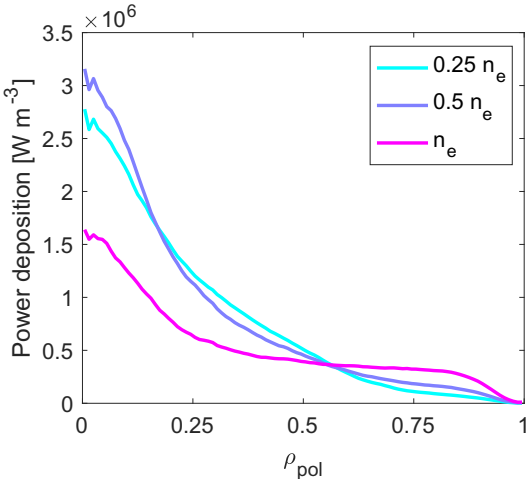

Figure 3.9: Radial profile of the total distributed power density for different plasma density scenarios.

The absorbed power differences derive from shine-through losses that occurs when neutrals are injected in a low density plasma. Indeed, at 0.25 n_e, the fraction of absorbed power is equal to 93.17%, corresponding to 9.32 MW, about 7% less than the absorbed power in the reference plasma scenario. This difference corresponds approximately to the power lost by the shine-through effect. As explained in section 2.2.4, shine-through losses happen when beam particles hit the first wall before being ionized. Their power is therefore considered lost. In a low density plasma, this happens because of the larger EP mean free path $\lambda \sim \frac{E_{\mathrm{NBI}}}{n_e}$ [41], which describes the characteristic distance travelled by neutral beam particles before ionization. The neutral ions probability to become lost particles increases when the density decreases since they travel a larger distance before ionizing. This fact can be also observed comparing the ionization clouds for the reference plasma scenario and the simulation with 0.25 n_e, reported in figure 3.10 and figure 3.11. These figures show respectively the (x,y) plane (top view) and the (R,z) plane (poloidal view) projections of neutral beam ionization points. For the lower density case, the ionization cloud is spread more inside the torus, reaching the first wall opposite the injection

position as can be seen in the top view projection.

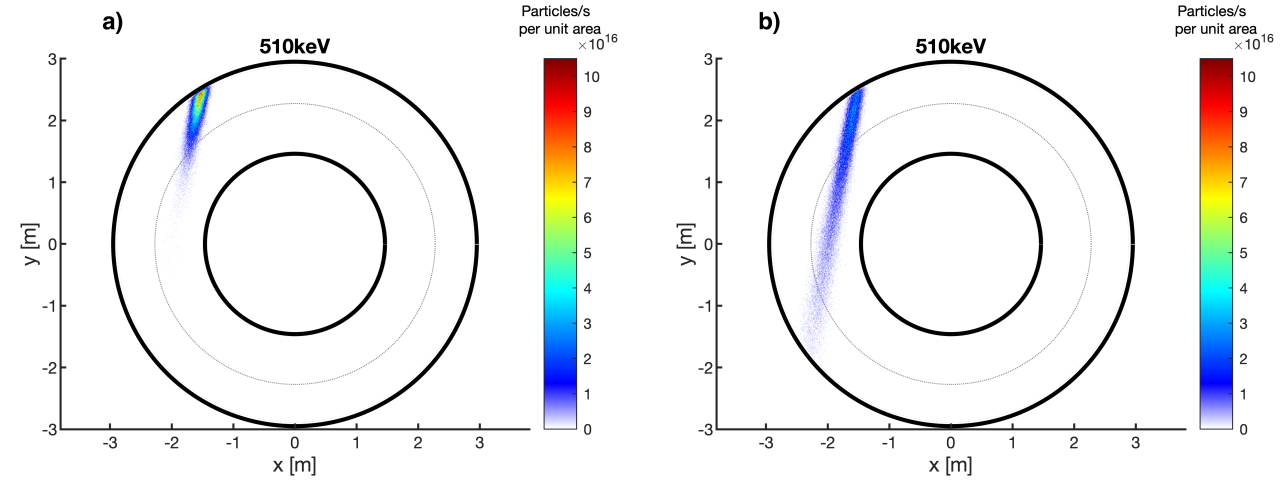

Figure 3.10: (x,y) projections of clouds of ionized particles derived from the neutral beam injection at 510 keV for different plasma density profiles. **a)** n_e, n_i of the reference plasma scenario. **b)** Reduced density case at 0.25 n_e.

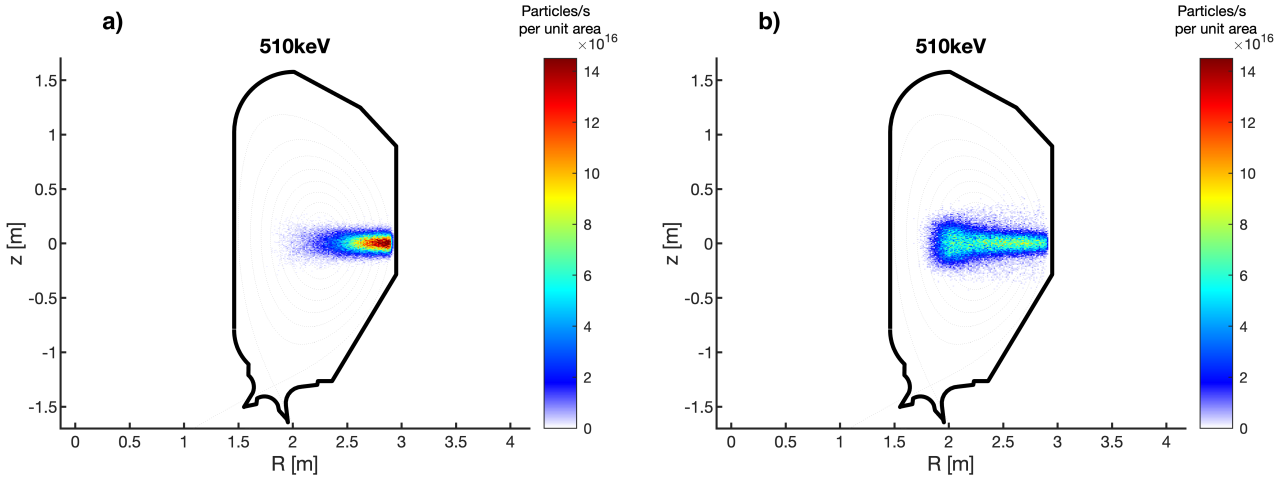

Figure 3.11: (R,z) projections of clouds of ionized particles derived from the neutral beam injection at 510 keV for different plasma density profiles. **a)** n_e, n_i of the reference plasma scenario. **b)** Reduced density case at 0.25 n_e.

In (R,z) projections it is worth noting that the particle density is larger at the plasma core for the simulation with 0.25 n_e. However, looking at (R,z) plane, it is important to take into account the effect of flux surfaces on the particle distribution. When particles cross the plasma, due to the tangential injection of the beam and the low density of the plasma, they cross the same flux surface in two different positions. Their spread, due to the beam divergence, is different being larger in the furthest point of flux surface crossing. This determines a larger and more spread particles distribution in the (R,z) projection, clearly visible especially for the lower plasma density scenario. This is reflected on the total power deposition: it is larger at the plasma core for lower plasma densities (see figure 3.9).

In table 3.4 the percentage of shine-through losses are reported for the three cases studied, showing an increase of losses decreasing n_e, as expected. Shine through losses as those of the lowest density scenario are potentially harmful for DTT since their power is localized on a relatively small NBI footprint area of about 0.25 m^{-2} [10]. The optimal situation to avoid device damages is the one at the reference plasma scenario where shine-through losses are $\sim 0\%$.

Density	Shine-through losses [%]	Shine-through losses [MW]
0.25 n_e	6.83	6.83e-01
0.50 n_e	0.33	3.35e-02
$\mathbf{n_e}$	**0.00**	**0.00**

Table 3.4: Shine-through losses in percentage and power at different plasma densities obtained with ASCOT. In bold, the reference plasma scenario data.

A detailed look to the deposition of the injected power to electrons and ions is reported on table 3.5. The fraction of power deposited to electrons increases with the density. Also in this case the explanation can be found in the electron-beam collision frequency ν_{eb} defined in [3]: the direct n_e dependence justifies the fact that electrons are mainly heated when the electron density increases. Radial profiles of the deposited power density to electrons and ions are shown in figure 3.12. For reference plasma scenario, power deposited to ions and electrons is larger at the plasma edge than at lower n_e.

Density	Deposited power to electrons [%]	Deposited power to ions [%]
0.25 n_e	54.58	45.42
0.50 n_e	59.30	43.70
$\mathbf{n_e}$	**61.67**	**38.33**

Table 3.5: Deposited powers to plasma electrons and ions during the slowing down process estimated with ASCOT for different plasma density scenario. In bold, the reference plasma scenario data.

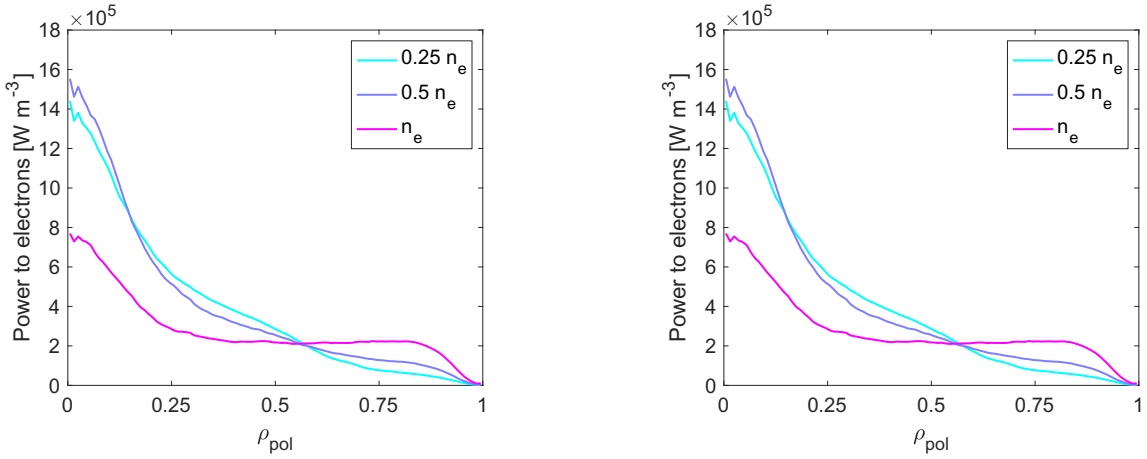

Figure 3.12: Radial profiles of power deposition to electrons and ions at different plasma density scenarios.

Regarding the current driven by NBI, from figure 3.13 it is possible to notice that the value of the current increases when n_e decreases. In particular, the driven current in a plasma with density n_e is reduced by 80% with respect to the driven current at 0.25 n_e, which reach a value around 1.4 MA at $0.25n_e$. The plasma resistivity doesn't depend on n_e but the CD efficiency η_{CD} does, as reported in the equation (2.5) which shows a dependence on $1/n_e$. This dependence actually derives from the

slowing down time definition where $\tau_s \sim \frac{1}{n_e}$ (see equation (2.6)): a lower density implies a longer slowing down process.

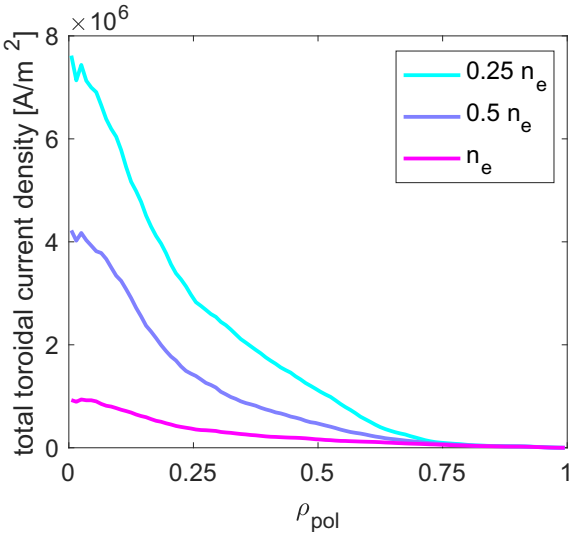

Figure 3.13: Radial profile of total toroidal current density at different plasma density scenarios.

In table 3.3 the values of the injected torque are reported. Differently from the plasma scenarios at different temperatures, the torque values change a little more. In particular, with respect to the reference plasma scenario, the injected torque for the scenario with 0.5 n_e increases of about 1.6%, while the injected torque for the scenario with 0.25 n_e decreases of about 3.5%.

As before, the critical energy is computed. Figures 3.21 and 3.22 depict the radial profiles of interest.

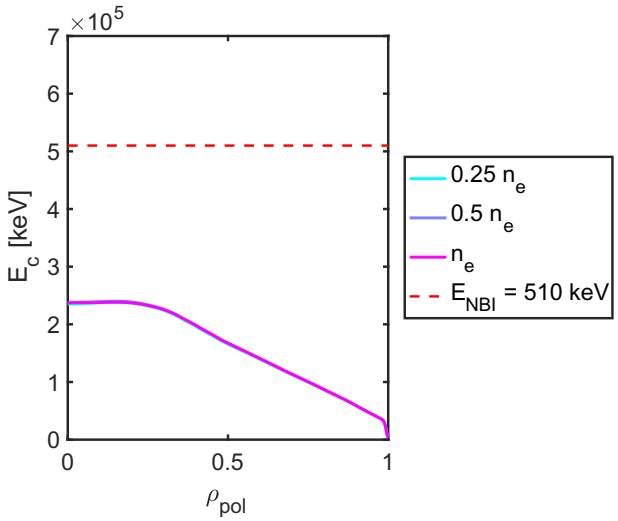

Figure 3.14: Radial profiles of the critical energy E_c at different densities.

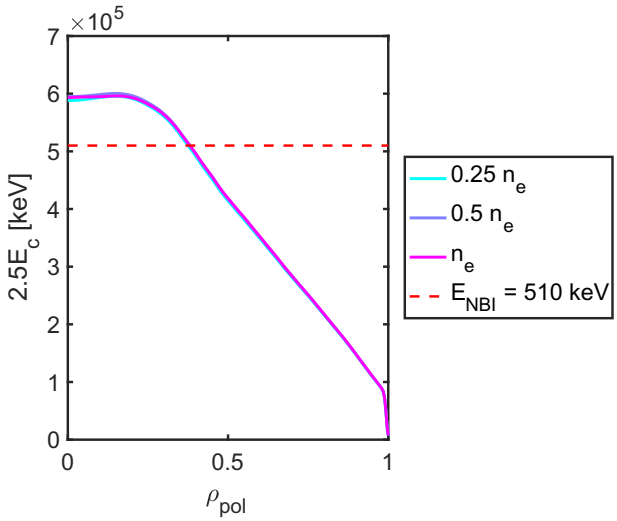

Figure 3.15: Radial profiles of 2.5 times E_c at different plasma densities.

Since E_c doesn't show an important dependence on n_e, (see equation (2.4)), the result of the computation, shown in figure 3.14, shows that E_c radial profiles for all the performed simulations with different plasma densities are approximately constant. Also in this case, the comparison of the beam energy E_{NBI} to $2.5E_c$ is performed, showing that $E_{\mathrm{NBI}} > 2.5E_c$ for all the cases above $\rho_{pol} \sim 0.4$ (figure 3.15), implying that, in this range, power is mainly deposited to electrons. Even if the injection energy is larger than $2.5E_c$ inside $\rho_{pol} \sim 0.4$ for all the studied scenarios, this doesn't imply that profiles of deposited power density, reported in 3.12, must be the same. The profiles indeed depends

on the position in which EPs are ionized by Coulomb collisions with plasma particles. At low density, a larger fraction of neutral ions are ionized closer to the plasma core. However, the position in which $P_{\mathrm{NBI,e}} = P_{\mathrm{NBI,i}}$ is the same for all the analyzed scenarios because doesn't depend on the radial profile itself but on the integrated value obtained from the profiles.

3.3 NBI energy scan

In the last analysis, beam energies E_{NBI} are changed, keeping fixed all plasma parameters as in the plasma reference scenario. In particular, three different beam energies are analyzed: the standard case at 510 keV and two lower beam energies, respectively of 400 keV and 300 keV. Indeed DTT NBI will be designed with the possibility to change the injection energy in a range between 250-510 keV, with a linear decrease of injected power, thanks to accelerator grid operation. In this section though, injected beam power is kept fixed to 10 MW, in order to easily compare the cases from beam-plasma interaction physics point of view. In table 3.6 the usual 0D quantities of interest are reported.

Beam Energy [keV]	Absorbed Power [%]	NBI CD [A]	Injected torque [Nm]
300	99.90	1.55e+05	6.60
400	99.93	1.96e+05	5.77
510	**99.92**	**2.26e+05**	**5.01**

Table 3.6: 0D quantities regarding beam-plasma interaction from ASCOT simulations at different beam energies. In bold, the reference scenario.

For all the E_{NBI} considered, the absorbed power is still $\sim 99.90\%$ of the injected power but the radial profiles change with the beam energy. The radial profile of the total deposition power density is reported in figure 3.16, where the dependence to the beam energy is clear.

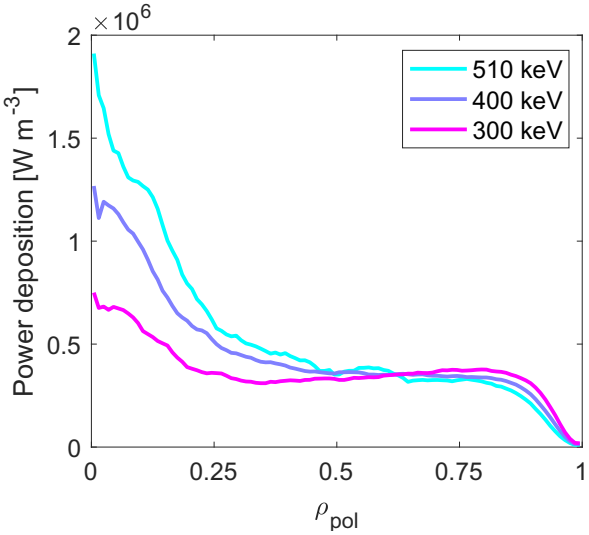

Figure 3.16: Radial profile of the total distributed power density for different plasma density scenarios.

Analyzing the fractions of energy transferred to plasma electrons and ions, it is possible to observe that increasing the NBI energy the percentage of power transferred to electrons increases, being always larger than that transferred to ions for all the studied cases. The relative values are reported on table 3.7.

Beam energy [keV]	Deposited power to electrons [%]	Deposited power to ions [%]
300	52.66	47.34
400	57.57	42.43
510	**61.80**	**38.20**

Table 3.7: Deposited powers to plasma electrons and ions during the slowing down process estimated with ASCOT for simulations with different NBI energies. In bold, the reference plasma scenario data.

This can be explained by looking at the beam-ion collision frequency ν_{ib} reported in [3]. In the approximation for velocities $v_i \ll v_b$, the collisionality ν_{ib} decreases if the velocity v_b is increased. Therefore, larger E_{NBI} implies lower ν_{ib} and so a lower power deposition to ions. Figure 3.17 shows radial profiles for fractions of power deposited to plasma electrons and ions.

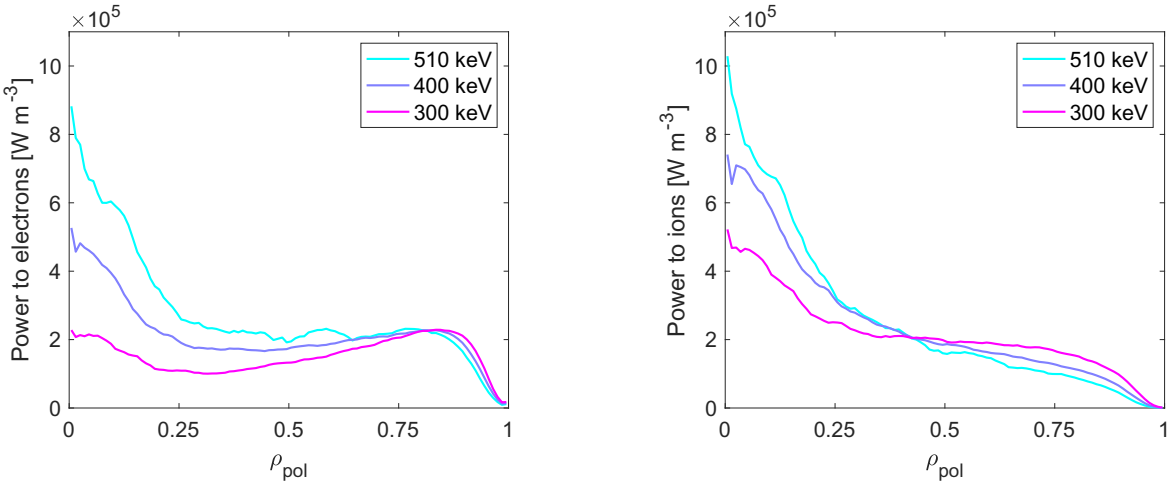

Figure 3.17: Radial profiles of deposition power density to electrons and ions at different injection energies.

The radial profiles for the simulation with $E_{\mathrm{NBI}} = 300$ keV show a larger deposition to both plasma ions and electrons near the plasma edge than the others simulation profiles. The neutral beam penetration for low NBI energies is lower. Again, this derives from the mean free path λ which characterizes the fast ions collisions: the lower the energy, the smaller the λ due to a direct proportionality to E_{NBI}. This can be also seen in the ionization clouds projections in (x,y) plane for $E_{\mathrm{NBI}} = 510$ keV and $E_{\mathrm{NBI}} = 300$ keV, shown in figures 3.18 and 3.19. The ionized particles with $E_{\mathrm{NBI}} = 510$ keV arrives deeper inside the plasma.

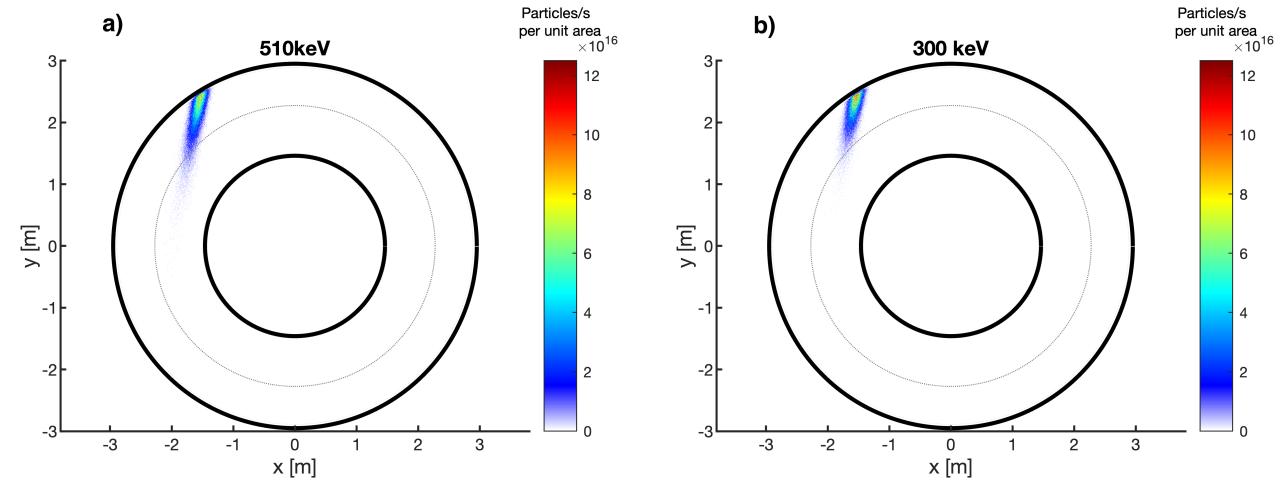

Figure 3.18: (x,y) projections of clouds of ionized particles derived from the neutral beam injection at 510 keV and 300 keV in the reference plasma scenario.

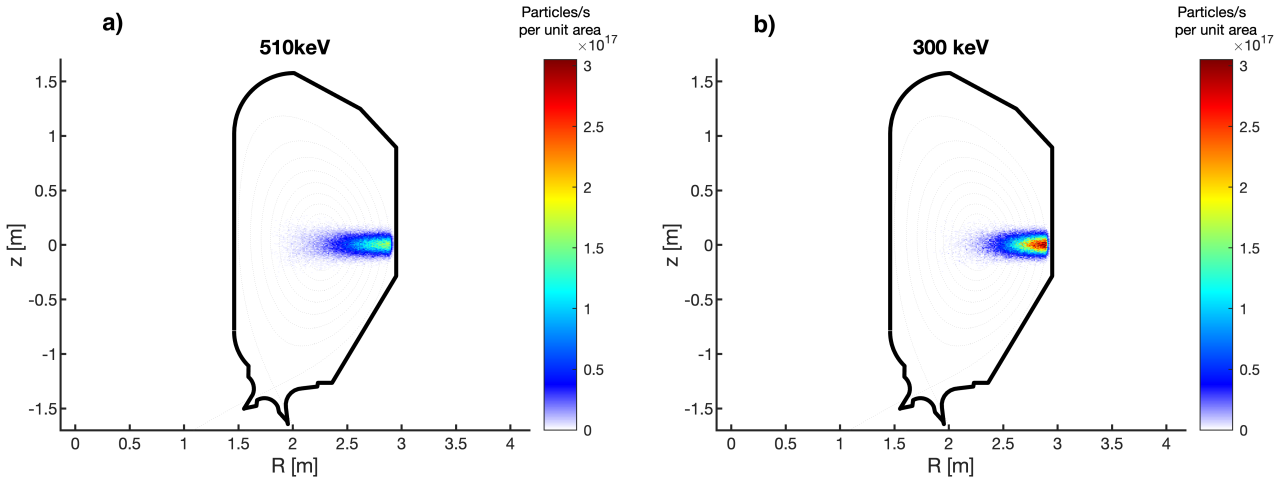

Figure 3.19: (R,z) projections of clouds of ionized particles derived from the neutral beam injection at 510 keV and 300 keV in the reference plasma scenario

Concerning the driven current, the radial profiles for the different energy scenarios are shown in figure 3.20. The relative values are instead reported in table 3.6. As for the radial profiles of the deposited power density, also for the driven current it is possible to observe clearly a dependence with the energy. In the CD efficiency η_{CD}, a logarithmic dependence on E_{NBI}/E_c justifies this increase, showing that larger E_{NBI} implies a larger injected current. As it can be seen in table 3.6, the injected current values don't change as in the cases of the plasma density and temperature scans, where the dependence from T_e, n_e was stronger. In this case indeed, the toroidal current passes from $I_{CD} = 1.55 \times 10^5$ A at $E_{\mathrm{NBI}} = 300$ keV to $I_{CD} = 2.26 \times 10^5$ A at $E_{\mathrm{NBI}} = 510$ keV, i.e. an increase of about $\sim 45\%$.

The relative velocity between ions and electrons, and therefore the current, increases when the torque is transferred preferentially to electrons. The injected torque is defined by two components, the j×B torque, derived from the radial movements of fast ions during their first orbit, and the collisional

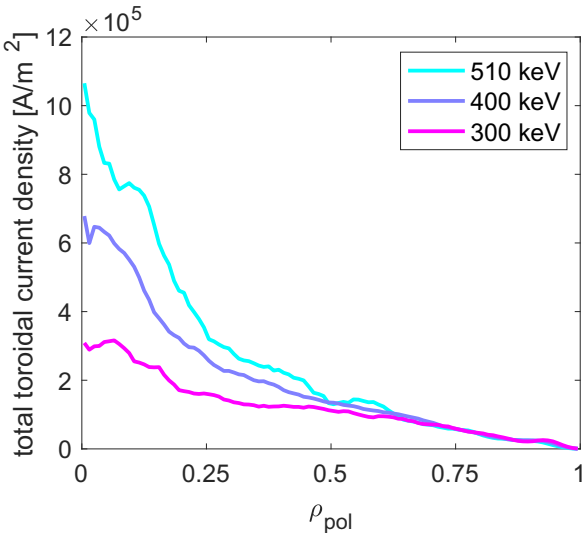

Figure 3.20: Power deposition and total toroidal current density at fixed temperatures but different densities.

torque. In particular, increasing E_{NBI} the collisional torque transferred to electrons increases, as can be seen in the distributions of collisional torques to plasma electrons and ions, respectively defined as $M_{col,e}, M_{col,i}$ reported in table 3.8. The total injected torque decreases from the scenario at 300 keV to that at 510 keV of about $\sim 24\%$.

Energy [keV]	$M_{col,e}$ [%]	$M_{col,i}$ [%]
300	32.24	67.76
400	35.13	64.87
510	**38.72**	**61.28**

Table 3.8: 0D collisional torque distribution to electrons and ions at different beam energies. In bold, the reference plasma scenario data.

To conclude, the critical energy for the analyzed scenarios is constant since doesn't depends on E_{NBI}. All the NBI energies are larger than the critical values along the radial coordinate. Analyzing instead the $2.5E_c$ radial profiles, the position at which $E_{\mathrm{NBI}} > 2.5E_c$ changes with the beam energy. For $E_{\mathrm{NBI}} = 300$ keV, power is mainly transferred to electrons in the plasma edge region, above $\rho_{pol} \sim 0.7$. Increasing the beam energy, the ρ_{pol} at which $E_{\mathrm{NBI}} > 2.5E_c$ is satisfied decreases. Both E_c and $2.5E_c$ radial profiles are depicted on figure 3.21 and 3.22.

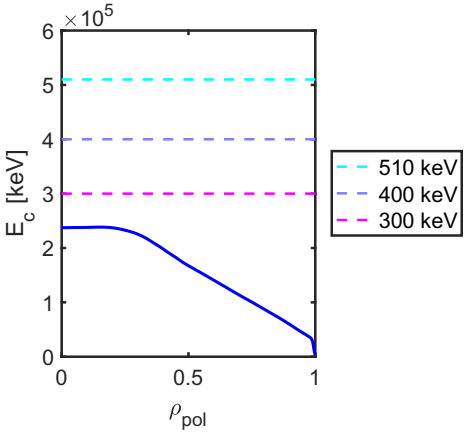

Figure 3.21: Radial profiles of the critical energy for different NBI energies.

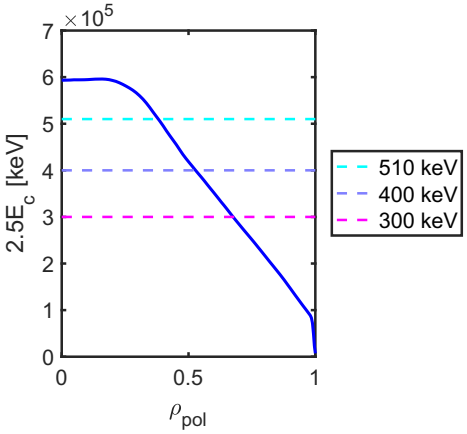

Figure 3.22: radial profiles of 2.5 times E_c for different NBI energies.

3.4 Concluding remarks

Numerical studies discussed in this chapter investigate beam-plasma interaction physics. Analyses are made changing plasma temperature and density independently to observe how their variations affect the beam-plasma interaction. For the NBI energy scan the injected power is kept fixed at 10 MW, even considering different NBI energies, to compare the results from beam-plasma interaction physics point of view. Some concluding remarks are reported here to summarize results obtained in this chapter.

Concerning the absorbed power from DTT NBI, significant changes are observed changing the plasma density profiles. To have an efficient absorption of about 100% of the injected power, the density must be sufficiently high ($> \ 0.5 \ n_e$) otherwise shine-through losses becomes significant in term of power losses ($\sim 7\%$ at 0.25 n_e) and also potentially harmful for the device. Low density plasma scenarios seem to be the most efficient way to drive the NBI current, since the injected current reaches ~ 1.4 MA, despite the lowest fraction of absorbed power detected (about 92%). Nevertheless, an optimization for both NBI CD efficiency and absorbed power is observed increasing the plasma temperatures or the NBI energy. Indeed, with an absorbed power of 99.92%, the NBI CD at 1.5 T_e is about 0.32 MA while that at 510 keV of injected energy in the plasma reference scenario is about 0.23 MA. To maximize the power deposition to electrons $P_{\mathrm{NBI,e}}$ it is possible to decrease the plasma temperature or increase the plasma density. In terms of the NBI energy, it is observed that, increasing E_{NBI}, also the fraction of deposited power to electrons increases. To maximize the fraction of deposited power to ions $P_{\mathrm{NBI,i}}$ instead opposite conditions must be considered. High plasma temperature and low plasma density determine an increase on the ion power distribution. The NBI energy instead must be decreased. The injection torque changes significantly only when the NBI energy changes. In particular, a decrease in the injection torque of about 24% is observed passing from 300 keV to 510 keV of NBI energy. No significant changes are observed in plasma density and temperature scans. First orbit losses are negligible thanks to the co-current injection. However, more details about them are given in the next chapter, where the EP orbit population for different DTT plasma scenarios and NBI energies are studied in a topological map designed in the CoM phase space, i.e the phase space defined by constants of motion and adiabatic invariant of the system.

Chapter 4

First topological analyses of energetic particle orbits in DTT with ASCOT code

The complexity of the EPs behavior inside plasmas is already clear from chapter 2. The focus of this chapter is to present a topological map for the classification of EP orbits in the phase space defined by EP constants of motion and adiabatic invariant of the system, as the toroidal canonical angular momentum P_ϕ, the energy E and the magnetic moment μ. Through this topological analysis a possible description of the expected EP confinement and losses is given. In particular, the EP orbit classification and the estimation of EP losses are performed. Topological maps are designed for different plasmas and different NBI energies for DTT, using the same scans analyzed in chapter 3, in the collisionless approximation to observe how different plasma temperatures and densities and different NBI energies change the EP behavior. Collisionless approach is assumed since first orbit losses, which are of particular interest for this analysis, occur on timescales that are smaller than the slowing down time (see section 2.2), i.e. the time required to released EP energy to plasma particles. Therefore, particles lost as first orbit losses would be lost also considering collisions between particles. However, collisions shift orbit points plotted on the EP topological map, e.g. some confined particles could be lost after collision. Moreover, due to the energy transfer between fast ions and plasma particles during Coulomb collisions, fast ions energy is reduced and EP topological maps changes, as explained in section 4.4.4.

As introduction to the chapter, in section 4.1, the adopted convention and the magnetic field equilibrium for the following analyses are defined. After that, in section 4.2, the topological map in the phase space (P_ϕ, μ, E), briefly called CoM (Constant of Motion) phase space, is built and its interpretation is illustrated in section 4.3. The topological map is drawn using equations which describes relevant EP orbits. These relevant orbits are referred to as orbit boundaries. The interpretation of the topological map is explained through figures with color coding to identify regions of the map in which particles behave differently. Moreover, an EP orbit "zoology" is presented in section 4.3.1, observing different particle orbits located in different domains of the topological maps. In section 4.4 results of ASCOT simulations performed for different scenarios in DTT are shown. In particular, the EP topological maps are populated by orbit points which identify the entire trajectory of EPs inside the plasma. The EP orbit population for plasma temperature and density scans are compared, together with those obtained for the NBI energy scan.

4.1 Adopted conventions

Adopted conventions used in this chapter are reported here. First of all, COordinate COnventionS (COCOS) [42] used here are introduced. Those of interest in this thesis are COCOS 2 and 5. Their relative index conventions are reported in table 4.1. The EQDSK file, generated by CREATE-NL free

boundary code [34], contains some of the plasma equilibrium information necessary for the construction of the topological maps discussed in this chapter. In particular, these information are the poloidal flux $\Psi(R, z)$, the free function g(R,z), the coordinates of the LCFS, the magnetic axis location (R_{ax}, z_{ax}) and the values of the poloidal flux and the toroidal magnetic field at the magnetic axis $\Psi_{ax}, B_{\phi,ax}$. All these quantities will be better explained in sections 4.1.1 and 4.1.2. COCOS 5 is adopted in ASCOT simulations and will be the adopted convention also for this thesis.

COCOS	e_{Bp}	σ_{Bp}	$\sigma_{\mathrm{R}\phi\mathrm{z}}$	$\sigma_{\rho\theta\phi}$	ϕ from top	θ from front
2	0	+1	(R,z,ϕ), -1	(ρ, θ, ϕ), +1	clockwise	cnt-clockwise
5	0	+1	(R,ϕ,z), +1	(ρ, ϕ, θ), -1	cnt-clockwise	cnt-clockwise

Table 4.1: Coordinate conventions [42] for COCOS 2 and 5. $e_{Bp} = 0$ means that ψ is divided by 2π. Therefore the poloidal flux surface is defined by Ψ. σ_{B_p} factor defines if the poloidal flux Ψ increases (+1) or decreases (-1) with the normalized poloidal flux coordinate ρ_{pol}. Signs of the cylindrical and poloidal coordinates, respectively defined as $\sigma_{\mathrm{R}\phi\mathrm{z}}$ and $\sigma_{\rho\theta\phi}$, indicate the right-handed (+1) and left-handed (-1) definition. ϕ and θ define respectively the toroidal and poloidal angle where *clockwise* and *cnt-clockwise* indicate the direction of rotation for these coordinates.

4.1.1 Coordinate systems

As can be already seen in table 4.1, different coordinate systems can be used in tokamak plasmas: cylindrical coordinates, toroidal coordinates or flux coordinates. In the following, a brief description of all these coordinate systems is given. All coordinate references can be better understand in figure 4.1.

- $(\mathrm{R}, \phi, \mathrm{z})$ are defined as cylindrical coordinates, where R and z describe the radial and vertical positions and ϕ the toroidal direction;
- $(\mathrm{r}, \phi, \theta)$ are instead toroidal coordinates, where r is the radial position inside the torus, ϕ and θ are respectively the toroidal and poloidal angles;
- $(\psi_{pol}, \phi, \theta)$ represents the flux coordinates, with ψ_{pol} the poloidal flux contained within a contour outlined by constant pressure values and ϕ and θ are the toroidal and poloidal angles as before. ψ_{pol} corresponds to the poloidal magnetic field flux across a surface at fixed θ. A similar definition can be given for the toroidal flux, as the toroidal magnetic field flux across a surface at fixed ϕ. The poloidal flux function can be also written as $\psi_{pol} = 2\pi\Psi_{pol}$, where Ψ_{pol} is called stream function. Ψ_{pol} can be seen as poloidal flux per radiant. In the next, Ψ_{pol} is used for the flux surface identification, in agreement with COCOS 5 ($e_{B_p} = 0$). Moreover, a normalized poloidal flux coordinates, called ρ_{pol}, can be defined as in (4.6). Flux coordinates then can be also written as $(\rho_{pol}, \phi, \theta)$.

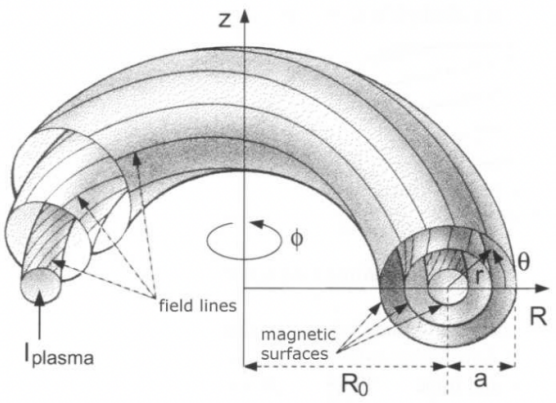

Figure 4.1: Representation of different coordinate systems. The magnetic fields surfaces are labelled by Ψ_{pol} (or ρ_{pol} in the normalized convention) [43].

Referring to the poloidal flux coordinate system $(\Psi_{pol}, \phi, \theta)$, it is possible to distinguish some relevant flux surfaces, and their relative corresponding cylindrical coordinates $(\mathrm{R}, \phi, \mathrm{Z})$, useful in the definition of the topological map described in section 4.2.

Magnetic Axis (MA) For a generic toroidal angle ϕ, the magnetic axis is defined in flux coordinate terms by $(\Psi_{ax}, \phi, 0)$. In the cylindrical reference instead corresponds to (R_{ax}, z_{ax}) at fixed ϕ. The position of MA does not usually match with the geometrical axis of the machine, defined by (R_0, z_0) coordinate. Indeed this is the case of the DTT equilibrium considered in this analysis, where $(R_{ax}, z_{ax}) \sim (2.28\ \mathrm{m}, 0.02\ \mathrm{m})$ while the geometrical axis is $(R_0, Z_0) \sim (2.19\ \mathrm{m}, 0\ \mathrm{m})$. This displacement is also known as Shafranov shift.

Last Closed Flux Surface (LCFS) The LCFS corresponds to the last flux surface with closed magnetic field lines. The poloidal flux associated to the LCFS is called Ψ_a. Due to the surjective nature of the stream function Ψ_{pol} along the radial position R (see figure 4.5), it is possible to identify two different coordinates at fixed ϕ, where the stream functions have the same value. For the LCFS at z_{ax}, in the flux surface coordinate system, these points are $(\Psi_a, \phi, 0)$ and (Ψ_a, ϕ, π). The first one corresponds to the outer edge of the LCFS, while the second to the inner edge. Switching to the cylindrical coordinate system, always at z_{ax} and fixed ϕ, these two points corresponds respectively to the maximal R_M and minimal R_m radial position. Since the magnetic field B scales as 1/R, these edges are respectively called Low Field Side (LFS) and High Field Side (HFS).

From now on, R_Ψ represents the radial coordinate for a given Ψ_{pol} at a fixed z. Through the poloidal flux of the magnetic axis and the LCFS (respectively Ψ_{ax}, Ψ_a), the poloidal flux coordinate can be normalized, obtaining ρ_{pol} coordinate as defined in (2.18). In figure 4.2 the LCFS, the MA position, the LFS and HFS coordinates for the plasma reference scenario of DTT (see section 2.1.1) are represented, together with its first wall geometry. These points are relevant for next discussions.

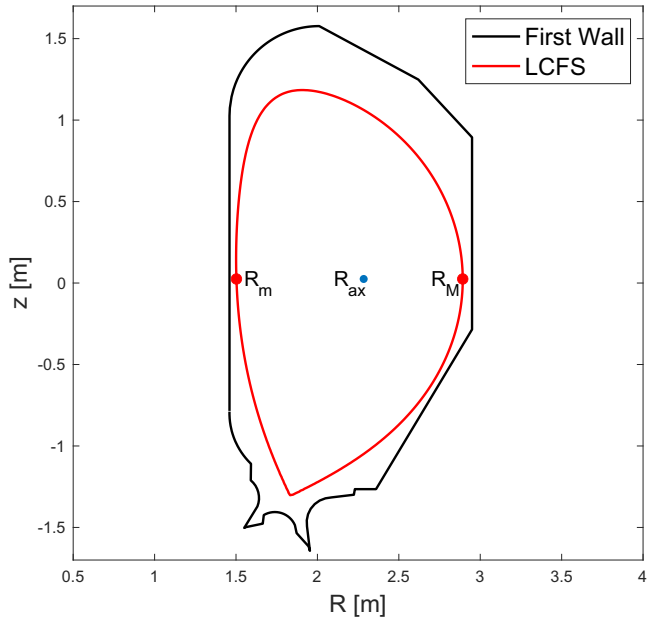

Figure 4.2: First wall and last closed flux surface (LCFS) of DTT for the plasma reference scenario. The positions of R_{ax}, R_m, R_M at z_{ax} are reported too.

4.1.2 Magnetic field equilibrium

The magnetic field for an axisymmetric system can be obtained from the stream function $\Psi(R, z)$ and the free function $g(R, z) = RB_\phi(R, z)$, called also current flux function. In COCOS 5, the magnetic

field is obtained from the following equations

$$B_{\theta,R}(R,z) = \frac{1}{R}\frac{\partial \Psi(R,z)}{\partial z} \tag{4.1}$$

$$B_{\theta,z}(R,z) = -\frac{1}{R}\frac{\partial \Psi(R,z)}{\partial R} \tag{4.2}$$

$$B_{\phi}(R,z) = \frac{1}{R} g(R,z) \tag{4.3}$$

The main component of the magnetic field in tokamaks is given by the toroidal B_ϕ which, as can be seen in equation (4.3), scales as 1/R. The poloidal component of the magnetic field is instead defined by $\vec{B}_p = B_{\theta,R}\hat{e}_R + B_{\theta,z}\hat{e}_z$. The magnetic field used as input in ASCOT simulations is obtained using $\Psi(R,z)$ and $g(R,z) = RB_\phi(R,z)$ functions stored in the EQDSK. Figures 4.3 and 4.4 show the magnetic field components of DTT used for the analyses presented later.

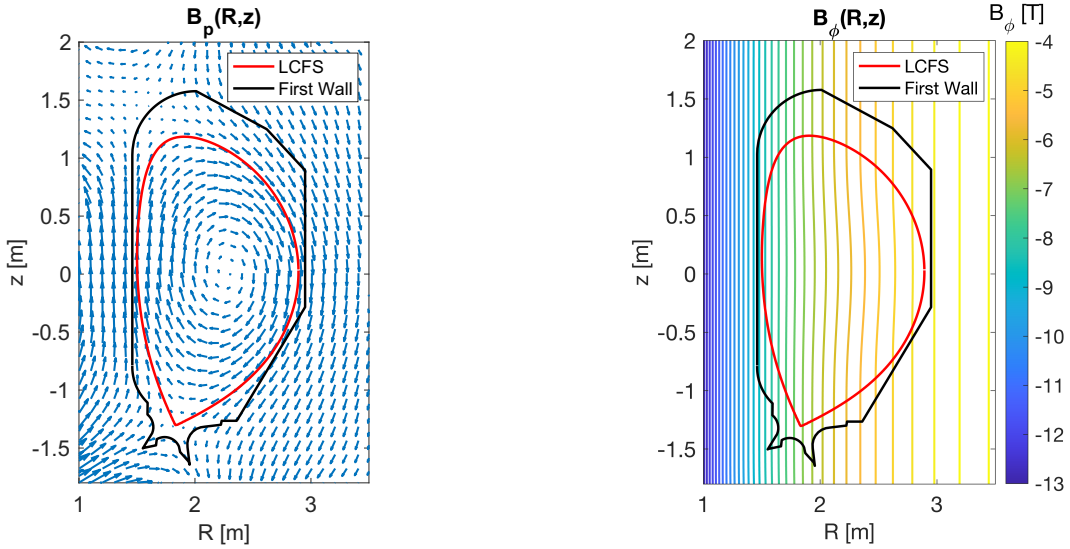

Figure 4.3: DTT poloidal and toroidal magnetic fields $B_p(R,z)$, $B_\phi(R,z)$ in COCOS 5.

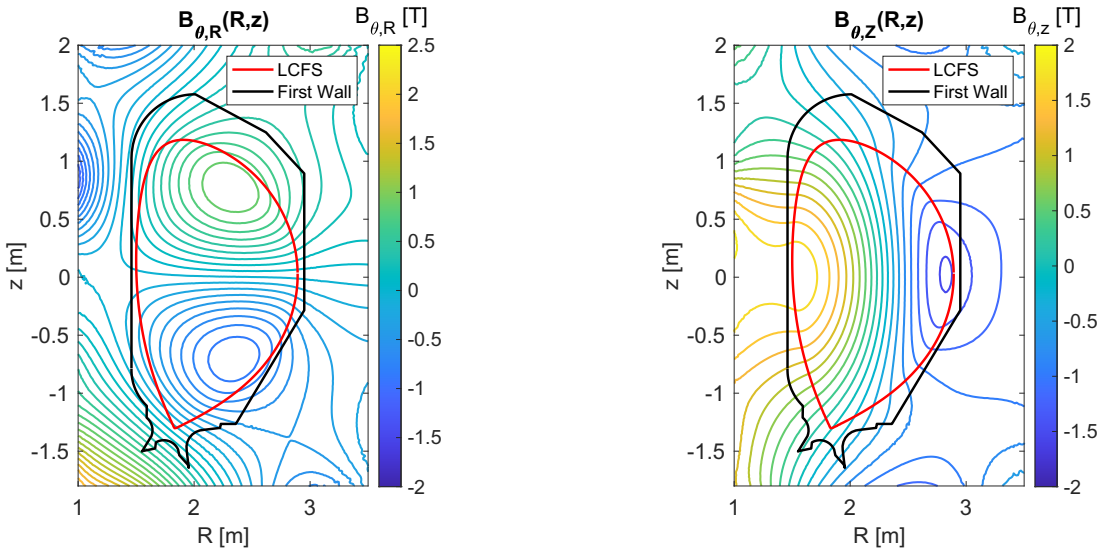

Figure 4.4: DTT poloidal magnetic field components $B_{\theta,R}(R,z)$, $B_{\theta,z}(R,z)$ in COCOS 5.

As it can be seen from figure 4.3, the poloidal magnetic field B_p follows the clockwise direction. This implies that the plasma current I_p flows inward with respect to the (R,z) plane. The toroidal magnetic

field B_ϕ instead is directed outward, therefore in the opposite direction with respect to I_p. This must be taken into account for the topological map interpretation. According to the relative signs of I_p and B_ϕ, EP orbits are confined or lost in different regions of the topological map, as later discussed in section 4.2.6. From the toroidal magnetic field representation, the plasma diamagnetism can be observed in the small deformation of the toroidal field lines inside the LCFS. Plasma response to an applied magnetic field is indeed aimed to reduce the applied field. The radial profiles of $B_\phi(R)$ at z_{ax}, as those of $\Psi(R)$ and $g(R)$ are shown in figure 4.5. z_{ax} represents the vertical coordinate of interest for the topological map representations since the NBI studied in this thesis in DTT is equatorial.

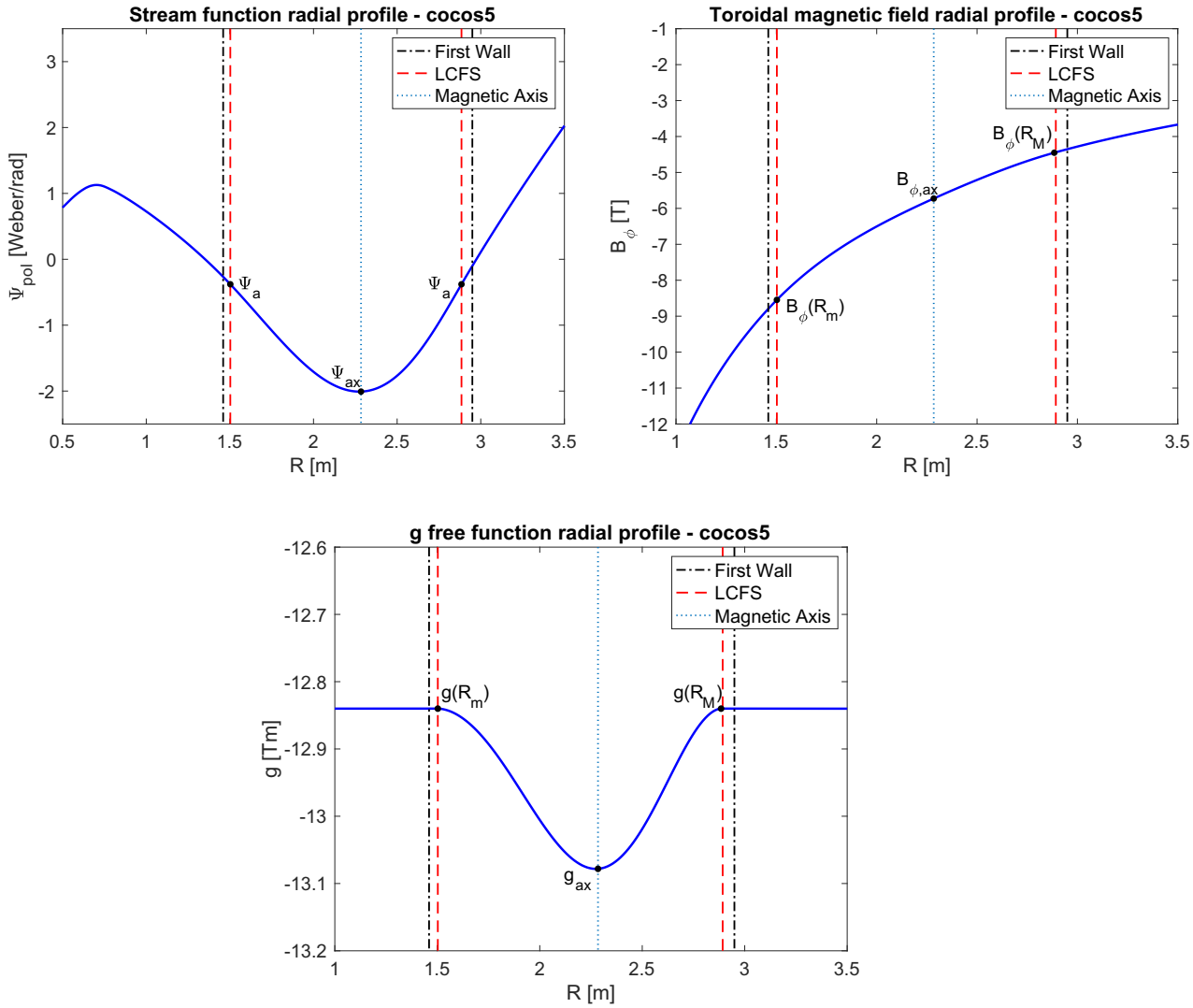

Figure 4.5: Radial profiles of $\Psi(R)$, $B_\phi(R)$, g(R) at z_{ax} for the magnetic equilibrium configuration of DTT in the plasma reference scenario, according to COCOS 5.

$B_\phi(R_M)$ and $B_\phi(R_m)$ in figure 4.5 refer respectively to the toroidal magnetic fields at the LFS and HFS of the machine. The same is valid for g(R) function. For a general radial position R_Ψ the toroidal magnetic field is $B_\phi(R_\Psi)$. The stream function profile shows that Ψ_{pol} is a surjective function, which becomes injective in two radial intervals defined by $[R_m, R_{ax}]$ and $[R_{ax}, R_M]$. It is worth noting that the curved shape of the g(R) profile derives from the plasma diamagnetism, whose effect is visible in the toroidal magnetic field (figure 4.3). The difference from $g(R_{ax})$ and $g(R_m) \sim g(R_M)$ is around 0.2 Tm. These radial profiles are useful for the computation of the toroidal canonical angular momentum P_ϕ and the magnetic moment μ necessary to the construction of the topological map for the EP orbits in the phase space (P_ϕ, μ) at constant E. The equations for P_ϕ and μ, which defines the topological map, are described in the next section, where the CoM phase space is introduced.

4.2 Constant of Motion (CoM) phase space

In section 2.3.1, the equation of motion for particles moving inside the plasma was presented. This equation can be solved in terms of spatial and velocity coordinates. However, a complete description of particle orbits can also be obtained by solving the equation with a reduced number of coordinates, exploiting the EP constants of motion and adiabatic invariant. In a collisionless approach for the axisymmetric plasma these coordinates are the kinetic energy E, the canonical toroidal angular momentum P_ϕ and the magnetic moment μ. The magnetic moment is an adiabatic invariant, being approximately constant over time scales typical of the particle motion if the spatial variations of the magnetic field are negligible compared to the EP gyro-motion [44]. Since in the cases studied, the magnetic field does vary along the particle trajectory, the constancy approximation of μ is verified in section 4.4.1. Using E, P_ϕ and μ, the number of coordinates necessary for orbit descriptions is reduced from six to three. This solution turns out to be useful to describe the fast ion orbit topology in a phase space defined by (P_ϕ, μ) at constant E. In this phase space a point represents an entire EP trajectory if P_ϕ, μ and E are exactly preserved during the particle motion [44]. Points in the CoM phase space are distributed in a topological map defined by so-called orbit boundaries, i.e. particular curves related to positions at the equatorial plane in our case of study. Depending on position in the CoM phase space, particles can be identified as lost or with different orbit typologies. Lost particles could be harmful for the device and must be avoided. The collisionless approach is justified for the study of particle losses since particles identified as lost would be lost also considering collisions. The time required by an EP to complete a toroidal turn is about $\tau_{tor} \sim 1.97 \times 10^{-6}$ s, smaller than the DTT slowing down time $\tau_s \sim 0.13$ s. Orbit boundaries are defined by equations which describe the canonical toroidal magnetic moment P_ϕ as a function of the magnetic moment μ for different radial position at fixed energy E and vertical position z_{ax}. P_ϕ and μ are computed using the radial profiles of $\Psi(R)$, $B_\phi(R)$, g(R) at z_{ax}. The orbit boundary equations will be presented in the following section. For this work, the energy considered to plot the orbit boundaries is $E = 510$ keV, i.e DTT NBI energy. This situation corresponds to newly-born beam fast ions. The CoM phase space indeed depends on the particle energy: this can be better seen in section 4.4 where different topological maps are built for different NBI energies.

4.2.1 Orbit boundary equations: general description

The toroidal canonical angular momentum and the magnetic moment are defined respectively as $P_\phi = q\Psi + mRv_\parallel$, with $v_\parallel$ as approximation of the toroidal velocity [25], and $\mu = \frac{mv_\perp^2}{2B_{tot}}$, as already reported in chapter 2. The orbit boundaries are defined from the relation that connects the toroidal canonical angular momentum to the magnetic moment. This relation is obtained defining P_ϕ and μ in terms of λ, the particle pitch, and then substituting μ in P_ϕ. The velocity and energy components in terms of λ are defined as follows

$$v_\perp = \sqrt{(1-\lambda^2)}v \qquad v_\parallel = \lambda v$$

$$E_\perp = \frac{1}{2}mv_\perp^2 = (1-\lambda^2)E \qquad E_\parallel = \frac{1}{2}mv_\parallel^2 = \lambda^2 E$$

The substitution of these velocities and energies into P_ϕ and μ provides the following parametrization in terms of Ψ, λ, E[1]:

$$\begin{cases} P_\phi(\Psi,\lambda,E) = q\Psi + \lambda\frac{g(R_\Psi)}{B_\phi(R_\Psi)}\sqrt{2mE} \\ \mu(\Psi,\lambda,E) = (1-\lambda^2)\frac{E}{B_{tot}(R_\Psi)} \end{cases} \tag{4.4}$$

The pitch dependence of (4.4) is cancelled writing λ^2 in terms of μ and substituting it in the equation of P_ϕ. The final result is

$$P_\phi^\pm(\Psi,\mu,E) = q\Psi \pm \frac{g(R_\Psi)}{B_\phi(R_\Psi)}\sqrt{2m\left[E - \mu B_{tot}(R_\Psi)\right]} \tag{4.5}$$

[1] for simplicity of notation, from now on $\Psi_{pol} = \Psi$

where $\pm$ derives from the sign of λ, positive for *co-moving particles* and negative for *counter-moving particles* with respect to $\vec{B}$. Equation 4.5 describes different parabolas in the CoM phase space when R_Ψ, μ are changed. It is worth noting that, the right-side of each parabola is obtained by P_ϕ^+, while the left-side is obtained by P_ϕ^-. To plot orbit boundaries, it is possible to use the equation 4.5 or its parametrized form, defined by equations (4.4). The orbit boundaries of interest are listed below:

- The high field side (HFS) curve, at the radial position $R_\Psi = R_m$;
- The low field side (LFS) curve, at $R_\Psi = R_M$;
- The magnetic axis (MA) curve, at $R_\Psi = R_{ax}$;
- The trapped-passing boundary, which describes the boundary curve used to distinguish CoM phase space area of passing and trapped particles. Since a trapped particle is defined by $v_\parallel = 0$ at certain point of its orbit the trapped-passing boundary is built imposing $\lambda = 0$ and computing P_ϕ for all the possible radial positions.
- The stagnation boundary instead defines the curves which contains stagnation orbits. It is obtained computing the maximum values of P_ϕ for fixed values of the magnetic moment μ.

4.2.2 CoM phase space in normalized coordinates

The CoM phase space can be defined also in normalized coordinates for the toroidal canonical angular momentum and the magnetic moment. The dimensionless versions of these quantities are obtained as follow:

$$\Pi(\Psi, \lambda, E) = \frac{P_\phi}{q\Psi_a} \qquad \Lambda(\Psi, \lambda, E) = \mu \frac{B_{tot,ax}}{E} \tag{4.6}$$

where $B_{tot,ax}$ is the total magnetic field on axis [44]. Equation (4.5) in normalized coordinates becomes

$$\Pi_\phi^\pm(\Psi, \Lambda, E) = \frac{\Psi}{\Psi_a} \pm \frac{g(R_\Psi)}{q\Psi_a B_\phi(R_\Psi)} \sqrt{2mE\left[1 - \Lambda \frac{B_{tot}(R_\Psi)}{B_{tot,ax}}\right]} \tag{4.7}$$

In COCOS 5, adopted for this thesis, since $\Psi < 0$ in the interval $[R_m, R_M]$, as well as $g(R_\Psi) < 0$, $B_\phi(R_\Psi) < 0$, the dimensionless toroidal canonical angular momentum Π_ϕ^+, related to co-moving particles ($\lambda > 0$), and Π_ϕ^-, related to counter-moving particles ($\lambda < 0$), design respectively the left-side and right-side of parabolas. Of course this is true considering positive particles as ions. In the following, the description of the boundary curves is discussed in details in terms of Π_ϕ, Λ coordinates. Figure 4.6 shows the orbit boundaries defined above in the normalized CoM phase space, according to [26]. A similar graph is built later on for DTT.

4.2.3 Passing particle boundaries

The HFS, LFS and MA curves are the relevant passing particle boundaries. Indeed, when a particle cross the inner or outer plasma edge in a collisionless scenario, it becomes a lost particle. The intersection or not with the magnetic axis define instead potato and stagnation orbits, particular cases of trapped and passing EP orbits (see section 2.3.3 for potato and stagnation orbit descriptions). In table 4.2 the conditions that must be imposed to (4.7) to obtain the following parabolic curves are reported.

$$\Pi_\phi(R_m) = 1 \pm \frac{g(R_m)}{q\Psi_a B_\phi(R_m)} \sqrt{2mE\left[1 - \Lambda \frac{B_{tot}(R_m)}{B_{tot,ax}}\right]} \tag{4.8}$$

$$\Pi_\phi(R_M) = 1 \pm \frac{g(R_M)}{q\Psi_a B_\phi(R_M)} \sqrt{2mE\left[1 - \Lambda \frac{B_{tot}(R_M)}{B_{tot,ax}}\right]} \tag{4.9}$$

$$\Pi_\phi(R_{ax}) = \frac{\Psi_{ax}}{\Psi_a} \pm \frac{g(R_{ax})}{q\Psi_a B_\phi(R_{ax})} \sqrt{2mE\left[1 - \Lambda\right]} \tag{4.10}$$

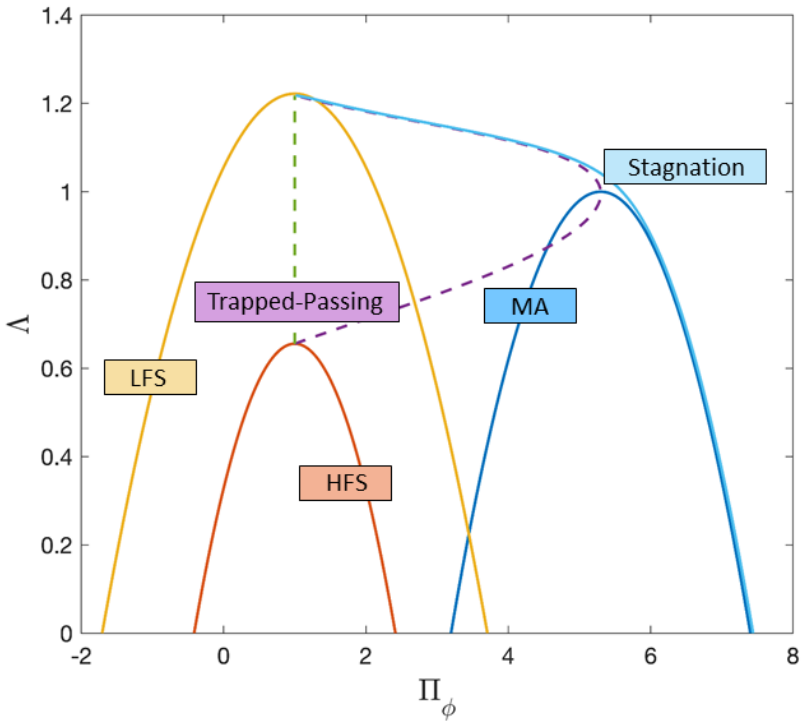

Figure 4.6: Orbit boundary representations in the normalized plane for fixed high energy E = 3 MeV.

Boundary	Radial position	Flux coordinates
HFS	R_m	(Ψ_a, ϕ, π)
LFS	R_M	$(\Psi_a, \phi, 0)$
MA	R_{ax}	$(\Psi_{ax}, \phi, 0)$

Table 4.2: Radial positions and flux coordinates for HFS, LFS and MA boundary curves.

Curves defined by (4.8)-(4.10) are drawn in figure 4.7 for DTT device and plasma reference scenario.

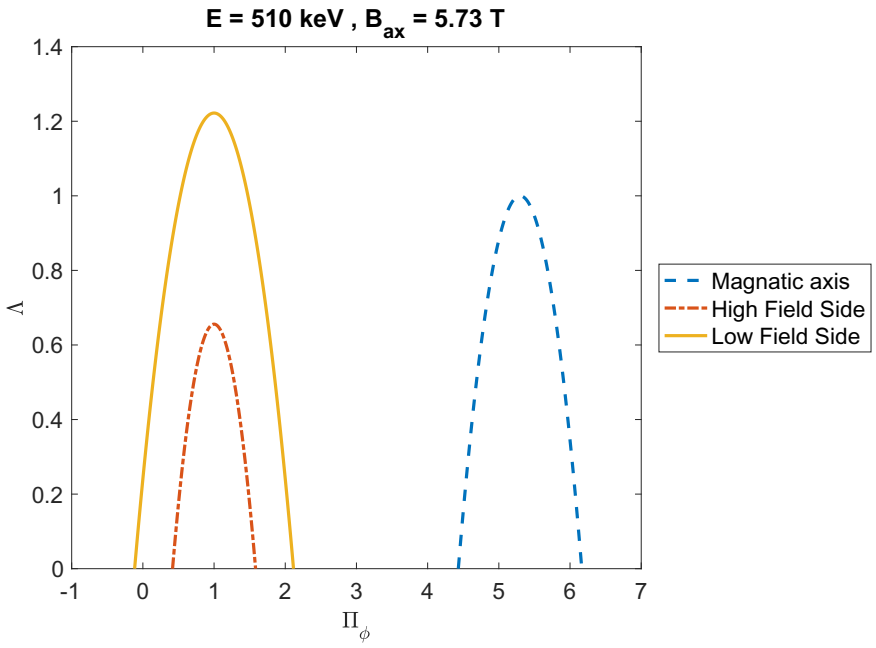

Figure 4.7: Passing orbit boundaries at $E = 510$ keV.

A particle follows undoubtedly a passing orbit if its pitch is $\lambda = \pm 1$. This condition is reflected on Λ as $\Lambda = 0$. Imposing $\Lambda = 0$ in (4.8)-(4.10), six different points in the phase space (Π_ϕ, Λ) can be distinguished. These points represent passing particle orbits. Their coordinates are the following:

$$\left(\Pi_\phi^{\pm}(R_m),\ \Lambda(R_m)\right) = \left(1 \pm \frac{g(R_m)}{q\Psi_a B_\phi(R_m)}\sqrt{2mE},\ 0\right) \tag{4.11}$$

$$\left(\Pi_\phi^{\pm}(R_M),\ \Lambda(R_M)\right) = \left(1 \pm \frac{g(R_M)}{q\Psi_a B_\phi(R_M)}\sqrt{2mE},\ 0\right) \tag{4.12}$$

$$\left(\Pi_\phi^{\pm}(R_{ax}),\ \Lambda(R_{ax})\right) = \left(\frac{\Psi_{ax}}{\Psi_a} \pm \frac{g(R_{ax})}{q\Psi_a B_\phi(R_{ax})}\sqrt{2mE},\ 0\right) \tag{4.13}$$

Points defined by (4.11) represent HFS passing orbits, those defined by (4.12) represent LFS passing orbits. The points in (4.13) instead define MA passing orbits. It is possible to define some relations between these points. Since $g(R_m) \sim g(R_M)$, $|B_\phi(R_m)| > |B_\phi(R_M)|$ and $\Psi_a < 0$, the normalized toroidal canonical angular momenta are related as

$$\Pi_\phi^+(R_M) < \Pi_\phi^+(R_m) \qquad\qquad \Pi_\phi^-(R_M) > \Pi_\phi^-(R_m) \tag{4.14}$$

Exploiting equation (4.7), it is possible to draw in the CoM phase space different parabolas changing the value of the radial position R. These new parabolas are located among passing orbit boundaries draw by equations (4.8)-(4.10). In figure 4.8, some parabolas are designed for different $R \in [R_m, R_{ax}]$ and $R \in [R_{ax}, R_M]$. Radial positions in the former interval are defined by parabolas between the HFS and MA curves while radial positions in the latter interval are defined by parabolas between MA and LFS boundaries. Moreover, in figure 4.8, the sides of parabolas corresponding to $\Pi_\phi^+(R)$ and $\Pi_\phi^-(R)$ solutions are indicated respectively with dashed and solid line which in practice corresponds to different pitch signs. For the simulations performed in this thesis, the interest is on the solid-side of the parabolas since EPs are counter-moving particles with respect to $\vec{B}$ ($\lambda < 0$).

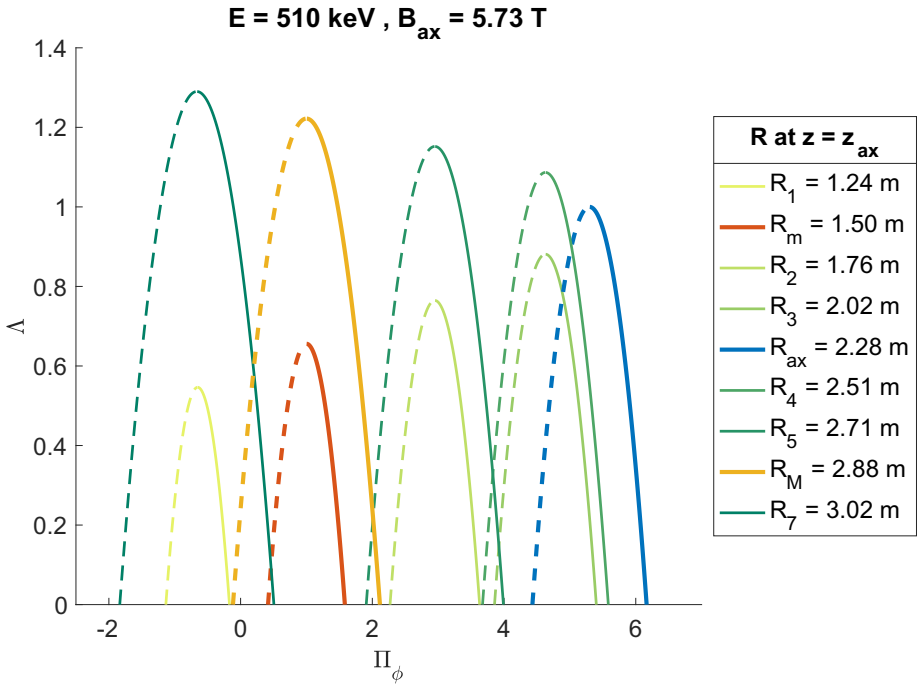

Figure 4.8: Passing orbit boundaries and parabolas at different radial positions R_i. The solid lines correspond to $\Pi_\phi^-(R)$ solutions ($\lambda < 0$), while dashed lines correspond to $\Pi_\phi^+(R)$ solutions ($\lambda > 0$).

4.2.4 Trapped-passing boundary

As described previously, trapped particle orbits are limited by two curves: the trapped-passing boundary and the stagnation boundary. The first one defines the condition at which a passing particle

becomes trapped. This happens when $\lambda = 0$, which implies a critical value for the magnetic moment, $\mu_c = \frac{E}{B_{tot}}$. Particles with a magnetic moment larger that μ_c are trapped [27]. Exploiting this condition, the boundary between trapped and passing particle orbits is defined by the following curve, parametrized with respect to the radial position R_Ψ

$$(\Pi_\phi(R_\Psi), \Lambda(R_\Psi)) = \left(\frac{\Psi}{\Psi_a}, \frac{B_{tot,ax}}{B_{tot}(R_\Psi)} \right) \tag{4.15}$$

Differently from the case of passing boundary orbits, to plot this curves the radial position is kept free while the pitch value is fixed at 0. The result is shown in figure 4.9. The green line represents the situation in which banana tips contact the last closed flux surface. Therefore, the green line can be interpreted as the left-boundary of trapped particle domains [26], called trapped boundary.

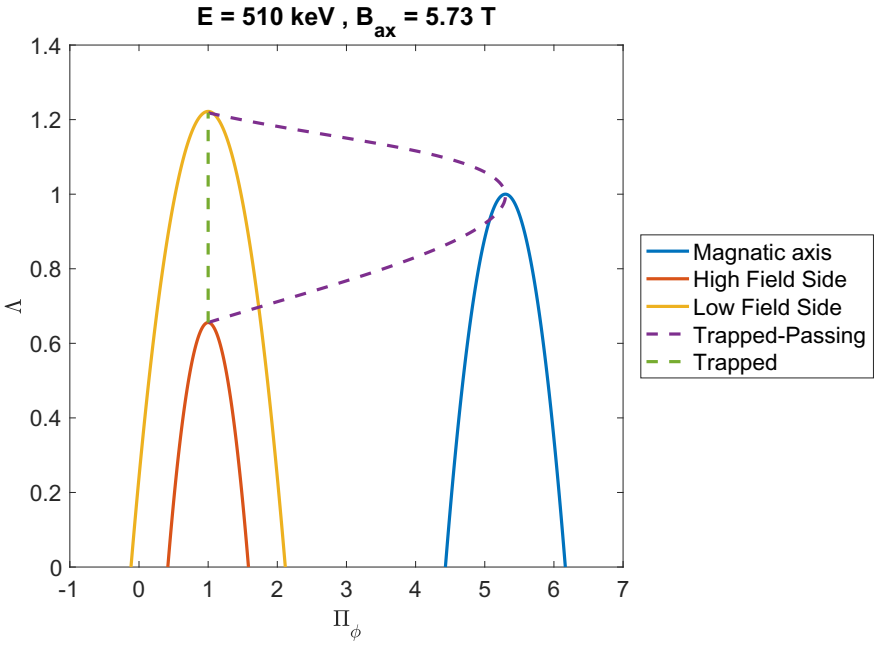

Figure 4.9: Plot of the trapped-passing orbit boundary together with the passing orbit boundaries at $E = 510$ keV.

Some particular orbits of trapped particles can be defined as for passing particles at R_m, R_{ax}, R_M. Their points are defined below:

$$(\Pi_\phi(R_m), \Lambda(R_m)) = \left(1, \frac{B_{ax}}{B_{tot}(R_m)} \right) \tag{4.16}$$

$$(\Pi_\phi(R_M), \Lambda(R_M)) = \left(1, \frac{B_{ax}}{B_{tot}(R_M)} \right) \tag{4.17}$$

$$(\Pi_\phi(R_{ax}), \Lambda(R_{ax})) = \left(\frac{\Psi_{ax}}{\Psi_a}, 1 \right) \tag{4.18}$$

(4.16) and (4.17) defines respectively HFS and LFS trapped orbits while (4.18) defines a MA trapped orbit. An interesting relation can be now derived for the magnetic moment of these points:

$$\Lambda(R_m) < \Lambda(R_{ax}) < \Lambda(R_M) \tag{4.19}$$

It is worth noting that all points in (4.16)-(4.18) correspond to the vertices of the parabolas which describe the passing orbit boundaries. Also the vertices of the parabolas defined at radial positions different from R_m, R_{ax}, R_M corresponds to trapped particle orbits. This can be better seen in figure 4.10, where the blue line describes the trapped-passing boundary while passing curves at different radial positions are in grey. As it can be noticed in figure 4.9, the intersection between the trapped-passing boundary and the magnetic axis parabola determines a small region. Here potato orbits live (see section 2.3.3 for potato orbit description). More details will be provided in section 4.3, where a guideline for the interpretation of the topological map is given.

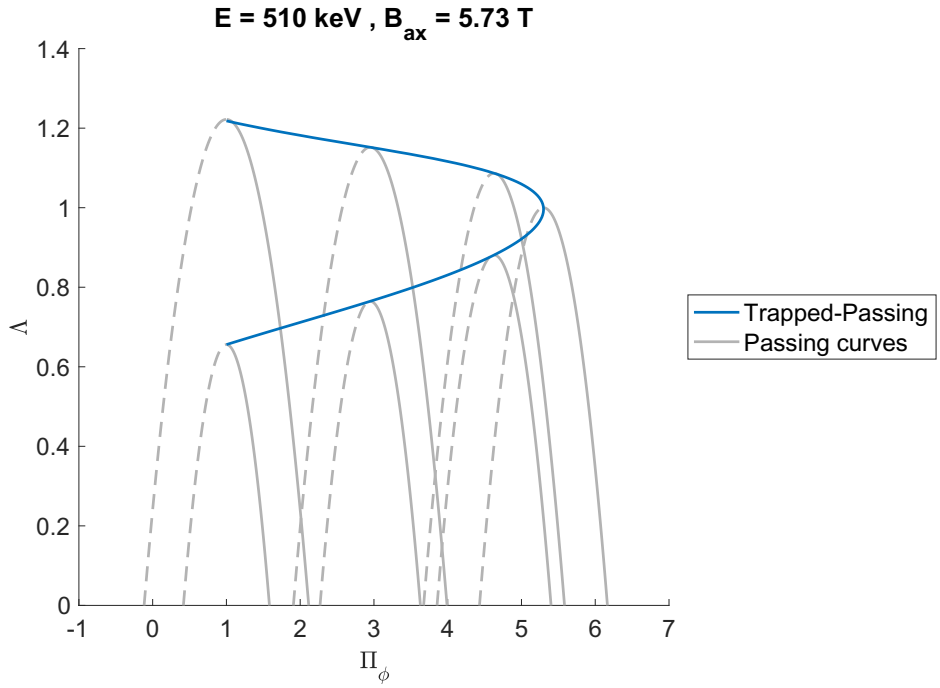

Figure 4.10: Passing orbit boundaries and parabolas at different radial position R_i with trapped-passing boundary in blue. The solid lines corresponds to $\Pi_\phi^-(R)$ solutions ($\lambda < 0$), while dashed lines corresponds to $\Pi_\phi^+(R)$ solutions ($\lambda > 0$).

4.2.5 Stagnation orbit boundary

The stagnation boundary defines the curve which encloses stagnation orbits (see section 2.3.3 for orbit description). These curves are obtained as described in [26] computing the maximum toroidal canonical angular momentum for a given value of the magnetic moment, defined in terms of λ and Ψ. The normalized magnetic moment $\Lambda = \Lambda(\Psi_k, \lambda_k)$ is represented as a function of the stream function Ψ_k and the particle pitch λ_k, as can be seen in figure 4.11.

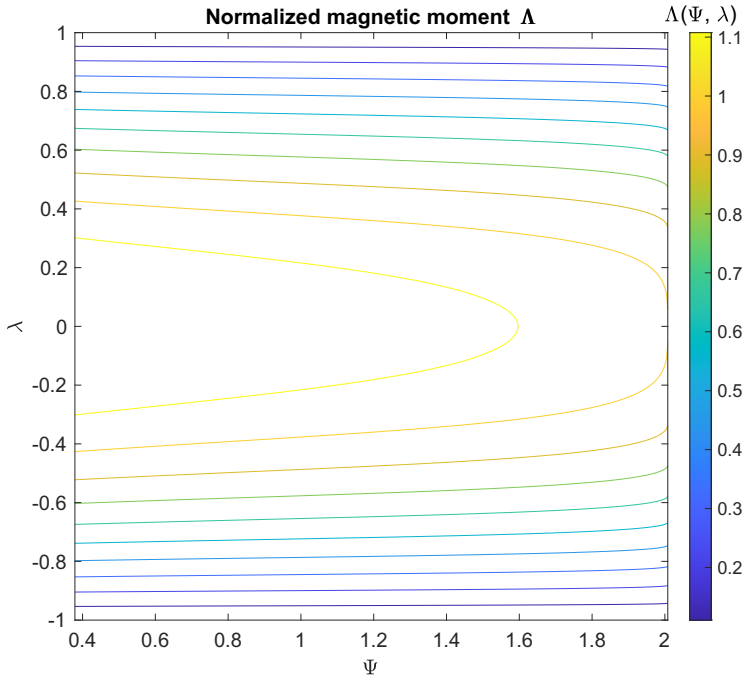

Figure 4.11: Normalized magnetic moment Λ as a function of Ψ and λ at $E = 510$ keV.

For each $\Lambda(\lambda_k, \Psi_k)$, the normalized toroidal canonical angular momentum $\Pi_{\phi,k}$ is computed by equation (4.20) for every (λ_k, Ψ_k), coupled that gives a constant value of Λ. Considering only the maximum $\Pi_{\phi,k}$ for each Λ, the stagnation boundary is determined. This curve is shown in figure 4.12 together with the trapped and passing particle orbit boundaries.

$$\Pi_{\phi,k,max}(\lambda_k, \Psi_k) = max\left(\frac{\Psi_k}{\Psi_a} + \lambda_k \frac{g(R_{\Psi_k})}{q\Psi_a B_\phi(R_{\Psi_k})}\sqrt{2mE}\right) \tag{4.20}$$

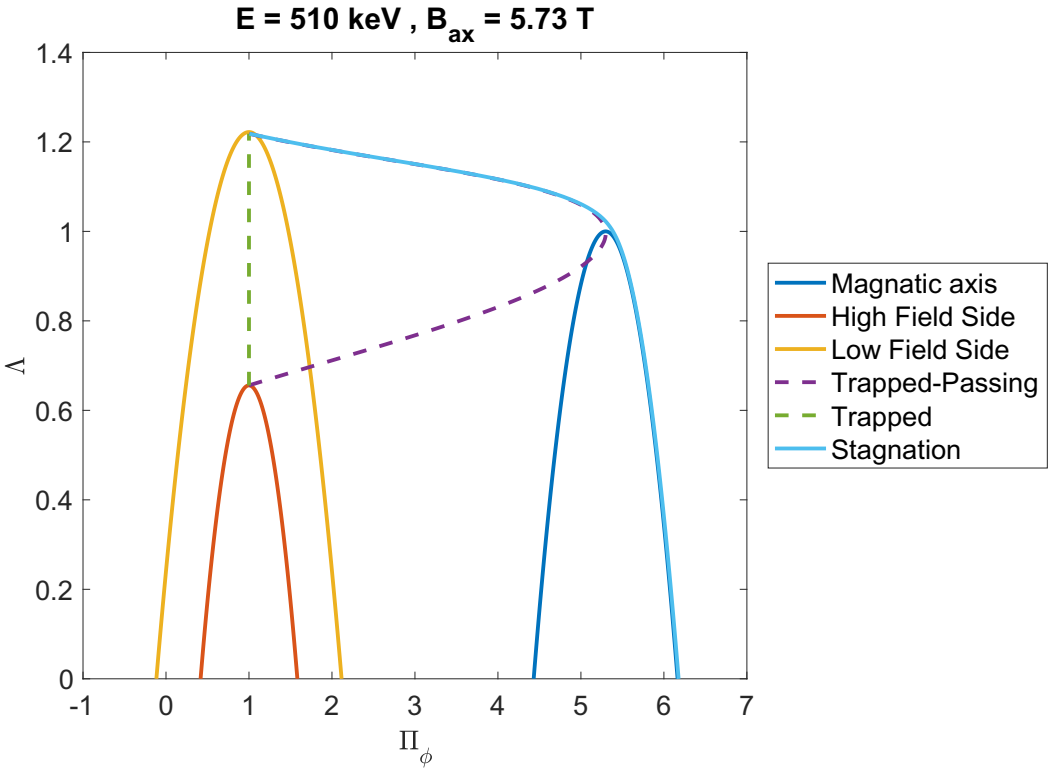

Figure 4.12: Plot of the stagnation orbit together with the trapped and passing particle orbit boundaries at $E = 510$ keV. This plot corresponds to the complete orbit boundary structure in the CoM phase space in normalized coordinates for the DTT plasma reference scenario at energy E = 510 keV.

4.2.6 Confined and lost particles in CoM phase space

Particles can be confined inside the plasma or lost outside. This last situation, in a collisionless approximation, happens when particle trajectories cross the inner or outer plasma edges. Different kind of particle losses were explained in section 2.2.4. In this chapter, the focus goes to orbit losses. When particles are born in unconfined orbits, they are lost almost immediately after the injection (first orbit losses). The rate of unconfined orbits depends strongly on the NBI direction: co-current injection reduces significantly the rate of first orbit losses. The motion of EPs obtained by NBI is strongly influenced by drifts, as already explained in section 2.3.2. Without these contributions particles would move along the same flux surface, remaining always confined once born in a confined orbit. Considering the magnetic equilibrium presented at the beginning of the chapter (section 4.1.2), the gradient and curvature drifts are directed in the same directions. According to drift effects, it is possible to define the loss boundaries for co-moving and counter-moving particles. The former is the low field side (LFS) while the latter is the high field side (HFS). Since DTT NBI occurs in the co-current direction, which is opposite to the toroidal magnetic field, EPs are counter-moving particles ($\lambda < 0$). Their losses therefore would be significant if counter-moving particles were injected near the HFS. However this is not the case for DTT NBI, since the neutral beam is injected tangentially to the torus from LFS. Information about the motion and orbit typology of EPs at energy E can be obtained observing where particle orbit points are located on the topological map designed in figure 4.12. In the following section, the interpretation of the EP topological map is explained.

4.3 Interpretation of the EPs topological map in CoM phase space

By equations (4.8)-(4.10), (4.15) and (4.20), the topological map in the phase space (P_ϕ, μ) can be designed. Considering the plasma reference scenario of DTT and fixing the energy of EPs at the injection energy E = 510 keV, orbit boundaries are represented in Figure 4.12. Since P_ϕ and μ are constant a point in the phase space describes the entire EP orbit. However, it is also necessary to keep in mind the following observations for a complete interpretation of the orbit boundary map.

- Each point in the map is described by the intersection of the orbit with the horizontal axis defined by $z = z_{ax}$. Since each orbit crosses z_{ax} two times (if it is not immediately lost), each point lies on the intersection of two different parabolas. Passing particles move without changing $v_\parallel$ sign and therefore λ sign. Then the same sides (left or right) of two different parabolas intersect for the orbit of a passing particle. For trapped orbits instead, since $v_\parallel$ changes sign during the motion of EPs, trapped points lie on intersections of opposite sides (left-right or right-left sides) of two different parabolas. Examples of passing or trapped particles are shown respectively in figures 4.13 and 4.14. Moreover, the closer the point is to one boundary curve, the closer the particle pass to that boundary.
- Parabolas for the maximal and minimal radial positions R_M, R_m are two boundary curves. If a particle crosses z_{ax} at radial positions $R > R_M$ or $R < R_m$, it means that the particle is lost. An example is shown in figure 4.15.

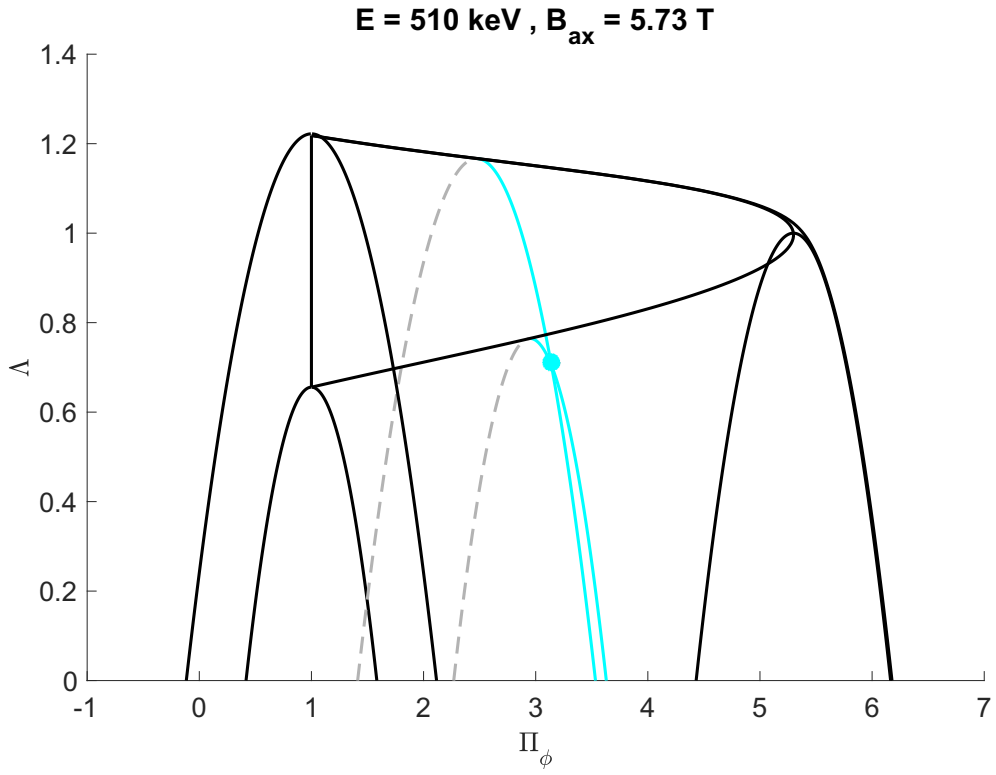

Figure 4.13: Topological map at $E = 510$ keV with example of a passing particle orbit. Its position corresponds to the intersection of the same sides of two different parabolas at the two radial positions where EP orbit intersect the axis $z = z_{ax}$.

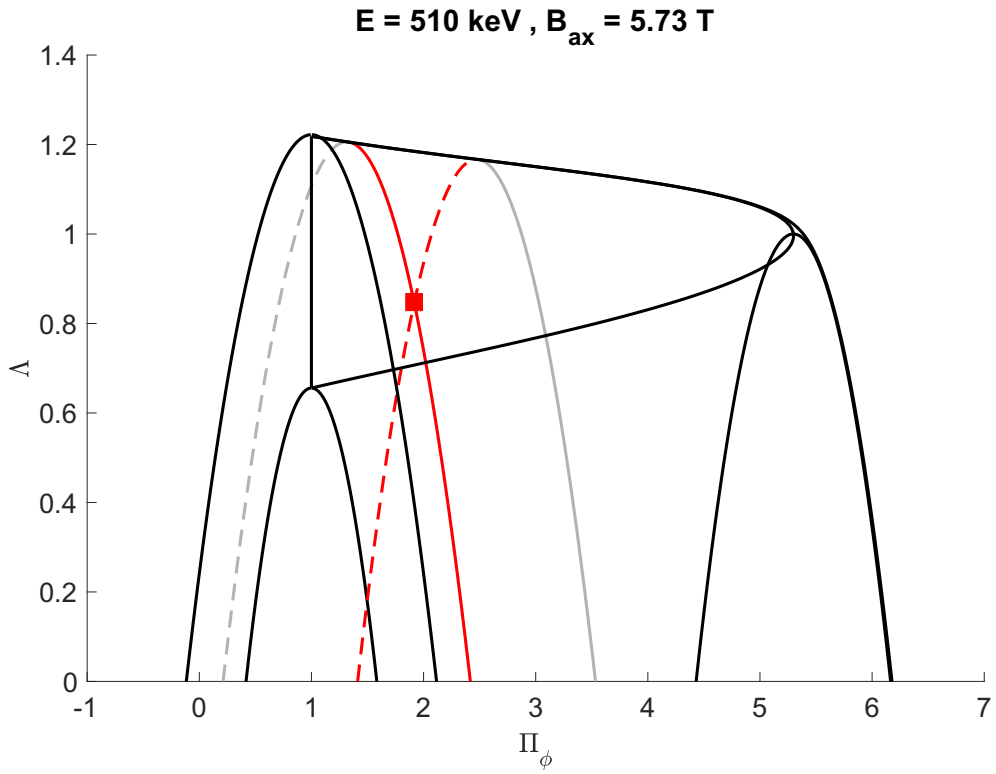

Figure 4.14: Topological map at $E = 510$ keV with example of a trapped particle orbit, whose position corresponds to the intersection between two opposite sides of two parabolas.

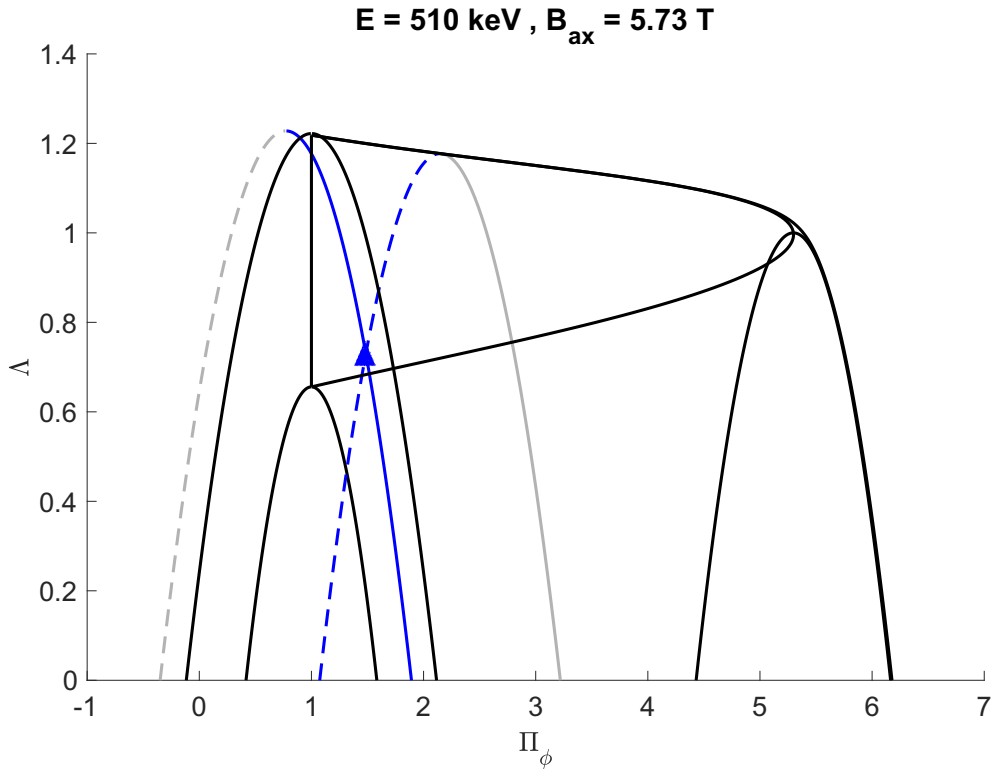

Figure 4.15: Topological map at $E = 510$ keV with an examples of lost particle orbit. In this particular case, it is a lost trapped particle. The position of the point related to this particle corresponds to the intersection between two different sides of two parabolas. The condition to be lost is related to the fact that one of the two intersected parabolas is defined by $R \notin [R_m, R_M]$ (in this particular case, $R > R_M$).

The orbit boundaries defines a topological map which can be populated by points representing EP orbits, as done in section 4.4. The location in which these points lie determines their collisionless trajectory. Different regions in the CoM phase space can be therefore identified. Through color coding, these regions are defined in figure 4.16. It is possible to distinguish regions for passing, trapped, potato and stagnation orbits, also in terms of confined and lost particles, according to the magnetic equilibrium considered for DTT.

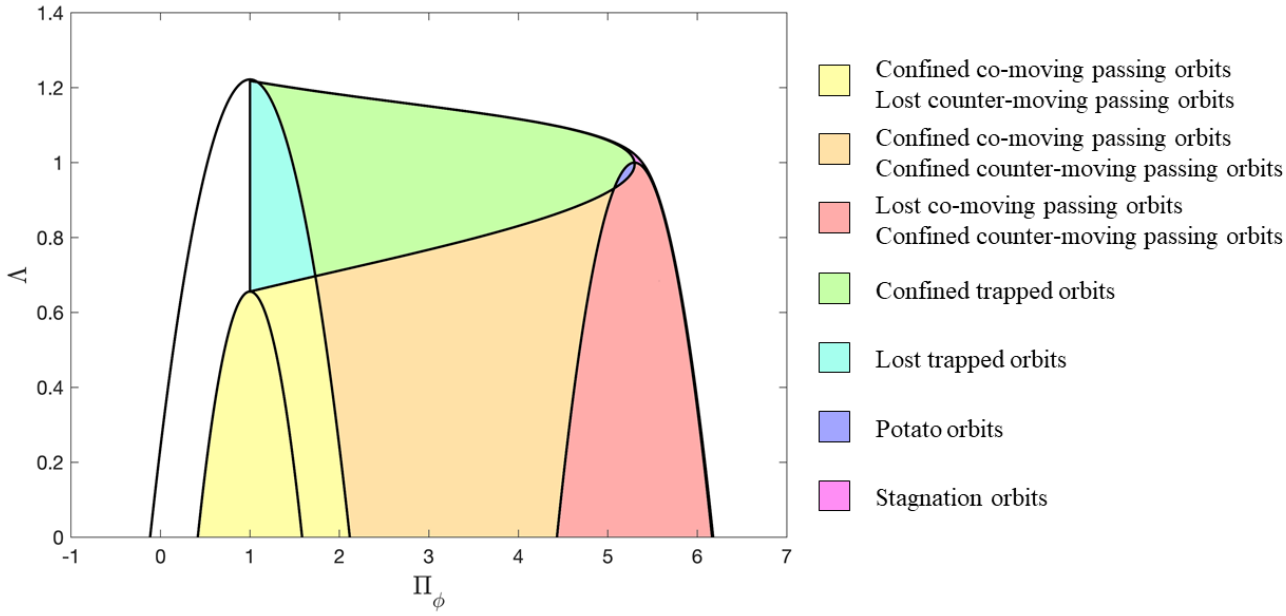

Figure 4.16: Topological map for EP orbits in CoM phase space at fixed energy $E = 510$ keV. Different orbit regions are represented by different colors.

To conclude the presentation of the EPs topological phase space, the dependence on the z vertical coordinate is illustrated. As written before, boundary equations (4.8)-(4.10), (4.15), (4.20) are defined in terms of $\Psi(R)$, $g(R)$, $B_\phi(R)$, $B_{tot}(R)$ radial profiles obtained at $z = z_{ax}$. Changing the vertical position considered, also these radial profiles change and this implies some modifications on the topological map. Up to now, z_{ax} was assumed as the vertical coordinate at which the radial profiles are computed. However it must be taken into account that EPs studied in this work are obtained from the NBI on DTT and EPs are born in a broader z range (see e.g. figure 3.11). Topological boundaries are now built considering different vertical coordinates to observe possible changes. The coordinates considered are $z_{ax} - 10$ cm, z_{ax} and $z_{ax} + 10$ cm. The result is shown in figure 4.17. It is possible to observe that the vertical positions don't affect strongly the topological map. Only the magnetic axis boundary is shifted but this is an effect derived mainly from the normalization. The stream function at the LCFS Ψ_a, to which Π_ϕ depends (equation (4.6)), remains the same for all the three studied cases. What changes is the stream function Ψ_{ax} at the magnetic axis which is different for different vertical coordinates. These changes however are not significant in the topological map since also the trapped-passing boundary and the stagnation boundary move with respect to the magnetic axis and therefore orbit domains remain basically the same. This implies that we can consider the beam as injected only at $z = z_{ax}$ as a good approximation.

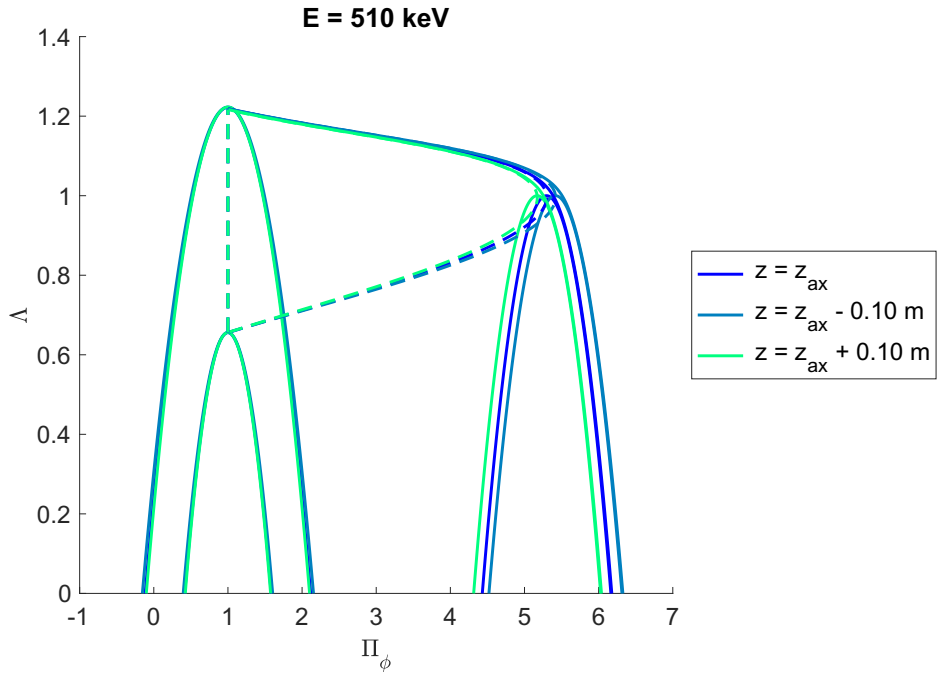

Figure 4.17: Topological maps for different vertical positions at fixed energy E = 510 keV.

In the following sections, topological maps at $z = z_{ax}$ are populated with particle orbits obtained from ASCOT simulations already presented in chapter 3. It must be taken into account that those ASCOT simulations consider collisions between particles. Collisions between fast ions and plasma particles determine a decrease of fast ion energies, since EPs energy is transferred to plasma particles by Coulomb collisions. The end-state of all these particles, i.e. the end of slowing down process, cannot be described just by one EPs topological map since particle energies at the endstate are significantly different (see section 4.4.4) and their orbits therefore populate topological map designed at different energies. However, the main interest of this analysis is on EP first orbit losses, which occur during the initial motion of particles around the torus. The collisional time is slower than that required for a particle to complete a toroidal turn into the plasma. Therefore, if a particle is lost in a few toroidal turns, it will be lost also considering collisions. The EP topological map in a collisionless approach is therefore useful to obtain an hint about the EP losses after the NBI. ASCOT outputs are used to populate the topological map at E = 510 keV in the CoM phase space defined by (Π_ϕ, Λ, E) with EP orbits immediately after particle ionization. Examples of EP orbits on the EP topological map are reported in the next subsection to show, with a reduced sample of particles, their location on the map and their relative motion around the torus. In particular, a collisionless simulation was performed for 100 particles to study the EP orbits "zoology" observed in DTT.

4.3.1 EP orbit "zoology"

The aim of this section is to show an EP orbit "zoology" obtained by neutral beam injection in DTT. In particular, a selection of passing, trapped and lost trapped particles is shown to relate the particle trajectory representations in the real space to their location on the CoM phase space. The selected particle typologies are types of particles that mostly populate the plasma after the NBI injection. Considering the plasma reference scenario (see section 2.1.1) and the injection energy $E_{\mathrm{NBI}} = 510$ keV, another ASCOT simulation has been performed writing output information at different timestep, necessary to draw particle orbits in the (x,y) and (R,z) plane of the torus. Particle orbits on the toroidal and poloidal planes[2] are reported in terms of the guiding centre location.

Starting from passing particle orbits, some examples are reported in figures 4.18, 4.19 and 4.20, where the toroidal and poloidal projections of three particle orbits and their relative mapping on the CoM

[2]respectively (x,y) and (R,z) planes

phase space are reported. These particles are identified respectively by the particle id numbers 16, 12 and 100. Recalling the figure 4.16, in which orange and red regions contains confined counter-moving particles, it is possible to observe that orbits of passing particles 16, 12 and 100 are located properly in passing orbit domains. Their (R,z) projections however shows some important differences. In particular, the particle 16 is born close to the plasma edge while the particle 100 close to the magnetic axis. This can be also observed in their positions in the EP topological map, since particle 16 orbit is located near the LFS edge, while particle 100 orbit on the magnetic axis (MA) curve. Particle 12 orbit is instead located approximately in the middle of the right-sides of the LFS and MA parabolas. Its trajectory on the (R,z) plane shows that particle 12 neither passes close to the magnetic axis neither to the LFS or HFS edges. In the three (R,z) projections, where also the flux surfaces are reported (dashed lines), it is possible to appreciate the drift effect which affect the particle motion. The total drift, derived from the gradient and curvature drift components, shifts particle downward. This drift is larger for particle 16 (figure 4.18), due to the larger gradient felt by the particle during its motion around the torus. Particle 100 instead could be mistaken for a stagnation orbit. But stagnation orbits are passing orbits which do not enclose the magnetic axis during their motion around the torus. From the projection on the toroidal plane for the particle 100 (figure 4.20), it is possible to observe that the particle crosses slightly the magnetic field, defined by the dashed line on the middle of the torus. Therefore, particle 100 is classified as a quasi-stagnation particle.

Examples of trapped particle orbits and their relative locations on the EP topological map are shown in figures 4.21, 4.22 and 4.23. Particles which follow the depicted orbits are identified with particle id numbers 17, 54 and 83. The latter is a lost trapped orbit. All these orbits are located on the expected position with respect to the description in figure 4.16. Particle 17 represents a weakly trapped particle [3], since its banana tips are close to each others. This particle is located on the EP topological map near the trapped-passing boundary (purple curve). Particle 54 instead describes a moderately trapped particle, which represents the average behavior of trapped particles [3]. Its location on the EP topological map corresponds clearly to its nature of trapped particle. Particle 83 instead describes a lost trapped particle. Also its orbit point is located on the expected position in the CoM phase space. This particle is ionized on the upper region of poloidal section and its poloidal motion is directed upwards accordingly to its nature of counter-moving particle. On the lower part of the poloidal section, particle 83 crosses the LFS region during its first orbit becoming a lost particle. This indeed represents a first orbit losses. Due to the co-current injection, banana orbits close inwards. This reduce significantly the first orbit losses of trapped particle but if the external part of the banana hit the wall when returning to the starting point of its trajectory, the particle is lost. Looking at the (R,z) projections, also for trapped particles it is possible to observe drift effects, which shift particles to move downward, towards internal flux surfaces.

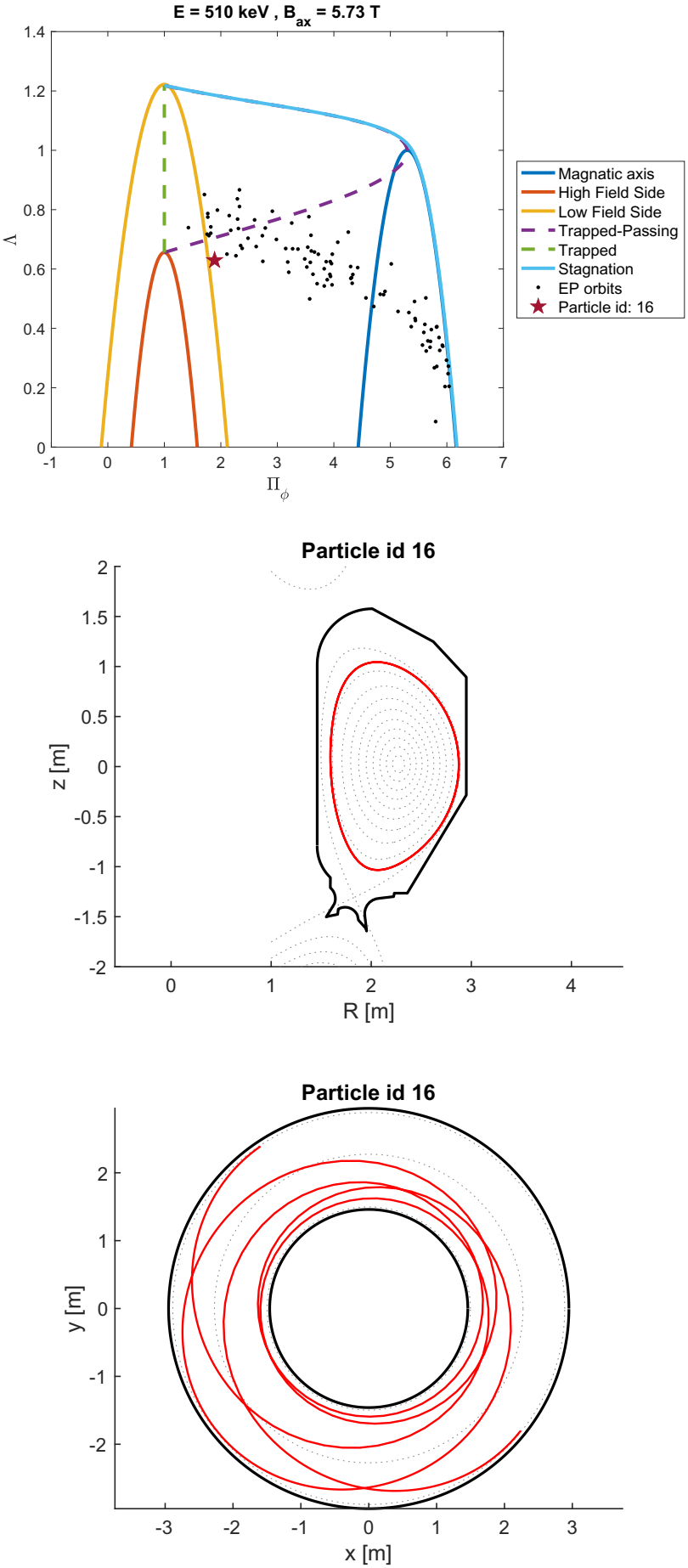

Figure 4.18: Orbit location of confined-passing particle 16 in the EP topological map at E = 510 keV for the DTT plasma reference scenario, together with the orbit projection on the (R,z) and (x,y) planes.

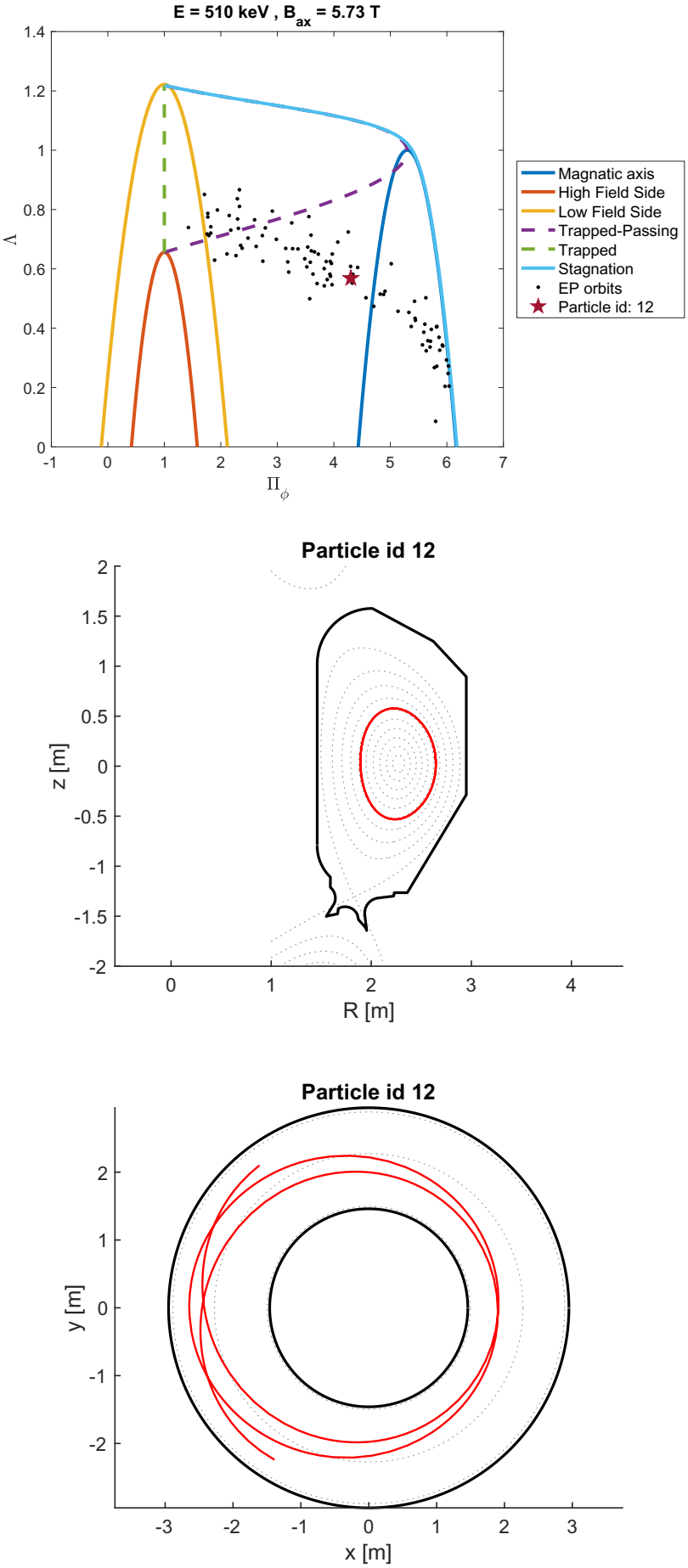

Figure 4.19: Orbit location of confined-passing particle 12 in the EP topological map at E = 510 keV for the DTT plasma reference scenario, together with the orbit projection on the (R,z) and (x,y) planes.

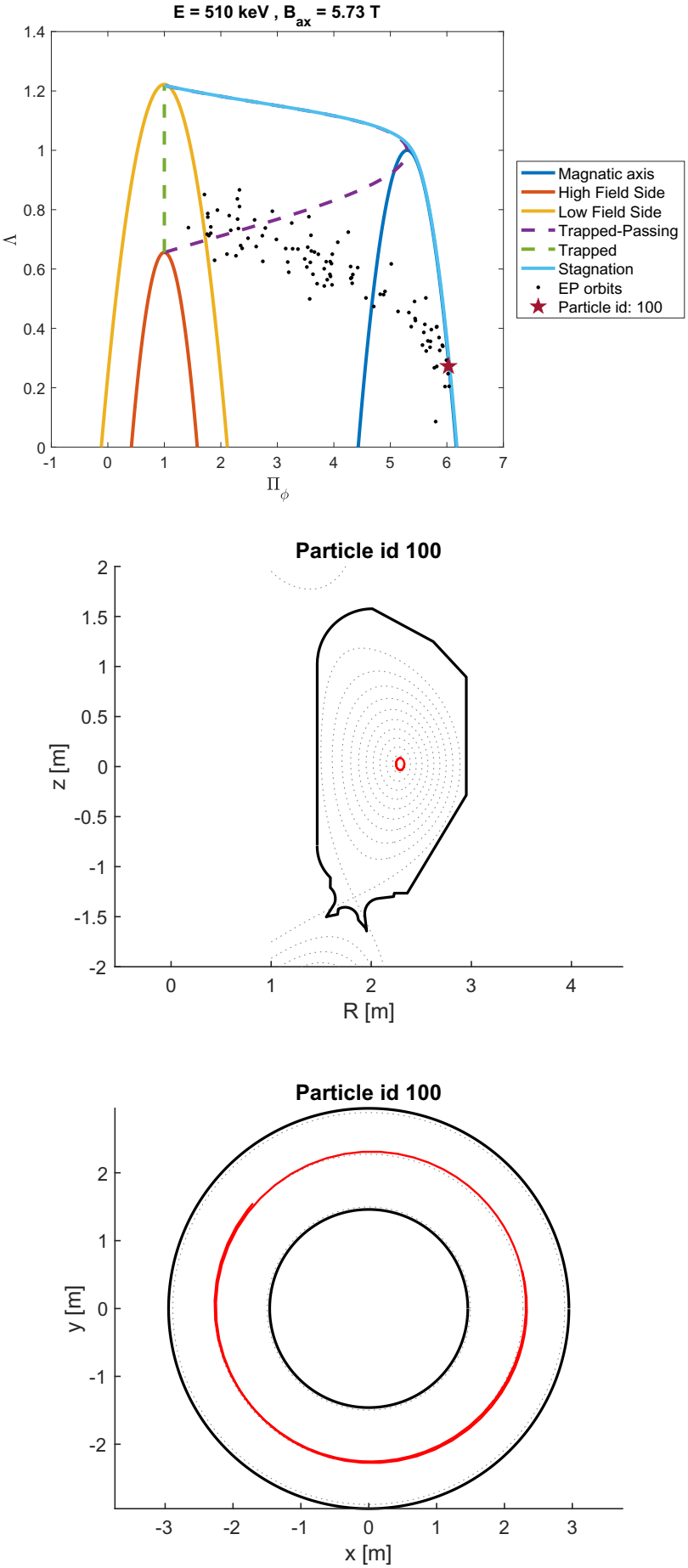

Figure 4.20: Orbit location of confined quasi-stagnation particle 100 in the EP topological map at E = 510 keV for the DTT plasma reference scenario, together with the orbit projection on the (R,z) and (x,y) planes.

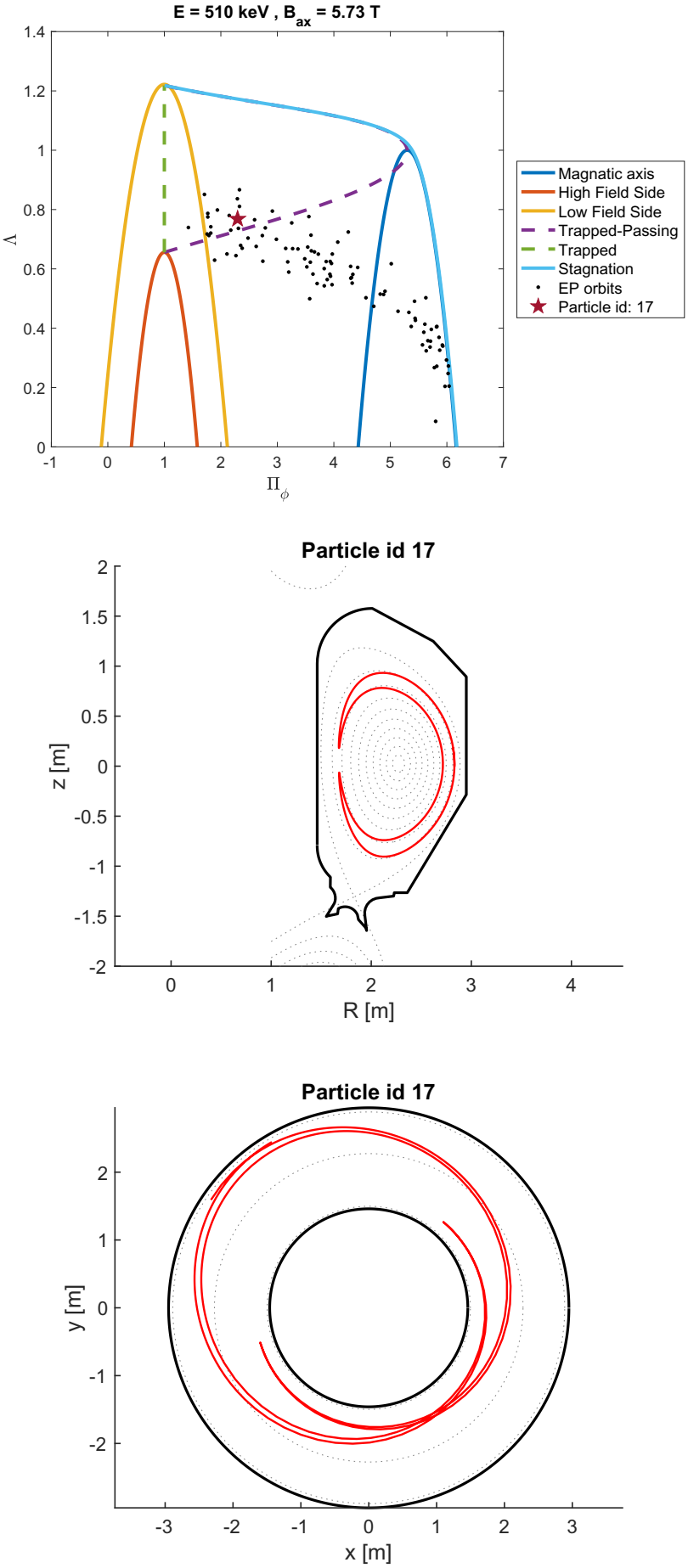

Figure 4.21: Orbit location of confined-trapped particle 17 in the EP topological map at E = 510 keV for the DTT plasma reference scenario, together with the orbit projection on the (R,z) and (x,y) planes.

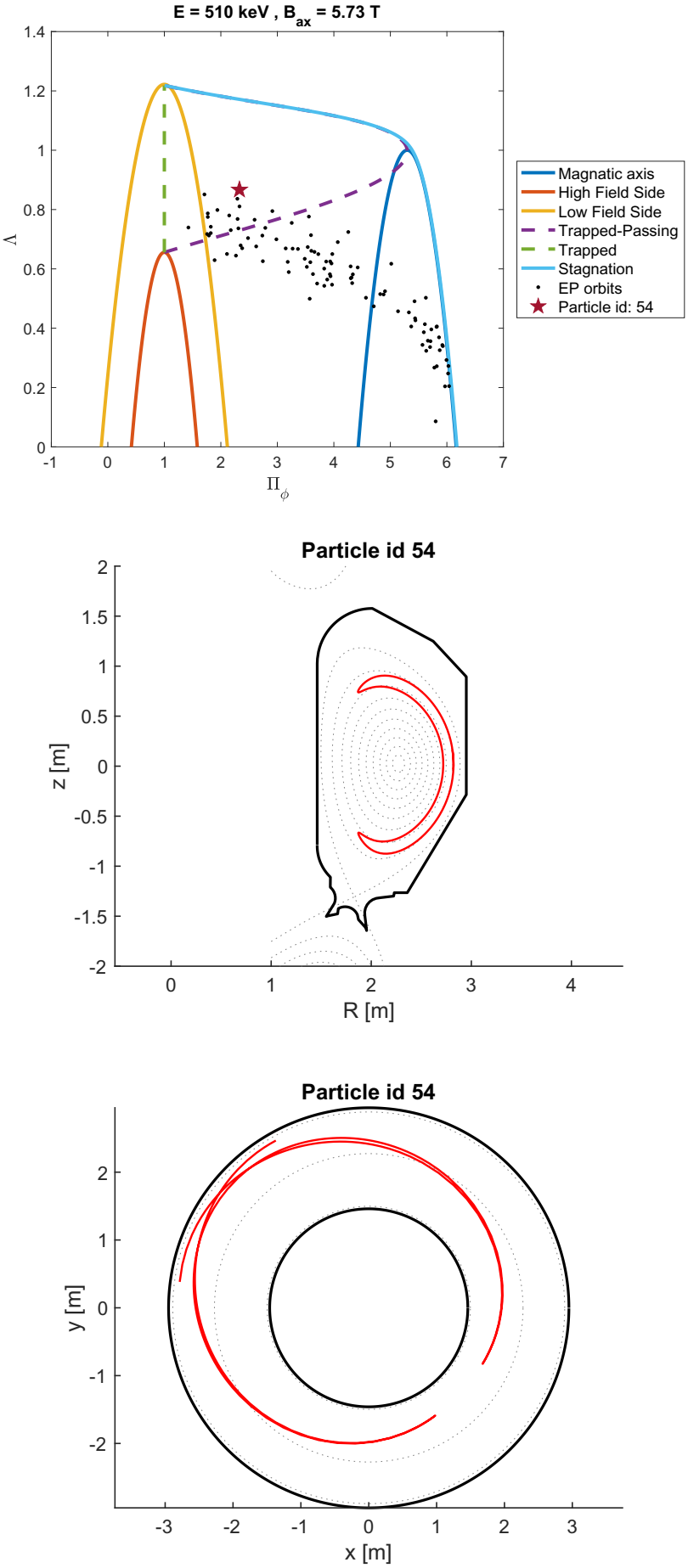

Figure 4.22: Orbit location of confined-terapped particle 54 in the EP topological map at E = 510 keV for the DTT plasma reference scenario, together with the orbit projection on the (R,z) and (x,y) planes.

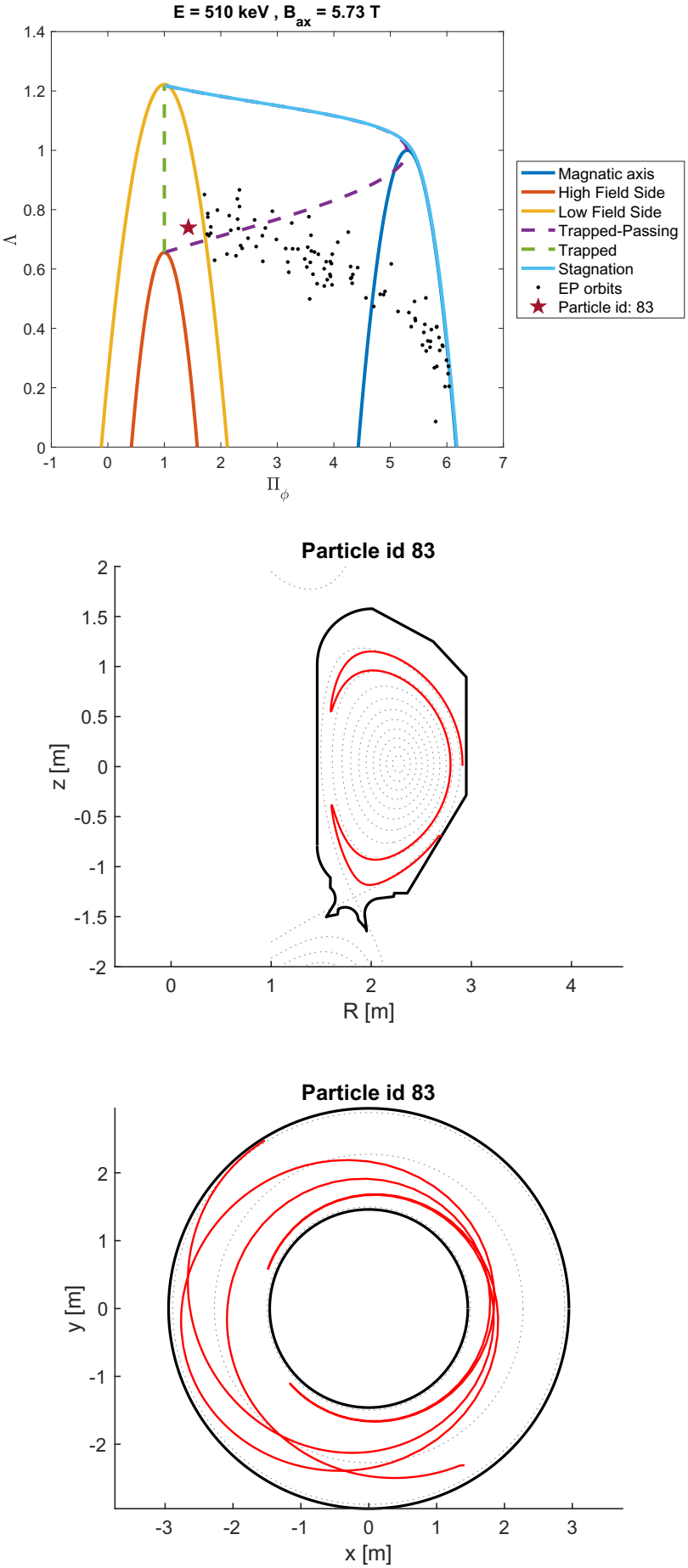

Figure 4.23: Orbit location of lost-trapped particle 83 in the EP topological map at E = 510 keV for the DTT plasma reference scenario, together with the orbit projection on the (R,z) and (x,y) planes.

4.4 ASCOT simulations of DTT NBI energetic particles

Making use of ASCOT simulations performed and presented in chapter 3, EPs topological maps are now built for DTT cases. The first map presented is built considering EPs born from neutral beam injection at $E_{\mathrm{NBI}} = 510$ keV for the DTT plasma reference scenario. Other maps are build considering different DTT plasma parameters or different particle injection energies. Changes in the plasma scenario are not expected to imply any significant modifications of the orbit boundaries that form the EP topological map but rather changes on EP constants of motion. Changes in particle injection energies imply some modifications of the orbit boundaries, due to their dependence on E. These changes are analyzed in the subsection (4.4.4). In the following subsections, all the topological maps for the parameter scans presented in chapter 3 are shown and compared to investigate how different plasmas and NBI energies modify the EPs behavior in terms of orbits. To read these maps, it is important to remember that DTT fast ions are counter-moving particles with respect to the magnetic field $\vec{B}$, characterized by a negative pitch ($\lambda < 0$). This means that, with the adopted COCOS, EP orbits lie on the right-side of parabolas drawn in the CoM phase space for different radial positions (see figure 4.13). For graphical reasons, only a sample of 100-1000 EP points are plotted in the following CoM phase spaces, representing the whole fast ion population in the EP topological map. The plotted EPs come from ASCOT simulations. As reported at the beginning of the chapter, particle orbits correspond to one single point in the topological map in the CoM phase space if P_ϕ, μ (and their dimensionless coordinates) are constant during the particle motion. Otherwise, points move in the topological map along EP orbit. If P_ϕ, μ are constant, just one point represents the entire trajectory. The assumption of constant magnetic moment μ (and its dimensionless version Λ) is verified in the next subsection.

4.4.1 Constant magnetic moment

All the EP topological maps are built assuming that the toroidal canonical angular momentum P_ϕ and the magnetic moment μ are constant. Precisely, μ is an adiabatic invariant, meaning that its value remains constant over time scales typical of the particle motion for small variations of the magnetic field. However, in DTT and all tokamaks, the magnetic field changes significantly from HFS (high field side) to LFS (low field side), passing from $B_\phi(R_m) \sim 8.55$ T to $B_\phi(R_M) \sim 4.44$ T (at z_{ax}). To verify the validity of constant μ assumption, and therefore constant Λ, an ASCOT simulation was performed following particles during their collisionless motion in the plasma, writing EP outputs at a fixed timestep. Indeed, ASCOT can write outputs at different timesteps[3], with e.g. information about the particle pitch and position in a (R,z) spatial grid during the particle motion. From these information it is possible to compute (Π_ϕ, Λ) coordinates for each timestep of the particle trajectories and plot them in the EP topological map to observe if Λ is conserved. Orbit points are represented in figure 4.24 (a) for all the timesteps obtained by ASCOT for three different EPs. These particles are particle 83, 16, 100, whose trajectories were already shown in section 4.3.1 representing respectively a lost trapped particle, a passing particle near the LFS and a passing particle close to the magnetic axis (quasi-stagnation particle). It is possible to see that as the particle is moving inside the plasma, also the orbit point is slightly moving on the EPs topological map [44], showing fluctuations on Π_ϕ and Λ. Figures 4.24 (b), (c), (d) show a zoom of orbit points representing the entire trajectories of particles 83, 16 and 100.

[3]The simulations analyzed in chapter 3, and used also in this chapter, were performed without writing particle information at fixed time-steps, but just writing information about their initial (ionization) and final (thermalization) state.

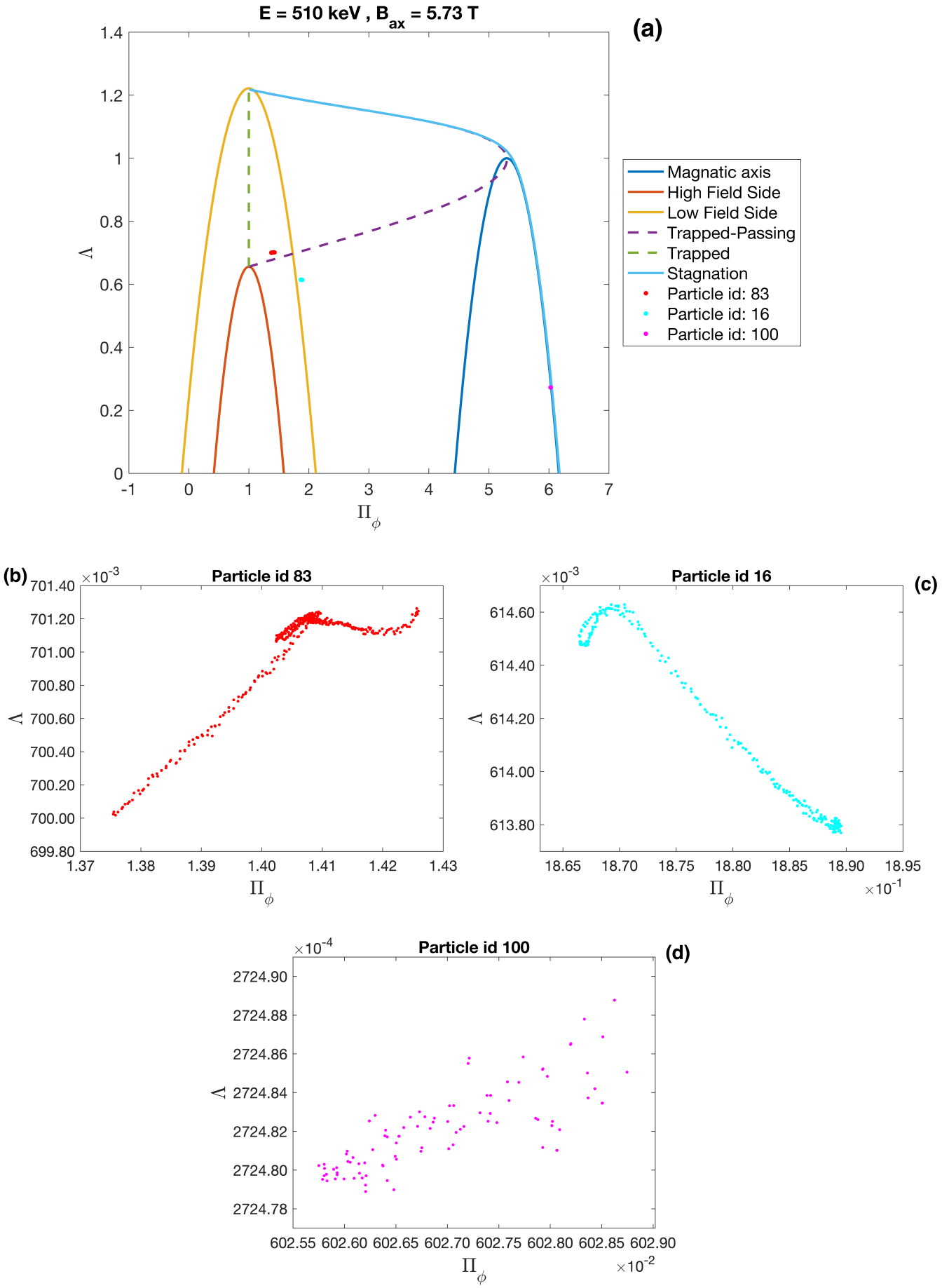

Figure 4.24: (a) EP topological map with orbits for three different energetic particles (id 83, 16, 100) plot to show fluctuations on Π_ϕ and Λ along their orbit. Figures (b), (c), (d) show a zoom of their coordinates where variations of toroidal canonical angular momentum and magnetic moment can be better appreciated.

The values of the small fluctuations of Λ and Π_ϕ visible in figures 4.24 (b), (c) and (d) are reported in table 4.3. Fluctuations reported are defined as $\Delta\Lambda = \Lambda_{max} - \Lambda_{min}$ and $\Delta\Pi_\phi = \Pi_{\phi,max} - \Pi_{\phi,min}$, where *max* and *min* subscripts stay for maximum and minimum values. Inside brackets, the percentage variations with respect to the average values of Λ, Π_ϕ for each particle is reported. It results indeed that Λ, Π_ϕ are conserved during particle orbits and the small variations detected on Π_ϕ are likely due to numerical inaccuracy. Λ, Π_ϕ can therefore be assumed constant during the particle orbit with good approximations. This means that the entire collisionless trajectory of particle inside the plasma can be represented by just one point in the topological map.

Particle id	$\Delta\Lambda$	$\Delta\Pi_\phi$
83	1.2e-3 (0.17%)	5.1e-2 (3.6%)
16	8.6e-4 (0.14%)	2.3e-2 (1.2%)
100	9.9e-6 (0.003%)	3.0e-3 (0.05%)

Table 4.3: Λ and Π_ϕ fluctuations for particle orbits of figure 4.24.

4.4.2 EP topological map for DTT plasma reference scenario

First, the EP topological map for DTT plasma reference scenario is presented. To populate the EP map, it is necessary to compute the coordinate (Π_ϕ, Λ) for each particle, using the normalized form of equations 4.4. Pitch and radial position of each energetic particle at their initial state (ionization) are given by ASCOT as outputs. The radial profiles of $\Psi(R), g(R_\Psi), B_\phi(R_\Psi)$ are then computed at z_{ax}. Indeed, it is assumed that EP are all born at z_{ax}, even if the ionization cloud is spread vertically in a range approximately of $[z_{ax} - 10\ cm, z_{ax} + 10\ cm]$ (as can be estimated from 3.11). The validity of this approximation is already discussed in section 4.3. The particle energy used to built the EP topological map corresponds to 510 keV, i.e the beam injection energy. The topological map populated by EP orbits for the DTT plasma reference scenario is shown in figure 4.25.

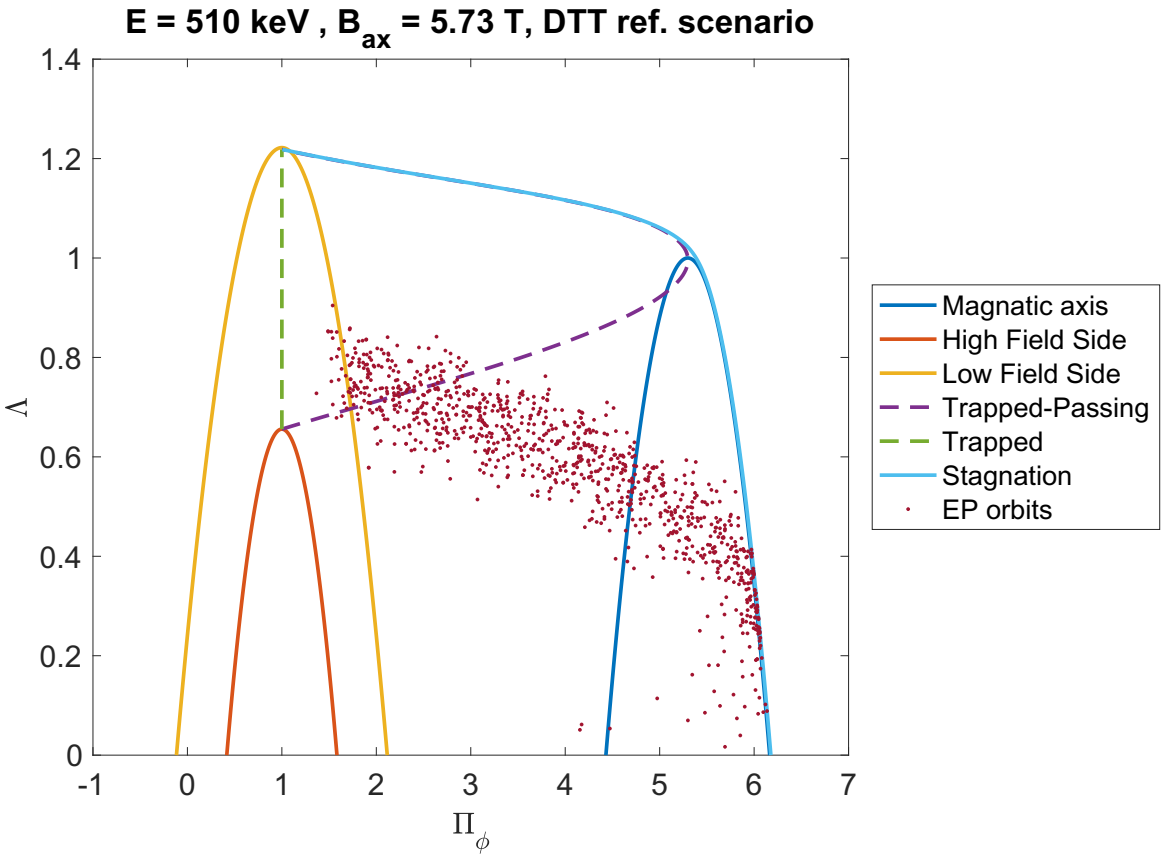

Figure 4.25: EP orbit topological map at E = 510 keV considering the reference DTT plasma.

Just looking at figure 4.25 it is possible to determine that the number of passing particles is greater than that of trapped particles, since the region of counter-moving passing particle is more populated than that of trapped particles. This is something expected and desired, since trapped particles are easier to be lost with respect to passing particles. Points located on the right-side of the magnetic axis (blue curve) describes particle trajectories close to the magnetic axis. They complete toroidal turns moving scarcely in the poloidal direction and therefore can be called as quasi-stagnation particles. Passing particle points located near to the low field side (yellow curve) instead describe orbits close to the plasma edge. It is possible to observe then a small number of points (about $\sim 2\%$) in the region of lost trapped particles. Points in this area describe first orbit losses of trapped particles. Just one orbit in the sample of 1000 particles is located in the region for lost counter-moving particle (see figure 4.16). Also this point represents a first orbit loss. Some example of passing, trapped and lost particle orbits are shown in section 4.3.1. No potato or stagnation orbits are identified in this topological map. In the next section, the EPs topological map for particles injected for different DTT plasma parameters are presented and compared to this case to observe how orbit population changes.

4.4.3 EP topological maps for DTT plasma scenarios with different temperatures and densities

As for ASCOT simulations in chapter 3, DTT plasma reference scenario has been modified changing plasma temperatures at fixed plasma densities, and viceversa. The orbit populations analyzed in this subsection refers to plasmas characterized by electron temperatures equal to 0.5 T_e and 1.5 T_e (fixed plasma density), and electron densities equal to 0.5 n_e and 0.25 n_e (fixed plasma temperature), with respect to the plasma used to determine orbits in subsection 4.4.2. The changes on T_i, n_i are reported in sections 3.1 and 3.2. Figures 4.26 and 4.27 show orbits on the EP topological maps by ASCOT simulations performed changing the plasma temperatures. Figures 4.28 and 4.29 show instead orbits obtained by ASCOT simulations performed changing the plasma density.

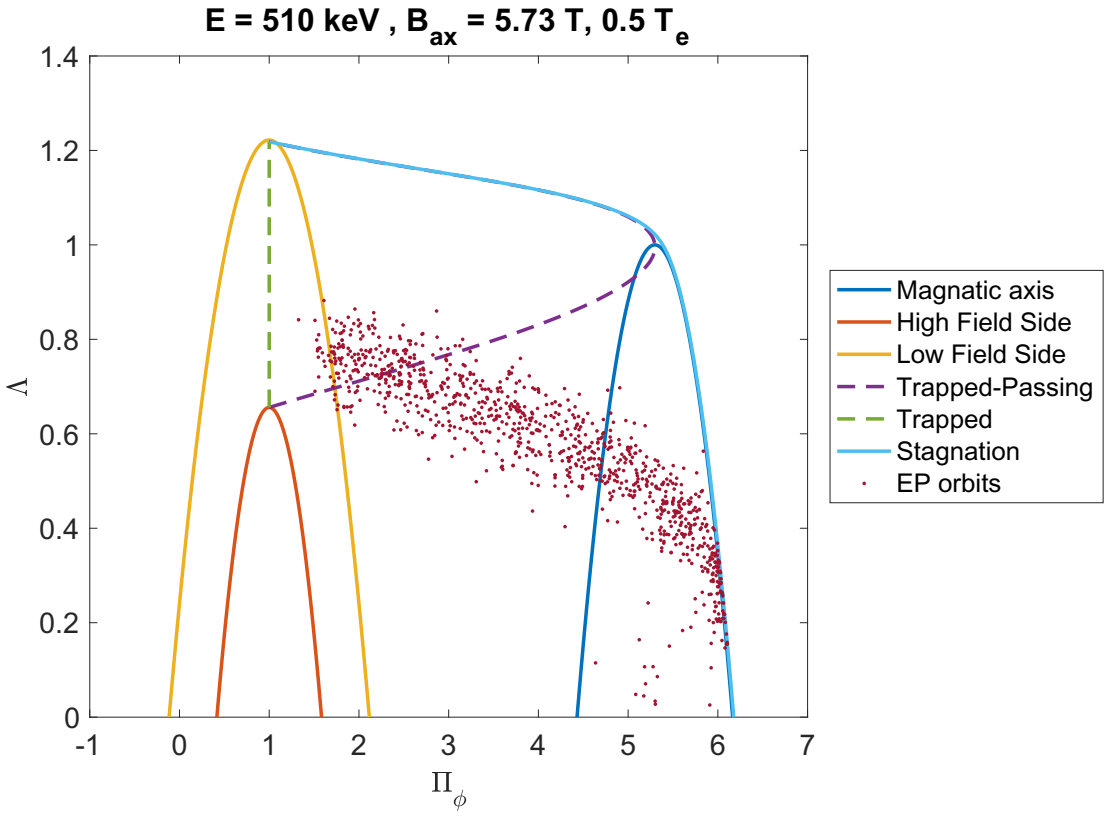

Figure 4.26: EP topological map at E = 510 keV considering a plasma with T_e and T_i multiplied by a factor 0.5.

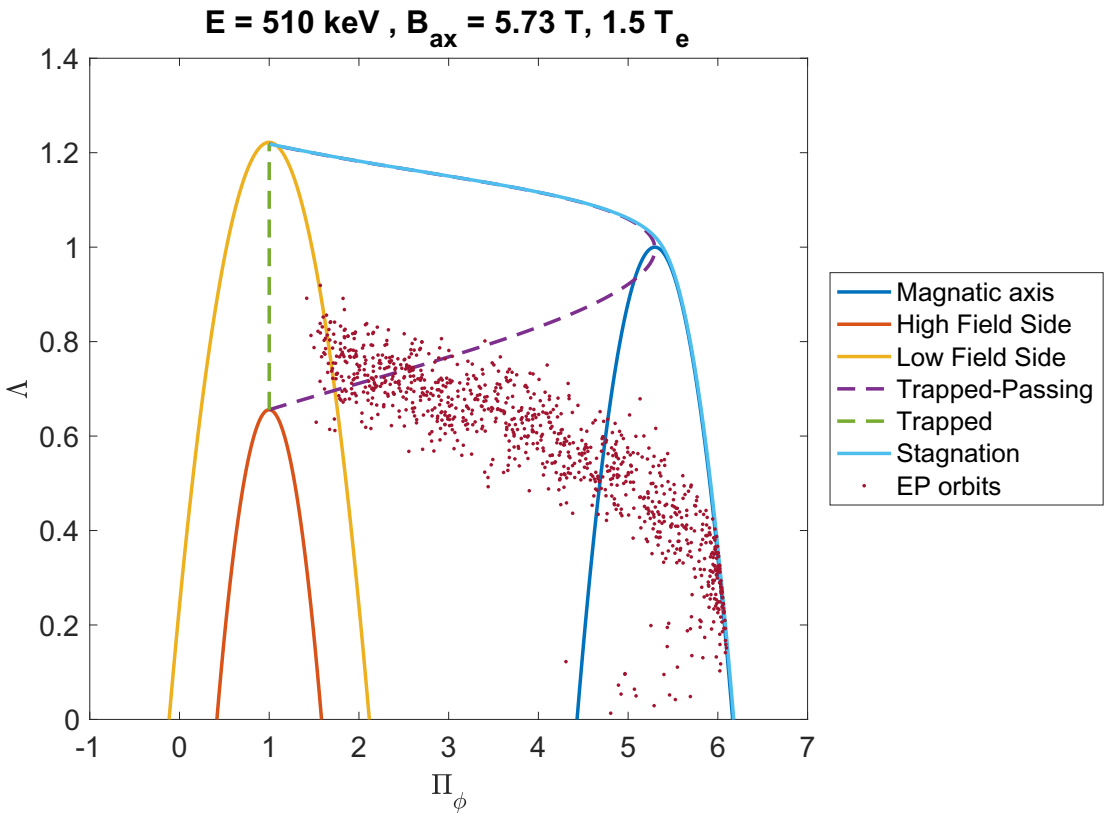

Figure 4.27: EP topological map at E = 510 keV considering a plasma with T_e and T_i multiplied by a factor 1.5.

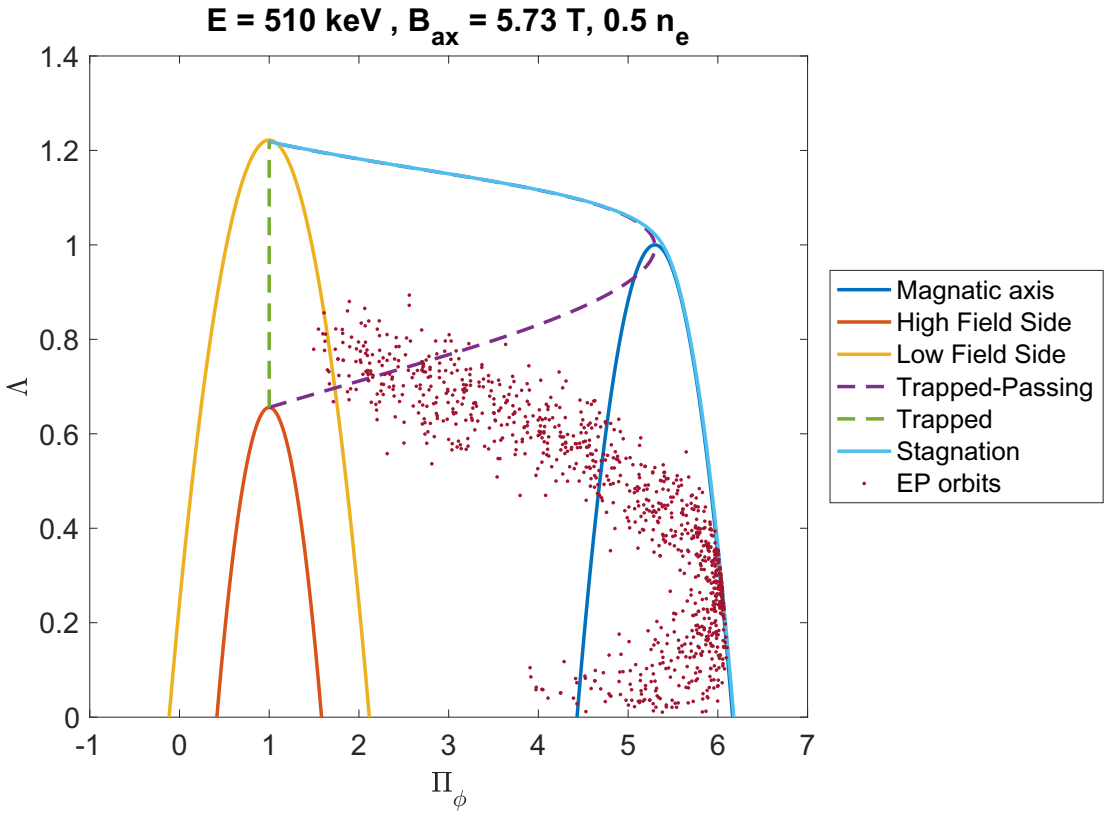

Figure 4.28: EP topological map at E = 510 keV considering a plasma with n_e multiplied by a factor 0.5 and n_i computed through equation (3.1).

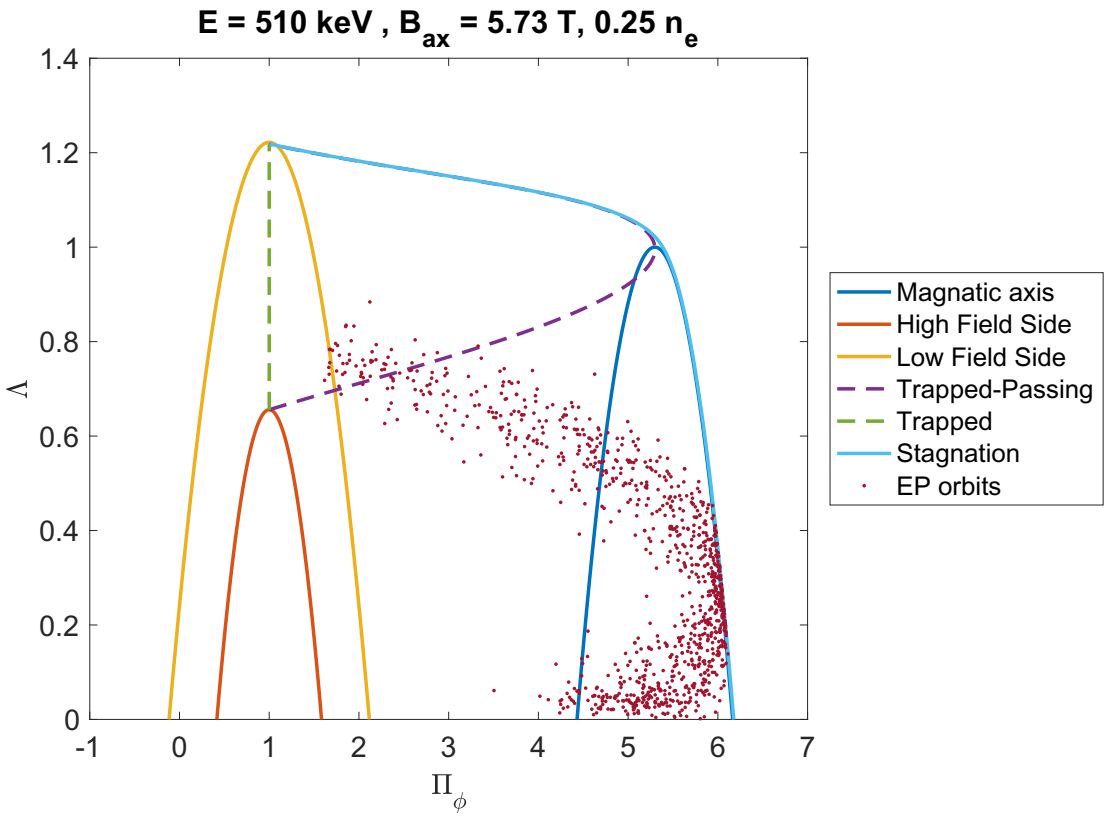

Figure 4.29: EP topological map at E = 510 keV considering a plasma with n_e multiplied by a factor 0.25 and n_i computed through equation (3.1).

The EP topological maps related to plasmas with different temperatures are commented first. No significant changes are observed with respect to the EP topological map obtained for the reference DTT plasma. Changing the plasma temperatures indeed the particle ionization positions are not changed significantly and therefore the particle orbits on the EP topological map remain located approximately on the same domains.

About EP topological maps populated with particle orbits evolved in different plasma densities, a strong variation can be observed on the orbit points location. Decreasing the plasma density, the fraction of trapped particles decreases. Comparing the plasma reference scenario and the 0.25 n_e scenario, the number of orbit points in the trapped particle region is drastically reduced. Also the percentage of first orbit losses derived from lost trapped particle decreases to 0.6%. Concerning passing particle orbits, also their distributions changes on the phase space. At 0.25 n_e passing particles populate mostly positions with low values of Λ. Since $\Lambda \propto (1-\lambda^2)$ this can derives from the fact that the pitch λ has larger values, i.e. the parallel[4] velocity $v_{\parallel}$ is larger than the ones obtained by injection at the plasma reference scenario. This would explain also the reduction of trapped particle losses. The larger parallel velocity at low plasma density is the results of two NBI effects. The first consists on the larger penetration of the neutral beam into the plasma. Neutrals become ionized deeper in the plasma core at lower plasma density. This can be seen in figure 4.30, where the fast ion birth density profile is reported as a function of ρ_{pol}. The second effect instead concerns the tangential direction of the NBI. Tangential injection implies that, for EPs born near the magnetic axis, their velocity is mainly parallel to the magnetic field lines. Therefore their orbits are characterized by lower values of Λ ($\lambda \sim 1$). Therefore the large fraction of EPs born close to the magnetic axis, where the parallel velocity component dominate the particle motion, justifies the distribution of the orbit population observed in figure 4.28 and even more clearly on 4.29. Finally, for plasma density scan too, potato or stagnation orbits are not observed.

[4]parallel with respect to the magnetic field lines

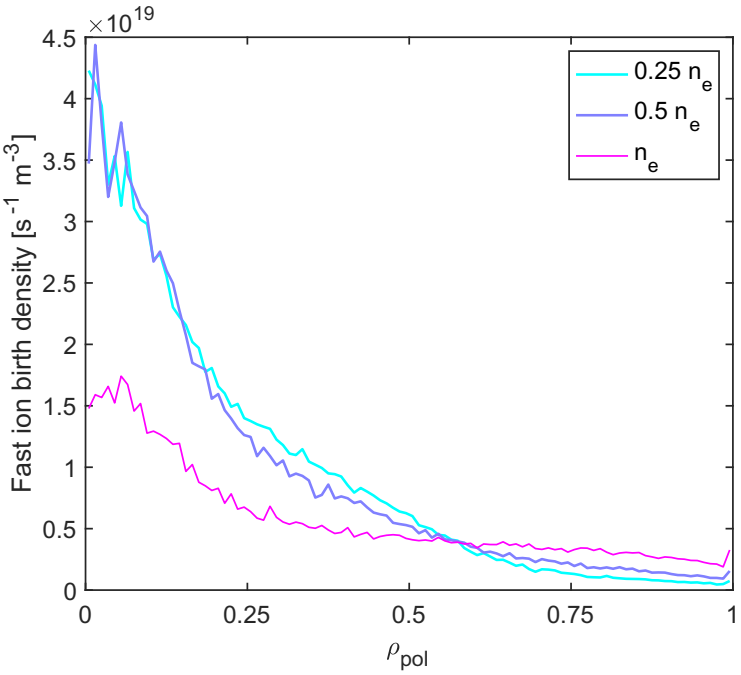

Figure 4.30: Fast ion birth density profile for different plasma densities with respect to DTT reference scenario.

4.4.4 EP topological maps for different NBI energies

As last plasma scan, EP topological maps at different NBI energies are discussed. EP orbits are simulated by ASCOT for the DTT reference plasma scenario. Before showing these maps, the dependence of the topological maps on the particle energy is discussed, since boundary curves defined previously depend on the particle energy E. In chapter 2, when introducing particle motion, drifts and orbits, it was discussed how larger energy of fast ions determines larger drifts effects and different orbits topology. This difference can be noted also building the EPs topological maps. Figures 4.31 and 4.32 show respectively the topological maps at E = 8 keV and E = 3 MeV which corresponding respectively the ion thermal energy at the plasma core and the alpha particle energy.

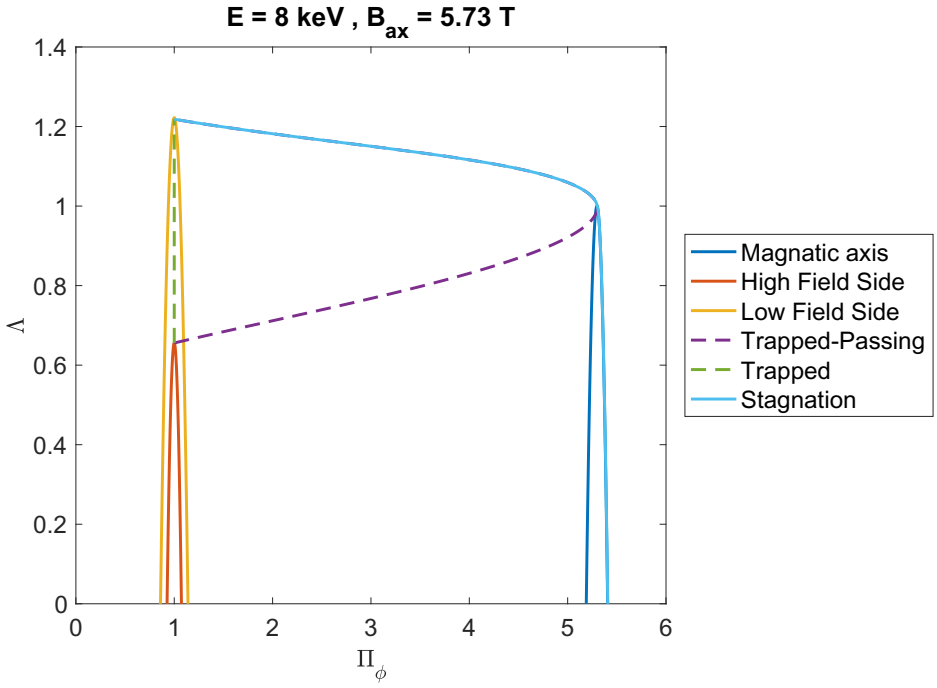

Figure 4.31: EP topological map at E = 8 keV considering the plasma reference scenario.

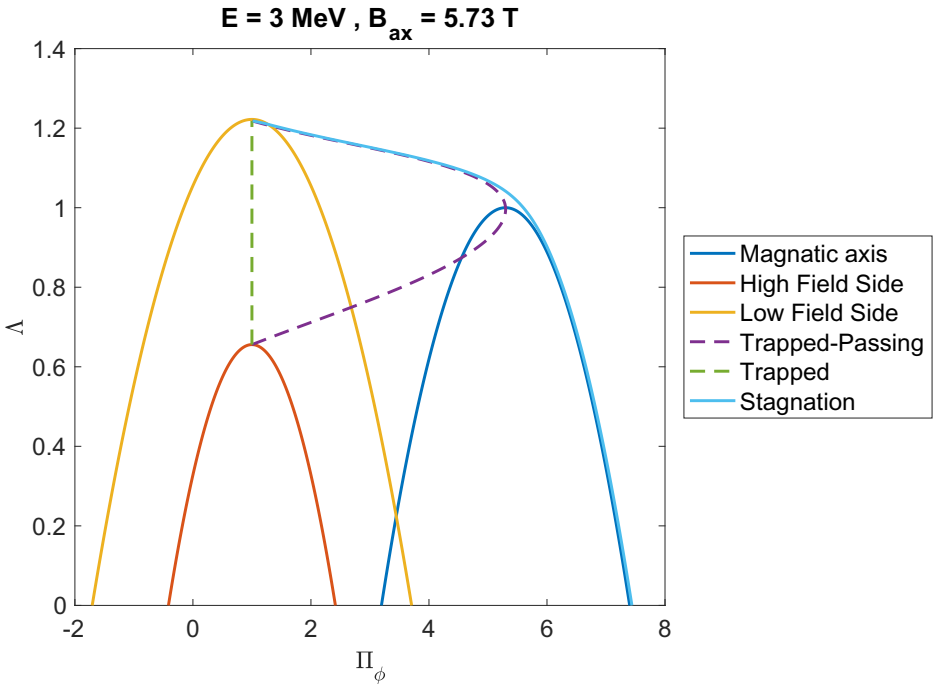

Figure 4.32: EP topological map at E = 3 MeV considering the plasma reference scenario.

As it can be seen from figures 4.31 and 4.32, changing the energy, the structure made by boundary curves is strongly modified. Looking at the EP topological map at the lower energy, domains of passing and trapped particles are larger than other maps while potato and stagnation domains are reduced. The Π_ϕ values range for passing boundary curves is restricted. These curves indeed appear more thinner than the same curves on EP maps at higher particle energy. Increasing the particle energy, the boundary curves tend to overlap each others. Looking at the EP topological map built with E = 3 MeV, it is possible to observe that magnetic axis and low field side curves intersect forming new regions, e.g. the domain in which co-moving particles are confined while counter-moving are lost. At high energy, particle orbits are larger and therefore the confined particle domains are restricted. These changes on the topological maps at different energies become significant comparing situations where energies have different orders of magnitude. Indeed, the analysis performed changing the NBI energy, and so the EP energy, from 510 keV to 300 keV are not affected by relevant changes in orbit boundary structure. The EP topological maps at 400 keV and 300 keV and their orbit population are reported in figures 4.33 and 4.34.

Observing these figures it is possible to see that decreasing the energies, particles tend to move to trapped orbits, since the trapped particle regions is more populated at 300 keV than that at 400 keV and 510 keV. Moreover the fraction of lost trapped particles slightly increases at $\sim 2.5\%$, with respect to $\sim 2\%$ of the plasma reference scenario case. The motion towards trapped particle domains derives from a lower penetration of the neutral beam inside the plasma for NBI energy at 300 keV than that at 400 or 510 keV. The reduced penetration changes both the ionization position of particles, which happens closer to the low field side, and the particle pitch λ which assumed lower values, i.e. higher value of Λ, than those at higher NBI energy. Observing figure 4.35, it is possible to notice that the fast ion birth density close to the plasma edge is larger at 300 keV than that at higher injection energies. Therefore, EPs are mainly born in regions where the dominant velocity component is perpendicular with respect to the magnetic field lines. This is in agreement with the presence of a larger fraction of trapped particles. Similarly to previous analyses, potato and stagnation orbits are not observed.

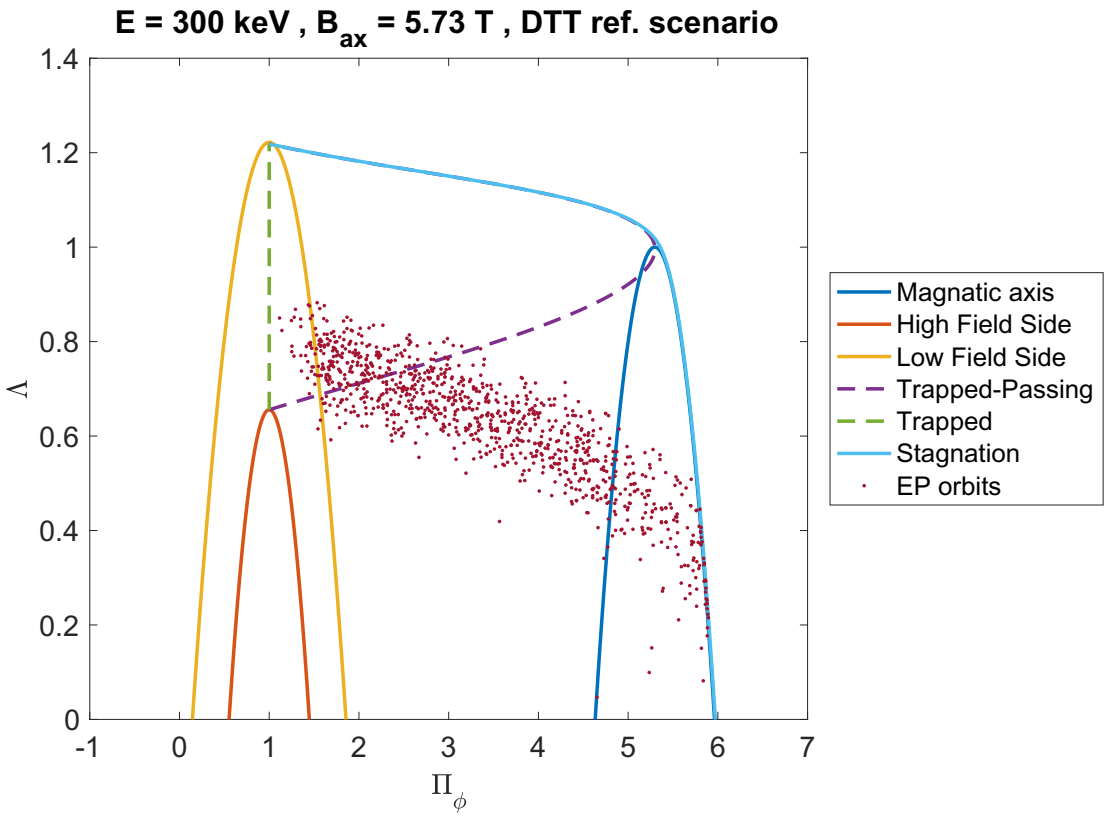

Figure 4.34: EP topological map at E = 300 keV considering the plasma reference scenario.

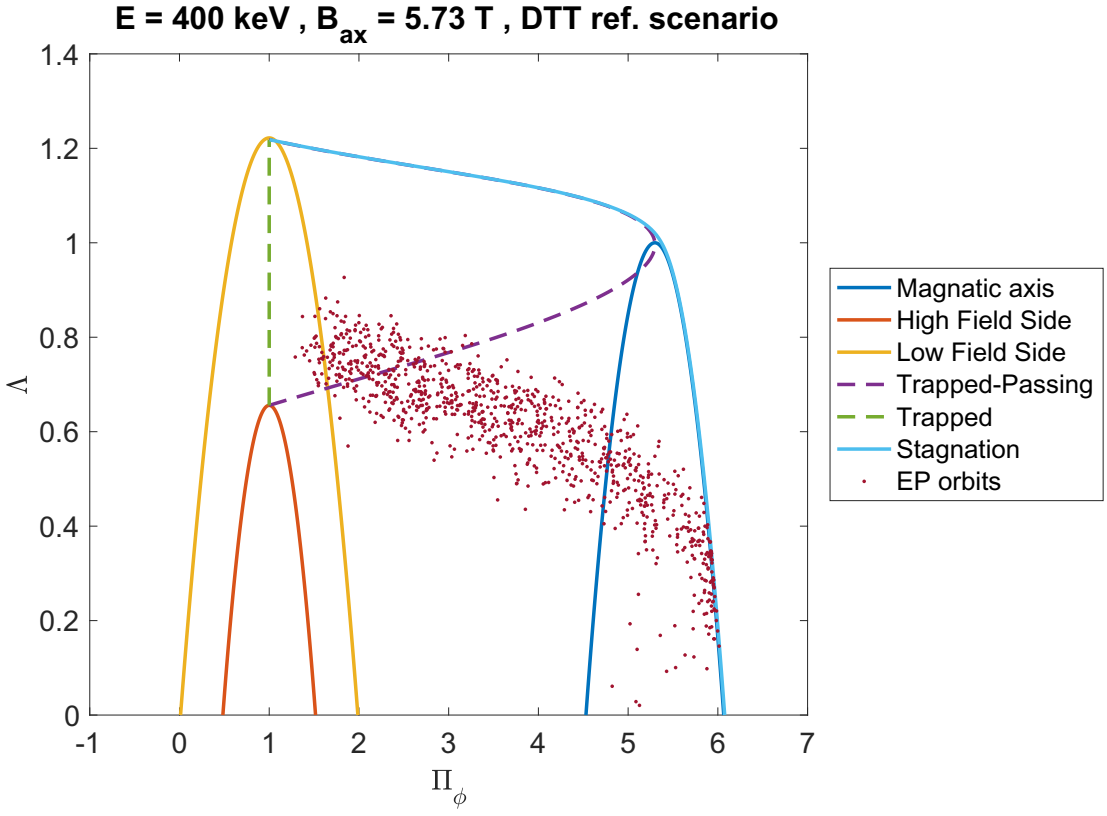

Figure 4.33: EP topological map at E = 400 keV considering the plasma reference scenario.

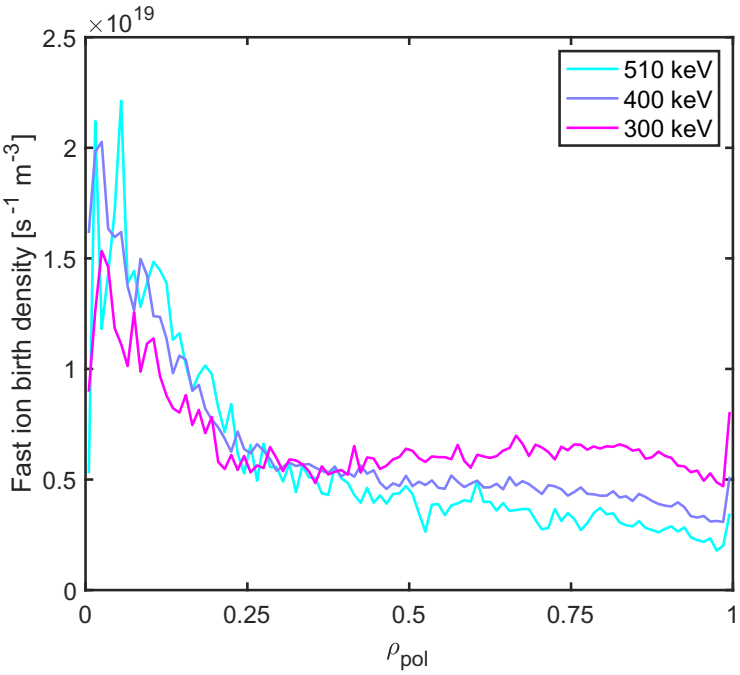

Figure 4.35: Fast ion birth density profile for different NBI energies.

4.5 Concluding remarks

The analysis presented in this chapter provides the DTT community with the first complete topological analysis of EP orbits in DTT with ASCOT code. The use of the EP topological map built in the CoM phase space turns out to be an efficient tool for the particle orbit classification and to estimate first orbit losses in the collisionless scenario. Indeed this kind of particles is lost before collisions due to the faster motion of EPs around the torus than the time required for particle collisions. Some concluding remarks are reported here to summarize results obtained from the analyses of orbit population for different DTT plasma parameters and NBI energies.

NBI energetic particles follow different kinds of orbits in DTT. In particular, passing, trapped and lost particle orbits are identified. No potato or stagnation orbits are observed. This kind of trajectories are more likely to happen at higher injection energies and lower magnetic fields. As can be seen in figure 4.32 for particle with an energy of 3 MeV, the region for potato orbits is wider than that at lower energy. Fractions of passing particles and trapped particles change considering different plasma scenarios and different injection energies. In particular, passing particle fraction increases if the plasma density decreases. Particles indeed penetrate deeper into the plasma and therefore are characterized by larger pitch λ. Particle orbits in the EP topological map therefore populate region with smaller values of Λ, as can be seen in figure 4.29. An opposite effect is instead observed when the NBI energy is decreased (or density increased). The neutral beam particles are ionized closer to the plasma edge and show a smaller particle pitch that implies larger values of the magnetic moment. Therefore, in the EP topological map, particle orbit points tend to move to trapped orbit domain and the fraction of passing particle decreases. This can be observed e.g. in figure 4.34. Concerning the fraction of trapped orbits, it decreases when the plasma density decreases or the NBI energy is increased. By changing the plasma temperature, the fractions of passing and trapped particles do not change significantly.

From this analysis it is also possible to observe that the fraction of first orbit losses is low (around $\sim 2\%$ for the plasma reference scenario). By changing the plasma scenario or the NBI energies, no significant changes are observed regarding first orbit losses. From the topological map reported in this chapter, the efficiency of the co-current NBI in DTT in the reduction of first orbit losses is confirmed.

Chapter 5

Conclusions

This thesis investigates beam-plasma interaction and energetic particles (EPs) confinement and losses in the forthcoming Divertor Tokamak Test (DTT) device. DTT will be indeed equipped with a state-of-the art Neutral Beam Injection (NBI) system capable of generating a high-energy ($E_{\mathrm{NBI}} = 510$ keV), high power ($P_{\mathrm{NBI}} \sim 10$ MW) beam. A good confinement of EPs is essential both for plasma performances and to avoid potentially harmful EP losses to the machine first wall. Using the orbit-following Monte Carlo ASCOT code, systematic modelling of EP dynamics is performed for different plasma conditions and different NBI energies, focusing on the beam-plasma interaction physics (chapter 3) and orbit and losses analyses (chapter 4) through a topological map in the phase space defined by EP constants of motion and adiabatic invariant. The analyses presented in this work are among the first performed for DTT using ASCOT code and will contribute to the power mix optimization of target DTT operating scenarios for the different operational phases where the NBI system will be in use.

Concerning NBI-plasma interaction, in chapter 3 analyses, several 0D quantities are estimated by ASCOT, as the absorbed power and the driven current obtained by NBI, for different plasma and NBI energy conditions. It results that the absorbed power is reduced significantly when the plasma density decreases. This derives from shine-through losses, i.e. a fraction of the beam that is not ionized and is directly lost to the wall. The current driven by the NBI instead increases when NBI energy or plasma temperature increase. Increasing the NBI energy, the efficiency of the current drive increases. This derives from the increase of the cross section with the electrons with respect to that of ions. Therefore, fractions of energy and momentum transferred by collision to electrons increase with the NBI energy and so also the current drive efficiency. Increasing plasma temperature instead leads to a larger current drive since the resistivity of the plasma decreases as $\propto T_e^{-3/2}$. At lower plasma density, the NBI current drive is larger than all the other studied cases but the absorbed power is not maximum due to large EP losses making low plasma density scenarios not suitable for DTT operation. Scans on plasma parameters are done considering independent changes on temperature and density even if real situations imply that changes on plasma temperatures lead to changes into plasma densities too. Nevertheless, a plasma temperature scan is useful in devices where also the Radio-Frequency (RF) heating systems are used, as in DTT. A RF system can indeed provide heat on localized plasma regions at fixed plasma density. When using the neutral beam injection combined with RF, it must be taken into account that the critical energy changes with the plasma temperatures, as shown in figure 3.5, impacting on the fraction of NBI power going to plasma electrons and ions.

In chapter 4 a detailed analysis of EP orbits and collisionless EP loss phenomena is illustrated through a EP orbit classification in the topological map defined in the Constant of Motion (CoM) phase space. The CoM phase space is defined by the constants of motion Π_ϕ and E and the adiabatic invariant Λ, which are respectively the normalized toroidal canonical angular momentum, the particle energy and the normalized magnetic moment. NBI energetic particles follow different kinds of orbits. In particular in DTT, passing, trapped and lost particle orbits are identified looking at the EP topological map, while no potato or stagnation orbits are observed. The fraction of passing particles shows a dependence on

the plasma densities. Indeed, particle orbit population moves inside the EP topological map towards passing orbits characterized by low values of Λ (i.e. large pitch λ) when the density is decreased. This is due to the deeper beam penetration into the plasma. An increase in trapped particle orbits instead is observed when the NBI energy is decreased. This is expected since the beam penetration at low energy is lower and therefore neutrals are ionized mainly on the outer side of the torus, where the fraction of trapped particles is expected to be larger. First orbit losses are of particular interest representing one possible source of losses that arises from the neutral beam injection. In DTT, NBI is directed in the same direction of plasma current, condition that guarantees a small fraction of trapped, immediately-lost, EPs. However a fraction of first orbit losses remains and this can be observed from the orbit population on the EP topological maps. Their fraction in the reference plasma scenario is $\sim 2\%$. First orbit losses occur on timescale faster than those related to collisions between fast ions and plasma particles and this justifies the collisionless analysis performed in chapter 4. The EP topological map in the constant of motion phase space is confirmed to be a useful and fast analytical tool to investigate possible EP orbits and their relative first orbit losses.

Regarding possible future work, this analysis can be completed by further investigations on EP behavior in different plasma scenarios. For example, it is of interest to observe the EP behavior in plasma scenarios expected during the initial experimental phase, called "phase 0", planned for DTT (see figure 2.3), where the magnetic field is halved. During the "phase 0", the NBI system will not be yet installed. However, for experimental reasons, the reduced magnetic field scenario will be likely reproduced in later phases too, when the NBI will be in operation. Another interesting analysis is to consider different divertor configurations and plasma shapes. The DTT purpose is indeed to the test possible alternatives to the single null divertor configuration. Through the EP modelling it is possible to investigate how EP confinement and losses change for different divertor configurations, obtaining information about the most effective application of NBI for alternative divertor configurations proposed for DTT. The fast ion modelling can be performed also considering non-axisymmetric magnetic field, e.g resulting from the ripple effect [27], i.e. the toroidal variations of the magnetic field due to the finite number of coils used to generate the toroidal component. This effect determines possible specific EP losses, called ripple losses. ASCOT is in fact capable of treating a 3D magnetic field input, therefore the ripple effect can be considered. The analyses presented in this thesis, and the further analyses proposed, are essential to allow for the most effective use of NBI in DTT device, that will be operational soon before 2030.

Appendix A

Variable naming conventions

In this appendix the main variable naming conventions used in this thesis are reported.

a	Torus minor radius
A,Z	Mass and charge numbers
β	Beta parameter defined as the ratio between the plasma pressure and the magnetic pressure
$B_{\theta,R}$, $B_{\theta,z}$	Components of the poloidal magnetic field
B_p	Poloidal component of the magnetic field
B_T, B_ϕ	Toroidal component of the magnetic field
B_{tot}	Total magnetic field
$B_{tot,ax}$	Total magnetic field at the magnetic axis
$E, E_\parallel, E_\perp$	Particle kinetic energy and relative parallel and perpendicular components
E_c	Critical energy
E_{NBI}	NBI energy
ϵ_0	Vacuum permittivity
η	Plasma resistivity
η_{CD}	Current Drive efficiency
g	Free function defined as g = RB_ϕ
I_p	Plasma current
λ	Particle pitch, where $\lambda > 0$ defines *co-moving particles* while $\lambda < 0$ defines *counter-moving particles*, both with respect to the magnetic field $\vec{B}$
λ_D	Debye length
Λ_D	Plasma parameter
μ,Λ	Magnetic moment and its dimensionless version called normalized magnetic moment
M_{col}	Collisional torque
n	Plasma density, which can be distinguished in electron density n_e and ion density n_i
P_{NBI}	NBI power
P_{tot}	Heating power

p_ϕ,Π_ϕ	Toroidal canonical angular momentum and its dimensionless version called normalized toroidal canonical angular momentum
q, m	Particle charge and mass
ρ_{pol}	Normalized poloidal flux function
(R,ϕ,z)	Cylindrical coordinates, where R and z are the radial and vertical positions while ϕ the toroidal angle
R_0	Torus major radius
R_0/a	Aspect ratio
(R_0, z_0)	Radial and vertical coordinates of the torus geometrical axis
(R_{ax}, z_{ax})	Radial and vertical coordinates of the magnetic axis
r_L	Larmor radius or gyro-radius
R_M, R_m	Radial position of the low field side and the high filed side
τ_E	Energy confinement time
τ_s, t_s	Slowing down time and Spitzer slowing down time
τ_{tor}	Time required to complete a toroidal turn
T	Plasma temperature, which can be distinguished in electron temperature T_e and ion temperature T_i
$\vec{v}$	Particle velocity
$v_\parallel, v_\perp$	Parallel and perpendicular components of particle velocity defined with respect the magnetic field $\vec{B}$
$\vec{v}_{\nabla B}$	Drift velocity derived by the magnetic field gradient ∇B
$\vec{v}_d$	Total drift velocity felt by particles
$\vec{v}_E$	Drift velocity derived by the presence of an electric field $\vec{E}$
$\vec{v}_F$	Drift velocity derived by a external force $\vec{F}$
$\vec{v}_k$	Drift velocity derived by a curved magnetic field with curvature radius $\vec{R}_c$
$\vec{v}_p$	Drift velocity derived by electric and magnetic field time variations
Ψ, Ψ_{pol}	Poloidal flux surface per radiant, also called stream function
Ψ_{ax}, Ψ_a	Stream function at the magnetic axis and the last closed flux surface
$(\psi_{pol}, \phi, \theta)$	Flux surface coordinates, where ψ_{pol} is the poloidal flux function and ϕ, θ respectively the toroidal and poloidal angles
ω_c	Gyro-frequency
Z_{eff}	Effective charge number

Bibliography

[1] T. Donné et al. European research roadmap to the realisation of fusion energy (long version). 2018.

[2] IEA. World energy outlook 2021. URL: https://gotcp.net/wp-content/uploads/2021/10/WEO2021_Launch_Presentation-1.pdf.

[3] J.P. Freidberg. *Plasma physics and fusion energy*. Cambridge University Press, 2007.

[4] A.R. Choudhuri. *The physics of fluids and plasmas. An introduction for astrophysicists*. Cambridge University Press, 1998.

[5] R. Martone et al. DTT - Divertor Tokamak Test facility–interim design report. Technical report, ENEA, 2019.

[6] T. Klinger et al. Overview of first Wendelstein 7-X high-performance operation. *Nuclear Fusion*, 59(11):112004, 2019.

[7] M. Zuin et al. Overview of the RFX-mod fusion science activity. *Nuclear Fusion*, 57(10):102012, 2017.

[8] A. Iiyoshi et al. Overview of the Large Helical Device project. *Nuclear Fusion*, 39(9Y):1245, 1999.

[9] M. Kikuchi, K. Lakner, and M. Q. Tran. *Fusion Physics*. IAEA, 2012.

[10] P. Vincenzi, P. Agostinetti, R. Ambrosino, T. Bolzonella, I. Casiraghi, A. Castaldo, C. De Piccoli, G. Granucci, P. Mantica, L. Pigatto, A. Snicker, and M. Vallar. Interaction of high-energy neutral beams with divertor tokamak test. Submitted to Fusion Engineering and Design, 2022.

[11] J. Mailloux et al. Overview of JET results for optimising ITER operation. *Nuclear Fusion*, 62(4):042026, jun 2022.

[12] ITER. https://www.iter.org/.

[13] Image from EFDA website. URL: https://web.archive.org/web/20140110094526/http://www.efda.org/fusion/focus-on/limiters-and-divertors/.

[14] Consorzio RFX. https://www.igi.cnr.it/.

[15] R. Ambrosino. DTT - Divertor Tokamak Test facility: A testbed for DEMO. *Fusion Engineering and Design*, 167:112330, 2021.

[16] I. Casiraghi et al. First principle-based multi-channel integrated modelling in support of the design of the divertor tokamak test facility. *Nuclear Fusion*, 61(11):116068, 2021.

[17] H. Eubank et al. Neutral-Beam-Heating results from the Princeton Large Torus. *Phys. Rev. Lett.*, 43:270–274, 1979.

[18] P. Agostinetti et al. Improved conceptual design of the beamline for the DTT Neutral Beam Injector. *IEEE Transactions on Plasma Science*, pages 1–6, 2022.

[19] P. Barabaschi, Y. Kamada, H. Shirai, and the JT-60SA Integrated Project Team. Progress of the JT-60SA project. *Nuclear Fusion*, 59(11):112005, 2019.

[20] R. Koch. Fast particle heating. *Fusion Science and Technology*, 61(2T):275–285, 2012.

[21] E. Speth. Neutral beam heating of fusion plasmas. *Reports on Progress in Physics*, 52(1):57, 1989.

[22] J. Wesson. *Tokamaks*. Oxford University Press, 2004.

[23] W.W. Heidbrink and R.B. White. Mechanisms of energetic-particle transport in magnetically confined plasmas. *Physics of Plasmas*, 27(3):030901, 2020.

[24] Image from Euro Fusion website. https://www.euro-fusion.org/news/detail/detail/News/from-doughnuts-to-bananas/.

[25] F.H. Tenney. Confinement of energetic alphas in TCT and tritons in PLT. Technical report, Princeton Univ., NJ (USA). Plasma Physics Lab., 1975.

[26] R.B. White. *The theory of toroidally confined plasmas*. Imperial college press, 2014.

[27] G. Spizzo et al. Collisionless losses of fast ions in the divertor tokamak test due to toroidal field ripple. *Nuclear Fusion*, 61(11):116016, 2021.

[28] L.G. Eriksson and F. Porcelli. Dynamics of energetic ion orbits in magnetically confined plasmas. *Plasma Physics and Controlled Fusion*, 43(4):R145, 2001.

[29] J. Varje, K. Särkimäki, J. Kontula, P. Ollus, T. Kurki-Suonio, A. Snicker, E. Hirvijoki, and S. Äkäslompolo. High-performance orbit-following code ASCOT5 for monte carlo simulations in fusion plasmas. *arXiv preprint arXiv:1908.02482*, 2019.

[30] E. Hirvijoki, O. Asunta, T. Koskela, T. Kurki-Suonio, J. Miettunen, S. Sipilä, A. Snicker, and S. Äkäslompolo. ASCOT: Solving the kinetic equation of minority particle species in tokamak plasmas. *Computer Physics Communications*, 185(4):1310–1321, 2014.

[31] O. Asunta, J. Govenius, R. Budny, M. Gorelenkova, G. Tardini, T. Kurki-Suonio, A. Salmi, and S. Sipilä. Modelling neutral beams in fusion devices: Beamlet-based model for fast particle simulations. *Computer Physics Communications*, 188:33–46, 2015.

[32] C.D. Challis, J.G. Cordey, H. Hamnén, P.M. Stubberfield, J.P. Christiansen, E. Lazzaro, D.G. Muir, D. Stork, and E. Thompson. Non-inductively driven currents in JET. *Nuclear Fusion*, 29(4):563, 1989.

[33] G.G. Lister. FAFNER-a fully 3D neutral beam injection code using monte carlo methods. *Technical Report IPP*, 4(222), 1985.

[34] R. Albanese, R. Ambrosino, and M. Mattei. CREATE-NL+: A robust control-oriented free boundary dynamic plasma equilibrium solver. *Fusion Engineering and Design*, 96-97:664–667, 2015. Proceedings of the 28th Symposium On Fusion Technology (SOFT-28).

[35] A. Pankin, D. McCune, R. Andre, G. Bateman, and A. Kritz. The tokamak monte carlo fast ion module NUBEAM in the National Transport Code Collaboration library. *Computer Physics Communications*, 159(3):157–184, 2004.

[36] M. Schneider, L.G. Eriksson, V. Basiuk, and F. Imbeaux. On alpha particle effects in tokamaks with a current hole. *Plasma Physics and Controlled Fusion*, 47(12):2087, 2005.

[37] M. Schneider, L.G. Eriksson, T. Johnson, R. Futtersack, J.F. Artaud, R. Dumont, B. Wolle, and ITM-TF Contributors. A rapid fast ion fokker–planck solver for integrated modelling of tokamaks. *Nuclear Fusion*, 55(1):013003, 2014.

[38] M. Weiland, R. Bilato, R. Dux, B. Geiger, A. Lebschy, F. Felici, R. Fischer, D. Rittich, M. van Zeeland, the ASDEX Upgrade Team, and the Eurofusion MST1 Team. RABBIT: Real-time simulation of the NBI fast-ion distribution. *Nuclear Fusion*, 58(8):082032, 2018.

[39] J.F. Artaud et al. METIS: a fast integrated tokamak modelling tool for scenario design. *Nuclear Fusion*, 58(10):105001, 2018.

[40] L. Spitzer and R. Härm. Transport phenomena in a completely ionized gas. *Phys. Rev.*, 89:977–981, 1953.

[41] P. Vincenzi, P. Agostinetti, J. F. Artaud, T. Bolzonella, T. Kurki-Suonio, M. Mattei, M. Vallar, and J. Varje. Optimization-oriented modelling of neutral beam injection for EU pulsed DEMO. *Plasma Physics and Controlled Fusion*, 63(6):065014, 2021.

[42] O. Sauter and S.Yu. Medvedev. Tokamak coordinate conventions: COCOS. *Computer Physics Communications*, 184(2):293–302, 2013.

[43] P. A. Schneider. *Characterization and scaling of the tokamak edge transport barrier*. PhD thesis, Max Planck Institute for Plasma Physics, 2012.

[44] M. Cecconello. Private communications, 2022.

[45] H. Cabal et al. Fusion power in a future low carbon global electricity system. *Energy Strategy Reviews*, 15:1–8, 2017.

[46] M. Schneider, L.G. Eriksson, I. Jenkins, J.F. Artaud, V. Basiuk, F. Imbeaux, T. Oikawa, JET-EFDA contributors, and ITM-TF contributors. Simulation of the neutral beam deposition within integrated tokamak modelling frameworks. *Nuclear Fusion*, 51(6):063019, 2011.

[47] K.D. Zastrow, W.G.F. Core, L.G. Eriksson, M.G. Von Hellermann, A.C. Howman, and R.W.T. König. Transfer rates of toroidal angular momentum during neutral beam injection. *Nuclear Fusion*, 38(2):257, 1998.